Modelling and Optimization of an Airflow Window with Between-the-Panes Shading Device

by

Chris Hadlock

A thesis
presented to the University of Waterloo
in fulfillment of the
thesis requirement for the degree of
Master of Applied Science
in
Mechanical Engineering

Waterloo, Ontario, Canada, 2006

I hereby declare that I am the sole author of this thesis. This is a true copy of the thesis, including any required final revisions, as accepted by my examiners.

I understand that my thesis may be made electronically available to the public.

Abstract

This thesis deals with the numerical investigation of the upper section of a building-integrated photovoltaic/thermal double-façade. The upper section consists of an airflow window with a between-the-panes roller blind. The purpose of this thesis is to develop and validate a numerical model in order to optimize the design of the system. The lower section, which consists of building-integrated photovoltaics, has already been modelled at Concordia University. The results from the lower section will be used as inputs to the upper section.

The validation of the model was carried out in three stages. In the first stage, the model was validated for forced convection between parallel plates using analytical data as benchmarks. In the second stage, a radiation analysis was performed for single, double and triple-glazed closed system with natural convection only. In the third and final validation stage, experimental data gathered from the Solar Lab at Concordia University was compared to the numerical model. The model included the effects of radiation for an open system with forced convection and a between-the-panes roller blind. For all three stages of validation, the results from the model were in excellent agreement with the benchmarking data.

Once the model was validated, a parametric analysis was used to determine the effects of varying key model parameters. The outlet temperature, the useful energy gain, and the net energy gain of the system were plotted as a function of inlet velocity. It was concluded that as the flow rate through the cavity was increased, the air temperature at the outlet approached that of the outdoor ambient air. By computing the heat generated from advection as well as the total losses from the system, including the heat lost from the indoor environment as well as the power consumed by the fan, the net useful heat gain of the system was calculated as a function of insolation level. Operating points (of the fan) for the upper section were therefore determined as functions of insolation level. A second order polynomial equation provided an excellent fit to the data and could therefore be used to determine the ideal operating point of the upper section for any insolation level.

Acknowledgements

Throughout this endeavor, I have been fortunate to have had the support and guidance of many people.

To Blythe, who has passed through all the peaks and all valleys at my side. The support has been unconditional and critical to my progression over that last few years. You fortitude in life provides me with strength.

I am indebted to my supervisor, Prof. M. Collins, first and foremost for creating an environment in which I enjoyed coming to work; the last two years, although arduous, have been very fulfilling. I also wish to thank Professor Collins for giving me enough academic freedom to make my own mistakes, and more importantly, learn from them.

Over the past few years I have spent countless hours with my friends and co-workers of the Solar Lab. To Nathan, who has provided hours of laughter and an unbelievable amount of help. To Shohel, whose knowledge and wisdom was limitless. To Vivek, with whom I am thankful to have shared an office and who has always

respectfully accommodated my indiscretions. Thanks to Marty, who helped orchestrate an unbelievably fun working environment. To my office neighbors, Victor and Veronique, thank you for your kindness.

The resources that have been afforded to me throughout my graduate degree have allowed the journey to progress a smoothly as possible. In particular I would like to thank Professor Stubley, who I relied on for numerical guidance, particularly near the beginning of my thesis when staying on track was critical. To Prof. Wright, whose wisdom and advice was always constructive and forthcoming.

During my brief visits to Montreal, I was extremely fortunate to have worked alongside Prof. Athienitis and his group of students. In particular, Liao Liang and Luis Candanedo, who were most tolerant and patient of my many requests. This thesis could not have been completed without your help.

Table of Contents

List of Tables

List of Figures

Nomenclature

Abbreviations

1-D	One-Dimensional
2-D	Two-Dimensional
3-D	Three-Dimensional
AFW	AirFlow Window
ASHRAE	American Society of Heating, Refrigeration and Air-Conditioning Engineers
BC	Base Case
BIPV	Building-Integrated PhotoVoltaics
BIPV/T	Building-Integrated PhotoVoltaic/Thermal
CCD	Charge-Coupled Device
CFD	Computational Fluid Dynamics
CG	Clear Glass
CONV	Convection
CPU	Central Processing Unit
CV	Control Volume
DO	Discrete Ordinates
DOE	Department of Energy
E	Emissivity
EWT	Enhanced Wall Treatment
GDF	Glass Double Façade
HVAC	Heating, Ventilating and Air Conditioning
IM	Interior Mesh
LE	Low-Emittance
LES	Large Eddy Simulation
NW	Near Wall
PIV	Particle Image Velocimetry
MAX	Maximum
NIST	National Institue of Standards and Technology
NS	Navier-Stokes
RANS	Reynolds-Averaged Navier-Stokes
RNG	Renormalization Group
RTE	Rate Transfer Equation

SST	Shear-Stress Transport
SW	Stream Wise
SWT	Standard Wall Function
TRNSYS	Transient System Simulation Program
WF	Wall Function

Symbols

#	Number
a	Absorption Coefficient [dimensionless]
A	Area [m^2]
A_c	Cross-sectional Area [m^2]
C	Specific Heat [J/kgK]
CP	Wind Pressure Coefficient [dimensionless]
d	Distance from Wall to Blind [m]
D	Diameter [m]
D_h	Hydraulic Diameter [m]
ψ	Friction Factor [dimensionless]
f	Frequency [1/s]
F	View Factor [dimensionless]
g	Gravity constant (9.81) [m/s^2]
G	Radiation Flow [dimensionless]
G_s	Incident Solar Radiation [W/m^2]
h	Heat Transfer Coefficient [W/m^2K]
H	Height [m]
HP	Power [W]
I	Radiation Intensity [W/m^2]
J	Torque [W/m]
k	Thermal Conductivity [W/mK]
K	Extinction Coefficient [dimensionless]
K_f	Pressure Drop Loss Coefficient [dimensionless]
l	Path Length [m]
L	Length [m]
m	Mass Flow Rate [kg/m^3]
n	Refractive Index [dimensionless]
n	Number of
Nu	Nusselt [dimensionless]
P	Pressure [Pa]
$P_{electric}$	Electric Power [W]
$\wp$	Wetted Perimeter [m]
Pr	Prandtl [dimensionless]
q	Heat [W]
q''	Heat Flux [W/m^2]
Q_g	Rate of Internal Heat Gain [W]
$Q_{thermal}$	Thermal Energy [W]
$\vec{r}$	Position Vector [m]

r_s	Reflectivity [dimensionless]
Re	Reynold [dimensionless]
$\vec{s}$	Direction Vector [m]
$\vec{s}'$	Scattering Direction Vector [m]
s	Position [dimensionless]
S	Stratification Parameter [dimensionless]
S'''	Volumetric Source Term [W/m^3]
t	time [s]
T	Temperature [K,°C]
u	Velocity (x-direction) [m/s]
u_τ	Friction Velocity [m/s]
U	Thermal Conductivity [W/m^2K]
U	Thermal Energy Flow [dimensionless]
v	Velocity (y-direction) [m/s]
V	Velocity [m/s]
w	Width [m]
W	Wind Speed [m/s]
X	x-direction
Y	y-direction
z	Thickness [m]
Z	Cube Root of Building Volume [m]

Greek Symbols

α	Absorptance/Absorptivity [dimensionless]
β	Thermal Expansion Coefficient [1/K]
γ	Eddy Diffusivity [dimensionless]
δ	Kronecker Delta [dimensionless]
Δ	Change in
ε	Emissivity [dimensionless]
ϵ	Turbulent Kinetic Dissipation [m^2/s^3]
ς	Angle of BIPV with respect to Horizontal [degrees]
η	Efficiency [dimensionless]
θ	Slat Angle [degrees]
θ_L	Incidence Angle [degrees]
θ^*	Influence Coefficient [dimensionless]
Θ	Polar Angle [degrees]
κ	Turbulent Kinetic Energy [m^2/s^2]
λ	Wavelegth [m]
μ	Viscosity [kg/ms]
ρ	Density [kg/m^3]
ρ	Reflectance [dimensionless]
σ	Stefan-Boltzmann constant (5.672×10^{-8} W/m^2K^4)
σ_s	Scattering Coefficient [dimensionless]
τ	Shear Stress [N/m^2]
τ	Transmittance [dimensionless]

φ	Azimuthal Angle [degrees]
Φ	Phase Function [dimensionless]
ω	Specific Dissipation Rate [1/s]
Ψ	Angular Velocity [rad/s]
Ω	Solid Angle [steridians]

Subscripts

∞	Far Stream
a	Air
ac	Airflow Cavity
b	Blackbody
B	Back
bc	Base Case
c	Wall
conv	Convection
D	Diameter
eff	Effective
ext	External
fd	Fully Developed
h	Hydraulic
H	Heat
i	Related to the i^{th} Component
i	Inner Surface
ii	Inner Surface when Inner Surface is Heated
in	Related to the Incoming Energy
j	Related to the j^{th} Component
L	Incident
m	Mean
M	Refering to a Particular Surface
mom	Momentum
N	Normal
0	Free Stream
o	Outside
out	Related to the Outgoing Energy
p	Pixel
r	Radiation
R	Room
s	Solar
t	Turbulent
th	Thermal
tr	Transmitted
tot	Total
w	Wall
x	X-direction
y	Y-direction

Chapter 1

Background

1.1 Introduction

Throughout the world and especially here in North America, higher living standards combined with an aging population have contributed to rising energy consumption levels. As an indication of higher living standards in the United States, between 1950 and 1990 the floor space requirement per person doubled (Owens, 1994). During that same period, the population of the United States grew by a factor of 1.6 (U.S. Census Bureau, 2005). This combination resulted in massive increases in the energy demand, and energy consumption grew by a factor of 2.5 (Figure 1.1) (DOE, 2004b). These factors, coupled with frivolous energy consumption, have contributed to dwindling natural resources and volatile fuel prices.

A growing dependency on depleting resources has become a major cause for concern in many countries, including the United States and Canada. The potentially irreversible environmental damage caused by pollution is yet another reason why modern day society has a renewed interest in the topics of energy consumption and energy conservation. Irrespective of the reasons, energy and energy-related issues now play an important role in global politics, dictating to a large extent the future economic prosperity and autonomy of nations.

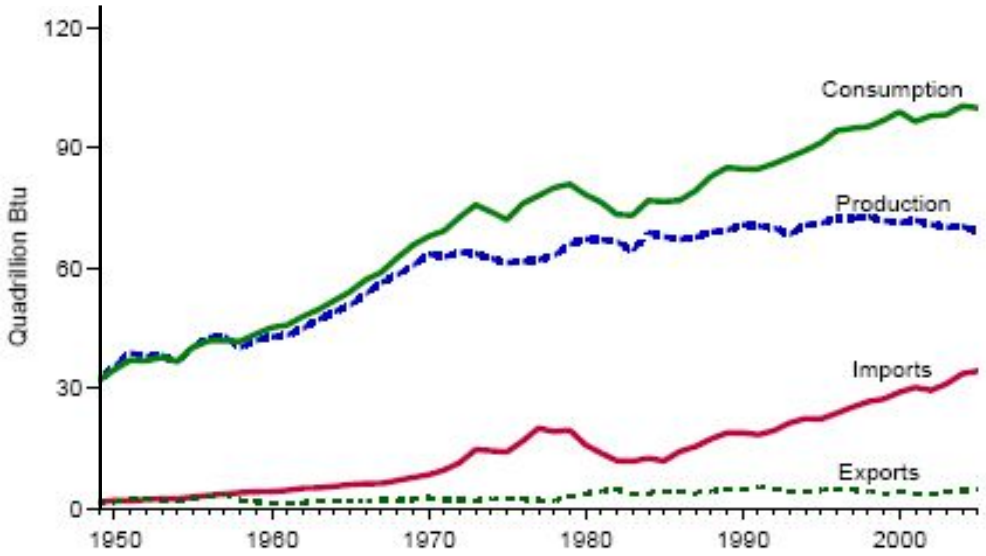

Figure 1.1: Energy overview in the United States between 1949 and 2004 (DOE, 2004a).

In 2003, 39% of the total energy consumption in the U.S. was due to the primary energy consumption of buildings (DOE, 2005a). Within the residential energy sector, space heating accounted for 50% of the energy consumption while lighting accounted for 7% (DOE, 2005b). Data pertaining to the commercial energy sector indicated that space heating consumed 24% of the total energy while lighting accounted for 16% (DOE, 2005c). Windows, which allow solar energy and daylight into buildings, have a direct impact on the space conditioning and lighting of a building; in 2002, windows accounted for 3% of the national energy consumption in the United States (DOE, 2002) at a cost of $25 billion per year. The development of a more energy efficient window will therefore provide a substantial energy savings potential for both residential and commercial buildings.

1.2 History of Airflow Windows

For more than a century, windows have been used in buildings for daylighting, heating, cooling, and providing air exchange between the indoor and outdoor

environment. In the early 1860's, Jacob Forst of the United Kingdom published an article in which he speculated that the power from the sun could be employed to provide "an admirable arrangement for house ventilation" using circulated air warmed by the greenhouse effect (Wigginton and McCarthy, 2000). It is believed that the first real semblance of an airflow cavity emerged two decades later in 1882 when Edward Morse built the first ever solar wall (Wigginton and McCarthy, 2000). The wall, which comprised an exterior glass layer and an interior corrugated black iron sheet, was mounted in front of a masonry wall. Although the physics of solar energy was not well understood at the time, Morse knew that a black iron sheet would be warmed by the sun's energy and that this heat would in turn warm the air in the cavity. A series of flaps were used to control the air exchange between the solar wall and the indoor environment. When the outside air temperature was deemed sufficiently warm, the flaps would be opened and the outdoor air would be drawn from the bottom of the solar wall past the black sheet and brought into the house as warm air. In the summer months, Morse used the solar wall to cool the building's envelop by venting the heated air to the outside (Wigginton and McCarthy, 2000).

In order to harness the full effects of the sun, A. E. Morgan in 1961 designed a highly advanced double skin wall for a school building in the United Kingdom that included a double glass façade separated by a 600 mm gap (Wigginton and McCarthy, 2000). The design represents a very important step in the development of the AirFlow Window (AFW) as it was one of the first significant designs which met both the thermal and lighting needs of a building. Reversible panels were used to optimize the thermal efficiency of the multiple-layered wall; one side of the panel comprised polished aluminum while the other side was painted black. During the colder winter months, the

black surface was used to provide maximum absorption of thermal energy which was used to heat the air. The reverse principle was used in the summer months whereby the highly reflective aluminum surface would help reduce the heat gain into the school building.

It wasn't until the energy crisis of the 1970's that energy conservation truly became an important factor in the design and construction of new buildings. During this period, the savings potential of multi-façade windows resulted in a noticeable increase in new building designs around the world that included airflow windows (Messadi and Augenbroe, 2001). It was believed that double façades could truly help reduce building energy consumption at a relatively affordable price. In 1980, airflow windows were installed in an office building in Portland, Oregon; this was likely the very first airflow window in the United States (Ripatti, 1984).

Since then, many different variations of airflow windows have come into existence, all of which rely on the same fundamental principles employed by Jacob Forst and other early solar wall inventors. With the addition of new technologies, today's airflow windows now perform multiple functions, making the widespread integration of airflow windows within buildings more economical.

1.3 Current State of Airflow Window Systems

As the knowledge and use of airflow windows and multi-window façades grew, new designs evolved which aimed to harness the full potential of the airflow window. One of the very significant advancements in AFW's was the incorporation of solar panels, or PhotoVoltaics (PV). The early AFW systems provided thermal energy, but never generated electric energy. The coupling of both thermal and electric generation

within a common system is a seemingly logical progression as both technologies are fueled by the same source. Furthermore, as will be explained in subsequent sections, electrical energy is required in many of the current airflow window designs to drive the fans (for the forced convection).

Although one of the main purposes of windows has always been to provide a passage for light into a building, only today is the importance of such a phenomenon becoming understood. Recent studies have shown that the productivity and performance of workers are directly affected by daylighting and that "workers [with proper daylighting] are less prone to take time off work, [thus] reducing absenteeism" (Santamouris, 2001). This reduction in absenteeism has a direct impact on productivity and company profits. Further savings can be realized via daylighting by reducing the energy required for artificial lighting in a building. In some cases, artificial lighting accounts for 50% of a building's energy consumption (Ripatti, 1984). Today, AFW's are designed with daylighting in mind, making it possible to design an entire building façade which will meet both thermal and illumination needs of the building.

Other recent advances in AFW systems include the use of motorized fan systems to incite forced convection within the cavity, spectrally selective coatings, and shading devices to help control the amount of direct solar gain into a building. The purpose and function of the various modern AFW technologies are explained in subsequent sections.

1.3.1 Concordia University Solar Lab

At Concordia University in Montreal, Quebec, Canada, there exists a Solar Laboratory (Figure 1.2) containing a full scale outdoor test facility for the purpose of researching solar generation systems. One such system is the building-integrated

photovoltaic/thermal (BIPV/T) system, which has a combination of electric (PV) and thermal (AFW) generation (Charron, 2004). At Concordia, two BIPV/T configurations have been tested (Figure 1.3). In Configuration 1 (Figure 1.3a), the PV comprises the exterior surface of the bottom section. Adjacent to the PV is a layer of insulation. The upper section of Configuration 1 consists of a double glazed airflow cavity with motorized roller blind. In Configuration 2 (Figure 1.3b), the PV is located in the bottom section between the exterior glazing and the interior insulation layer. The upper section of Configuration 2 is identical to that of Configuration 1 except that a venetian blind is used instead of a roller blind. To date, analytical 1-D and 2-D models (Athienitis et al., 2004) have been developed (Section 2.4.2 from Chapter 2) for the lower (PV) section of Configuration 1 and Configuration 2. Moreover, a Computational Fluid Dynamic (CFD) model has been developed for the lower section of Configuration 1 only (Athienitis et al., 2004). Preliminary results (Liao, 2005) of the lower section indicate that the electrical efficiency of Configuration 1 is 21% greater than that of Configuration 2. The opposite is true however of the thermal efficiency as Configuration 1 has a 25% lower thermal efficiency than Configuration 2. The lower electrical efficiency and higher thermal efficiency of Configuration 2 is due to the placement of the PV. As the PV is behind a glazing, a portion of the incident solar radiation (insolation) is reflected before reaching the PV. However, heat generated by the PV is not lost to the outdoor environment as is the case in Configuration 1, which explains the increased thermal efficiency of Configuration 2.

The work performed at the University of Waterloo is intended to further advance the work already completed at Concordia University. As such, this thesis presents the

development of a computational fluids dynamic (CFD) model used to model the upper section (AFW) of Configuration 1.

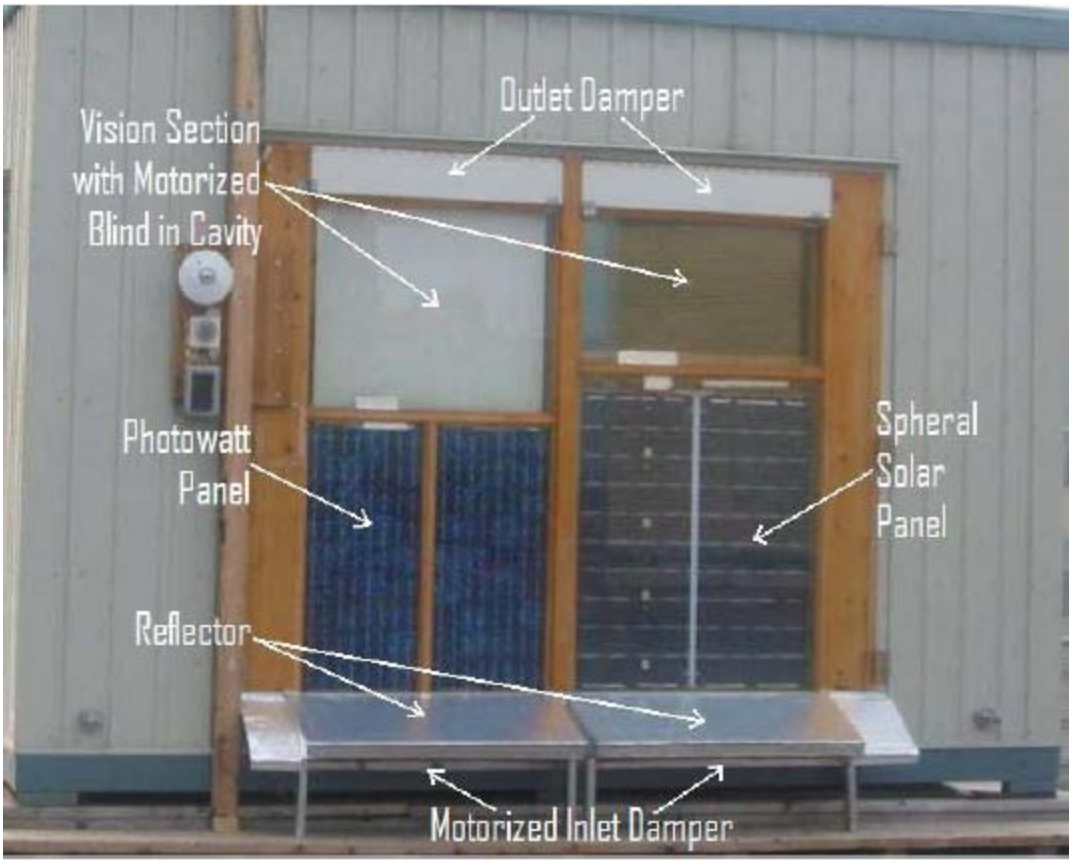

Figure 1.2: BIPV/T Configuration 1 (left) and Configuration 2 (right) at Concordia University Solar Lab (reproduced from Liao, 2005).

1.4 The Technology

In the last 150 years (Wigginton and McCarthy, 2000), there has been a push to make windows more energy efficient. As a result, we have seen the emergence of new technologies such as: substitute fill gases like argon and krypton, spectrally selective coatings, tinted glazings, switchable glazings, multi-paned windows, etc. All of these technologies are designed to reduce the energy loss through windows.

The energy gain/loss through fenestration occurs via all three modes of heat transfer: radiation, convection and conduction. Radiation from an energy source travels in various wavelengths and intensities. Both the magnitude and range of intensities

depend on the temperature of the source. Consider, for instance, radiation emanating from the sun towards the earth. This radiation, emitted from a source (the sun) of around 5800 K, travels in wavelengths ranging from approximately 0.3 to 3 μm (Hollands et al., 2001). The solar portion of the radiation energy spectrum (Figure 1.4) is often referred to as short wave or *solar* radiation and is comprised of visible radiation, as well as portions of both the UV and near-infrared wavebands. Objects at room temperature however, emit *long wave* radiation, from 3 to 50 μm. The term *thermal radiation* is used to define radiation from 0.1 to 100 μm which contains both the short wave (solar) and long wave radiation (Figure 1.4). The aforementioned definitions, which spectrally characterize the radiation, will be used throughout this report.

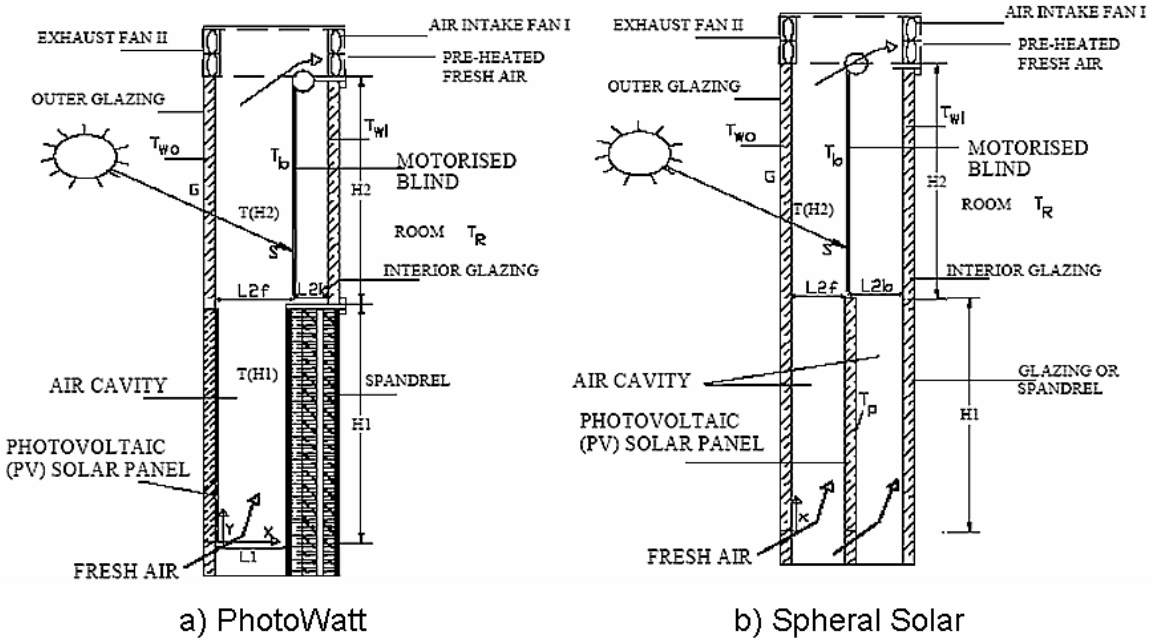

Figure 1.3: Configuration 1 (PhotoWatt) and Configuration 2 (Spheral), Figure 1.3a and 1.3b, respectively (reproduced from Liao, 2005).

In order to impede the flow of energy from one body to another, it is important to understand the mechanisms by which the energy is transferred. Irregardless of the climate, a maximum resistance to heat transfer will result in maximum energy savings; this is applicable to not only fenestration, but all façade materials. The methods used to

impede the flow of energy depend upon the mode of heat transfer. The manner in which convection and conduction in windows can be reduced is well understood. For example, the type of fill gas used in a multiple glazing window will directly affect the amount of convection between glazings. The geometry and composition of a given material, including glass, spacers, frame, insulation, etc., will have a direct impact on the conduction through the window. Although both conduction and convection heat transfer are essentially impossible to eliminate, the methods for their reduction are relatively straightforward. The reduction of radiation heat transfer through a window however, is both difficult and complex. One of the complications of radiative heat transfer is due to a seemingly paradoxical problem; for best energy efficiency, a set of glazings should block the maximum amount of heat while allowing the maximum amount of light. Since both light and heat emanate from the same source, the problem is understandably a difficult one.

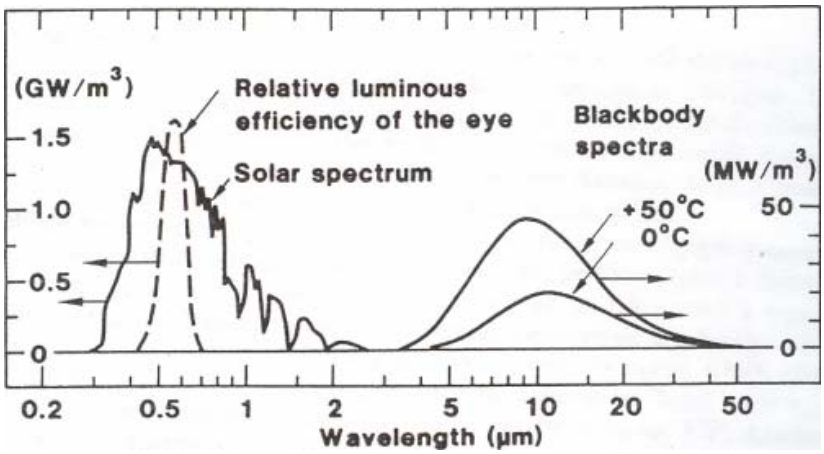

Figure 1.4: Black-body radiation spectrum (reproduced from Hollands et al., 2001).

1.4.1 Glazings

One of the easier ways of decreasing the amount of heat flow through a window is to increase the number of glazings. Heat flow through a window is generally characterized by its U-value, which is the conductance and has units of W/m^2K. A

window with a low U-value is therefore desireable in building design as a low U-value indicates a better ability to impede heat flow and thus reduce the energy losses. The conductance of a conventional double-glazed window is around 3.0 W/m^2K compared to 5.5 W/m^2K for a single glazing (Huang, 2005). Today, double-glazed windows have become the standard, as were single glazed windows back in the 1970's. In some cases, triple glazings are used, but only when the benefits of the added insulation outweigh the cost of the additional glazing.

The heat transfer through a glazing occurs via two modes only: radiation and conduction. The conduction through a glazing is directly proportional to the thickness and conductivity of the material. The radiation heat transfer process through a glazing varies with wavelength. Window glazings are generally opaque to long wave radiation; very little direct long wave transmission through a window will occur. However, through the process of absorption and re-emission, long wave energy will enter a building. Short wave (solar) radiation will be transmitted, reflected and absorbed at each glazing; the proportion of each will depend on the spectral characteristics of the glazing.

In order to account for radiation exchange in a multi-layered glazing system, both a heat transfer analysis and an optical analysis is required (Wright, 1998). This two-step analysis is possible due to the generally accepted demarcation of solar (below ~ 3 μm) and long wave radiation (above ~ 3 μm). The optical analysis is used to determine the amount of solar radiation absorbed by each glazing as well as the amount that is transmitted to the inside environment. This analysis requires no information of the glazing temperatures or heat transfer properties, only the solar spectral properties of the glazings are required. The heat transfer analysis, which makes use of the results from the optical analysis, is performed using a radiosity balance; the heat transfer entering and

leaving each glazing is determined. For a steady-state analysis, the solar energy absorbed at each layer must equal the net heat transfer of that layer.

1.4.2 Low-Emittance Coatings

One of the methods for providing better control over the passage of sunlight and heat into a building is through the use of spectrally selective coatings. Low-emittance (low-E) windows, which were introduced to the North American market in the early 1980's (Limb, 2002), use wavelength-dependent properties to reduce the energy flow through the glazing without significantly impeding the passage of natural light into the building. For example, in a heating-dominated climate, it is desirable to use coatings with high transmissivity in the short wavelengths and low transmissivity in the long wavelengths to allow the influx of solar radiation while minimizing the heat losses from inside the building. Depending on the type of climate, a range of coatings are available. In cooler climates, low-E coatings with high solar gain are typically employed while low-E coatings with low solar gain are used in warmer climates. The coating, which is highly reflective, is typically placed on one of the glazings on the side which is in contact with the fill gas. This reduces the transmission of the absorbed radiation through the glass. By reducing the amount of long wave radiation entering/leaving the building the cooling/heating load of the building is reduced. It has been estimated that simple low-E glazing can reduce the heating and cooling requirements of windows by more than 50% while achieving daylight requirements (Santamouris, 2001).

1.4.3 Shading Devices

One effective method of reducing the solar gain into a building is through the use shading devices such as blinds or curtains. Typically, shading devices are located on the inside of a building and are controlled by the inhabitants of the building. By reducing the solar gain during the summer months a reduction in the cooling load of the building is achieved. Although these devices essentially act as a radiation shield to both short and long wave radiation, a more effective use of shading devices can be achieved by placing the shading device between the glazings and controlling them based on stimuli. This method, which is only relevant to a multiple-glazed fixed[*] window, such as an AFW, helps reduce both the long and short wave transmission. Such a between-the-panes shading device will reflect radiation attempting to travel from one glazing to the other. Unlike the typical case where the shading device is placed inside the building, this configuration stops a certain portion of the thermal radiation from ever entering the building's envelope. Shading devices are therefore another effective device used to reduce the U-value of the window. Ultimately, to achieve the minimum U-value, the shading device would be placed on the buildings exterior. Due to potential weather damage, this configuration is not typically used.

1.4.4 Energy Production

The use of low-E coatings and shading devices in conjunction with AFW's is one of the ways to maximize both the energy efficiency of the building and the comfort level for its inhabitants. However, in order to take energy conservation a step further while ensuring maximum comfort at minimal cost, incorporating energy production is the next logical step. For this reason, modern AFW's generate both thermal and electrical energy.

[*] In this context, fixed windows are those without the ability to slide or open to allow outside air in.

PV: During hot summer months, a tremendous amount of time and energy goes into eliminating the unwanted effects of the sun. However, by using PV, the energy from the sun can be harnessed and buildings can become micro-generators. Depending on the size and the energy demand of the building, this electricity production may provide significant energy savings. For large buildings, PV is often placed on the south facing façade due to a lack of roof or ground space. Although such a setup results in lower PV efficiencies due to large angles of incidence, several significant benefits can be derived from this. By incorporating PV with an airflow window, electrical and thermal energy is generated and no separate mounting structure is required (Athienitis et al., 2004). Furthermore, this type of façade can also save on the cost of conventional cladding (Infield et al., 2003).

A solar panel's efficiency is a function of many parameters, one of which is PV panel temperature. As it is for most electronic devices, the lower the temperatures, the higher the operating efficiency. For example, the efficiency of crystalline silicon panels will drop 0.5% for every degree over its rated temperature of 25° (Tripanagnostopoulos, 2002). The effect of using forced air to cool a building-integrated PV (BIPV) system was studies by Yang et al. (1996) who developed a model to predict the electrical performance of BIPV systems. A 15°C temperature drop was reported during operation for a well designed airflow cavity. According to the authors, this temperature drop resulted in an 8% increase in the PV efficiency (Yang et al., 1996). For this reason, the use of forced convection to cool the solar panel provides a significant improvement over BIPV systems that use natural convection as a cooling mechanism.

Thermal Heating/Cooling: Historically, airflow windows have used buoyancy-driven natural convection to provide pre-heated air to the building. However, many recent airflow systems are now using forced convection to increase heat transfer within the cavity. This thermal energy may be used as a source of heat during the heating season, or, if rejected to the environment, used as a cooling mechanism to the buildings envelop during the summer. By combining BIPV with an AFW, additional heat is provided to the air in the cavity thereby increasing the thermal efficiency of the BIPV/T system. As previously mentioned, the forced convection also acts to increase the electrical efficiency of the system. As such, combining BIPV with AFW's results in a simultaneous increase in both efficiencies. In some buildings, the exhaust air from the AFW is piped directly to the HVAC unit to be conditioned and subsequently used to heat the building.

1.5 Thesis Objectives and Outline

The objectives of this thesis are as follows:

- To develop a 2-D numerical model that will include conductive, convective and radiative heat transfer of the upper portion of Configuration 1, which includes two glazings and a between-the-pane shading device.

- To validate the 2-D model using published numerical and analytical results as well as experimental data from the Concordia University Solar Lab.

- To examine the effects of varying key parameters as they pertain to the overall performance of the system. The results will be used to provide suggestions for future optimization methods of BIPV/T systems.

The steps taken to achieve the aforementioned objectives will be described throughout this thesis. As a starting point, a review of relevant research will be conducted in Chapter 2. The validation of the numerical model is then described in Chapter 3 followed by a presentation and discussion of the CFD results in Chapter 4. A summary of the work, including conclusions and recommendations, will be presented in Chapter 5.

Chapter 2

Literature Review

2.1 Introduction

In this chapter, a brief overview of research pertaining to airflow windows will be presented. The topics for the literature review will be cover the two main sections of the BIPV/T system - the lower section (Section 2.2) consisting of the BIPV and the upper section (Section 2.3) consisting of the AFW with between-the-pane shading device. For the upper section, research pertaining to flow between glazings with and without shading devices will be reviewed. Research presented on the lower section will focus on BIPV systems. Analytical, numerical and experimental work will be presented for both cases. Finally, the work which concerns the BIPV/T system from the Solar Lab at Concordia University will be presented (Section 2.4). Before proceeding, the terminologies that will be used throughout the remainder of this thesis will be presented.

An AFW is comprised of two or more glazings through which air flows either by natural, mixed or forced convection. As this thesis is mostly concerned with double-glazed cavities, unless otherwise noted the term AFW will refer to double glazed systems only.

It is generally accepted that there exists three different types of airflow windows (Messadi and Augenbroe, 2001). The first type, called the 'exhaust airflow window', circulates air from inside (labeled IS in the figure) the building through the double façade before it is exhausted to the outside (labeled OS in the figure) environment (Figure 2.1a). The second type is called 'supply airflow window' and circulates outside air through the airflow cavity before entering the building (Figure 2.1b). The third type of airflow window (Figure 2.1c) is known as the 'return airflow window'; inside air is circulated through the AFW and vented back into the building. The AFW at Concordia University is a hybrid system. The destination of the exhaust air is a function of the weather; air is exhausted to the outdoor environment for cooling and is brought into the building for heating. This particular AFW does not therefore fit into any one of the three aforementioned AFW categories. As a matter of convenience, throughout the remainder of this thesis, the AFW at Concordia University, irregardless of the season, will only be called by the generic name of AFW.

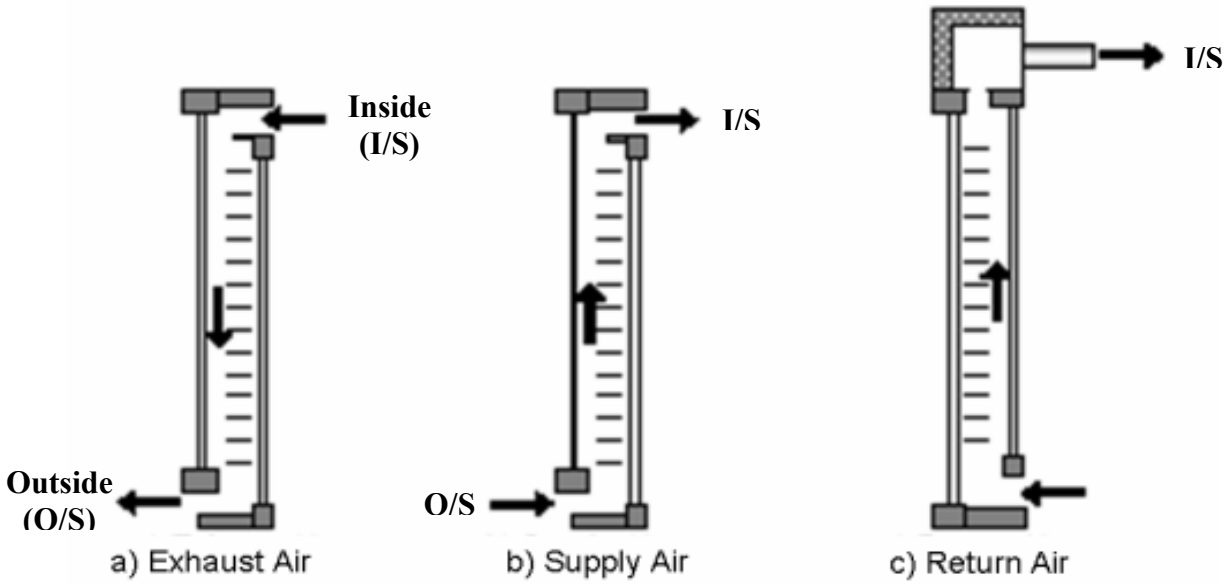

Figure 2.1: The three classifications of standard AFW's (Figure 2.1a, 2.1b and 2.1, respectively) (reproduced from Messadi and Augenbroe, 2001).

The research that is presented in this chapter which pertains to the lower section of the Concordia University BIPV/T systems focuses on existing building-integrated PV research. In this thesis, the term BIPV is used to define a system for which there exists a multi-façade wall of which the PV cell comprises one of the layers; in a double-façade wall, the PV is typically the outer layer. The term BIPV/T will be used to describe any system which generates both heat and electricity. Within the context of this thesis, BIPV/T will refer specifically to the BIPV and AFW combination which is present at the Solar Lab.

2.2 Lower Section of BIPV/T

The study of the BIPV/T system begins with the study of convection in tall cavities. Many such studies, new and old, have been performed for both open and closed cavities (Tao, 1960, Aung, 1972 and Xaman, 2005). Within the context of this thesis, only open (or ventilated) cavities are of interest.

2.2.1 Ventilated Cavities

The airflow in traditional ventilated cavities is driven by two mechanisms: wind and buoyancy forces. The effects of wind are not easily quantified and as a result are often neglected. The effects of temperature variations leading to buoyancy forces are well understood and mathematical expressions for buoyancy-driven flows over a vertical surface or between parallel plates can be found in virtually any heat transfer book (e.g. Incropera and DeWitt, 2002a). Where turbulence is concerned, empirical correlations are often used to measure the heat transfer and flow characteristics.

2.2.2 Ventilated Cavities with BIPV

The integration of PV with ventilated cavities increases the functionality of the façade as the thermal generation is now accompanied by the electric generation. Various approaches have been used to model ventilated BIPV systems; the level of model complexity ranges from simple steady-state solar collector analyses to more complex transient models.

Steady-State Models:

Brinkworths' Model

Brinkworth et al. (2000) modelled PV cladding with a naturally cooled airspace using a one-dimensional steady-state pressure balance method. The pressure balance method, also termed 'loop analysis', equates the pressure drop of one full system loop to zero. The pressure losses (in the loop) due to friction are equated to the buoyancy forces present; the buoyancy forces, which are due to the thermal gains of the air, are modelled using the Boussinesq approximation. The frictional losses within the system include the viscous forces (Eq. 2.1) within the cavity as well as the pressure losses occurring at the inlet and outlet:

$$\Delta P = K_f \left(\frac{\rho V^2}{2} \right) \tag{2.1}$$

where P, K_f, ρ and V are the pressure term, pressure drop loss coefficient, density and the air velocity, respectively. Brinkworth also investigated the effects of wind. The analysis was accomplished using wind pressure coefficients that could be either positive or negative, corresponding to a positive or negative (suction) pressure at the inlet and outlet. In the end, the authors formulated an analytical expression for the mass flow rate of air

within a ventilated BIPV system as a function of wind speed, solar gain and average velocity as follows:

$$m^3 = \frac{\dfrac{2S(\rho A_c)^2 gL\beta Q_g \sin(\varsigma)}{C} + (\rho A_c)^2 m\left[CP_1 W_1^2 - CP_2 W_2^2\right]}{\left[K_{f1} + K_{f2} + \psi \dfrac{L}{D}\right]} \qquad \textbf{(2.2)}$$

where

m mass flow rate,
S stratification parameter,
A_c cross-sectional area,
g gravity constant (9.81 m/s^2),
L length,
β thermal expansion coefficient,
Q_g rate of internal heat gain,
ζ angle of BIPV with respect to the horizontal,
C specific heat,
CP wind pressure coefficient,
W wind speed,
ψ friction factor,
D diameter.

The results of the analytical model (Eq. 2.2) were compared to experimental data obtained from the Solar Simulation Laboratory at Cardiff University in the UK; comparisons indicate strong agreement between the model and the measured data (Figure 2.2).

One of the strengths of this model resides in its user-friendly quality; one of the goals of the study was to develop a model that could be used within a simple spreadsheet. The simplicity of the model has its drawbacks as well however. For example, experimental data that is difficult to obtain is required as inputs to the model. Furthermore, as the loop analysis model is one-dimensional, only the mean velocity or mean temperature can be determined.

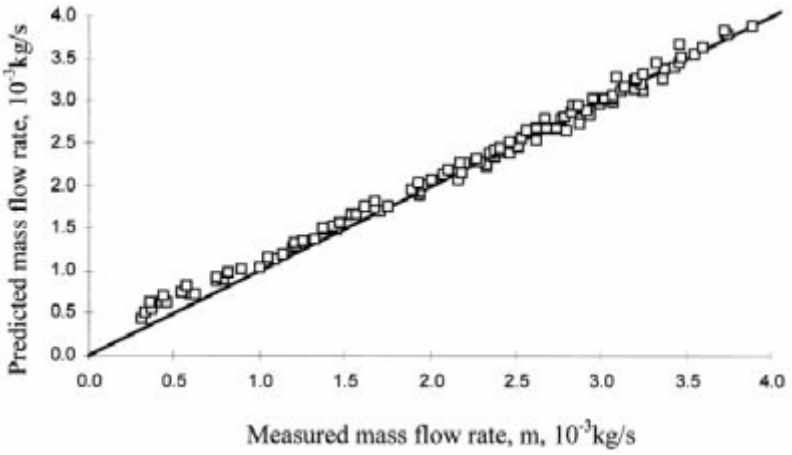

Figure 2.2: Predicted versus measured data for data by Brinkworth et al. (2000).

Infields' Model

Other attempts have been made to provide user-friendly models of BIPV systems with ventilated cavities (Infield et al., 2003). The model by Infield, developed for designers, architects and engineers, is based on *U* and *G* values where *U* represents the flow of thermal energy and *G* represents the flow of radiation within the BIPV system. The use of *U* and *G* values to represent energy flow has been used in other studies as well (Bansal and Gaur, 1996). A 1-D steady-state energy balance performed on the PV panel, glazing and air gap system, as seen in Figure 2.3, was used to calculate the heat transfer rates within the ventilated cavity. Data from the Mataro Public Library (Lloret et al., 1998), located near Barcelona, Spain, was used to validate the results. In subsequent work, Infield et al. (2004) developed a second model using a simpler solar collector-type analysis. Using the same experimental data, it was found that this simpler model predicted very similar results to the original model for summer conditions, however deviated somewhat in the results for winter conditions.

Transient Models:

Mei's Model

The majority of the BIPV models are developed for steady state (or quasi-equilibrium) conditions. However, a transient model has been developed by Mei et al. (2003) using the simulation program TRNSYS (1996). The model consists of a 14 cm air gap enclosed by a solar panel on one side and a double glazed window on the other (Figure 2.4). The transient model was run on an hour-by-hour basis; for each one-hour time step, constant insolation levels were assumed. The heat transfer was measured using Nusselt (*Nu*) numbers. In order to reduce the computational cost of the numerical simulation, the long wave radiation heat transfer expression was linearized. A solar collector model was used to calculate the heat transfer in the air gap. In order to solve the transient conduction terms, Mei used the transfer function method (ASHRAE, 1993) where pre-calculated coefficients were required. A one-dimensional finite difference analysis was performed and the model was validated using data from the Mataro Public Library. The required inputs to the model were: total horizontal radiation (beam and diffuse), outside wind speed and outside ambient temperature. The authors compared data for the inside building temperature and outlet temperature of the air gap. Although the model results were in good agreement with the experimental data, a slight lag in the model response was observed (Figure 2.5).

2.2.3 Optimization of Ventilated Façades with BIPV

The optimization of air-cooled BIPV has been the subject of investigation for many researchers. In order to optimize such a system, efforts are most often focused on reducing the temperature of the PV. A reduction of PV temperature translates into an

increase in electrical efficiency. This is usually achieved by enhancing the convective cooling around the PV by increasing the mass flow rate through the cavity. With the use of a fan, the mass flow rate can be increased as required. Other less conventional methods, like fins, exist to provide additional cooling to the PV as well. The increase in electrical efficiency combined with the additional thermal generation translates into an important cost savings potential.

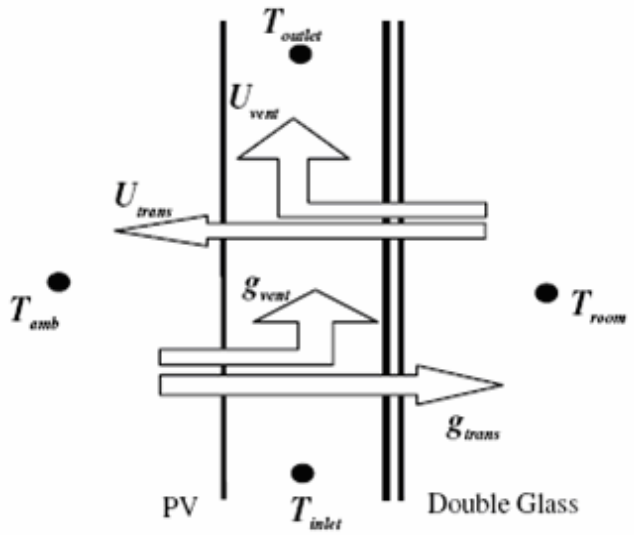

Figure 2.3: One dimensional steady-state energy balance used to calculate the heat transfer within a ventilated cavity (reproduced from Infield et al., 2004).

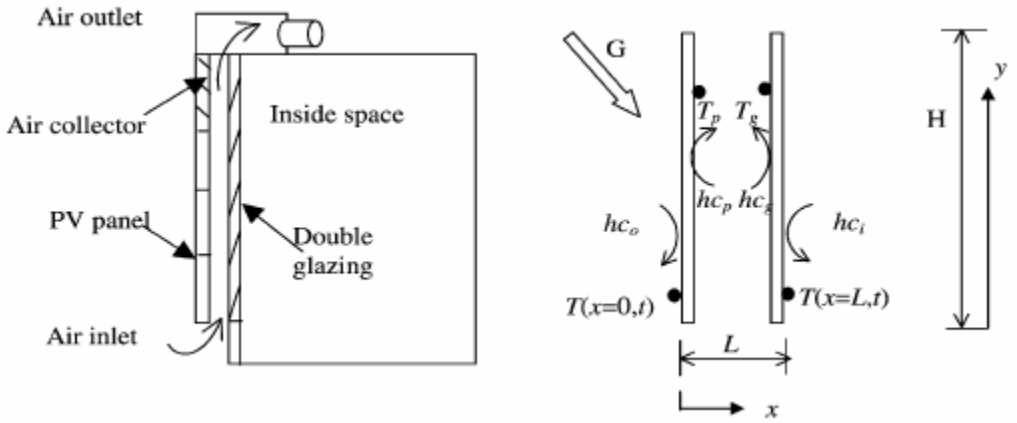

Figure 2.4: Schematic of PV façade with thermal representation (reproduced from Mei et al., 2003).

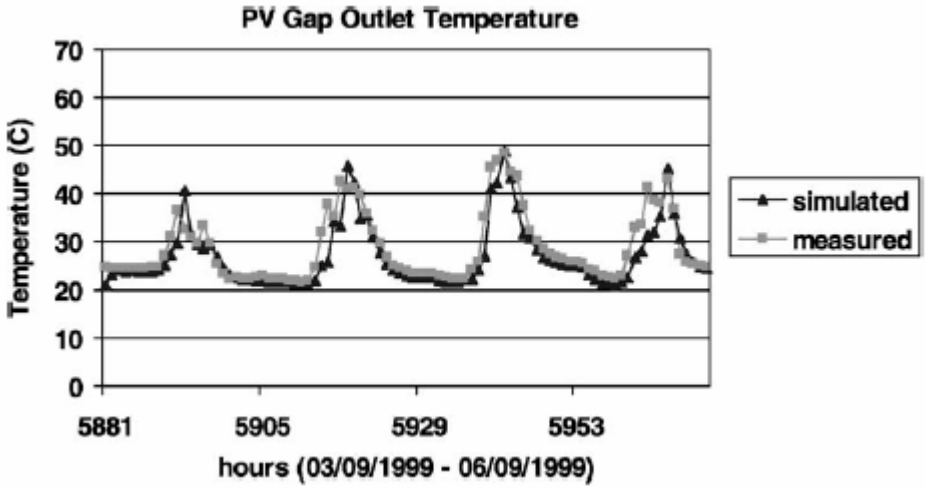

Figure 2.5: Comparison between the model and experimental data for PV façade (reproduced from Mei et al., 2003).

Less conventional methods of PV cooling has been explored by Tripanagnostopoulos et al. (2000). The research explores the effects of air channel depth, surface emissivity and various other low-cost heat extraction methods. Specifically, the authors examined the effects of fins, circular tubes and a flat metallic sheet as heat extraction methods as seen in Figures 2.6a, b and c, respectively. The effect of surface emissivity and roughness was also investigated. The authors used both air and water as cooling mediums. It was found that although the use of air is more practical, water cooled BIPV systems yield greater system efficiencies. Geometrical effects were also taken into consideration; it was found that increasing the cavity width would decrease the mass flow rate, resulting in a reduction of thermal gains. However, a greater cavity width produces a lower pressure drop, thus reducing the electrical needs of the fan. As would be expected, placing a high emissivity (high-E) surface adjacent to the PV will reduce the PV temperature, but will have the unwanted effect of increasing the temperature of the high-E surface, which is typically the building façade. The use of both fins and tubes as heat extraction methods were effective in increasing the electrical and thermal performance of the system. However, the authors warn that such heat extraction methods

may be expensive and result in a larger pressure drop. The effects of increased surface roughness to the wall adjacent to the PV resulted in a slight efficiency boost at a minimal cost. The best heat extraction method was determined to be a thin, flat metallic plate placed between the PV and façade (Figure 2.4c).

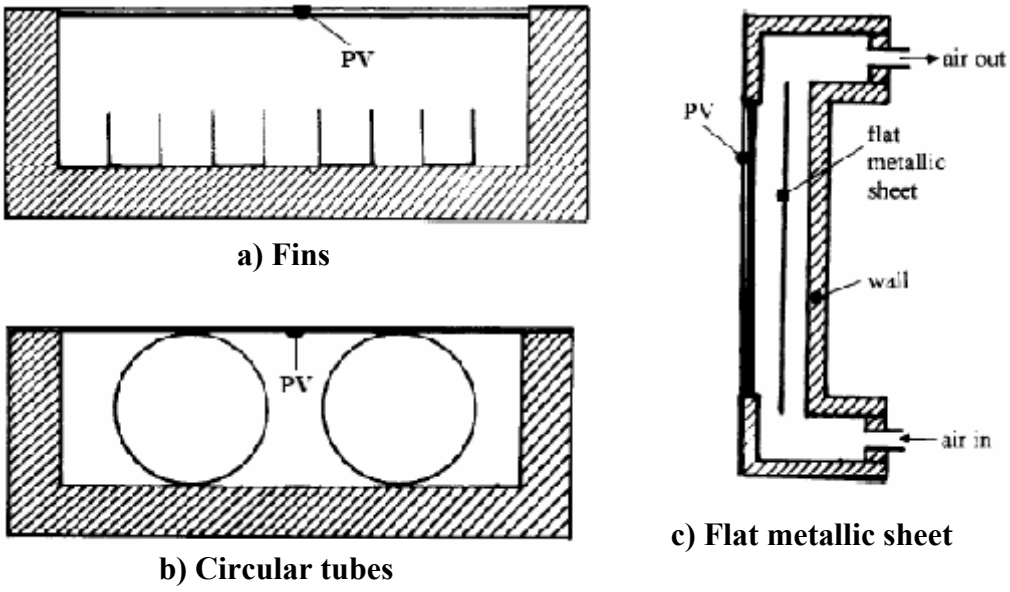

Figure 2.6: Low cost improvements to BIPV including fins (Figure 2.6a), circular tubes (Figure 2.6 b) and a flat metallic sheet (Figure 2.6c) (reproduced from Tripanagnostopoulos et al., 2000).

2.2.4 Electrical Performance of BIPV

Many studies have investigated the affect of temperature on PV efficiency. A model developed by Yang et al. (1996) was used for predicting the electrical performance of BIPV systems. The results of the model indicate that for a well designed airflow cavity, a 15°C temperature drop in the PV panel, equivalent to an 8% increase in the electrical efficiency, can be achieved.

At the Building and Fire Research Laboratory at the National Institute of Standards and Technology (NIST) in Gaithersburg, Maryland, the performance of BIPV panels and the algorithms that exist to model such systems were investigated (Hunter and Dougherty, 2001). It is interesting to note that with the exception of a single panel type,

the month of January resulted in the highest BIPV efficiencies for all solar panels due to the cooler temperatures. As would be expected, the panels without back insulation showed greater efficiencies than the insulated panels. In a follow-up study, data from the Sandia National Laboratory Model was examined (Davis et al., 2001). Of particular interest was the plot that showed the peak power of a solar panel as a function of cell temperature and solar irradiance. From Figure 2.7, it is clear that at high irradiance values, the efficiency of the PV depends heavily on its temperature.

2.3 Upper Section of BIPV/T

The upper section in question is comprised of a double-glazed cavity with between-the-panes shading device. The study of such a system can be broken up into three main areas of research: glass double façades (Manz, 2004), active envelopes (Saelens and Hens, 2001) and smart façades (Messadi and Augenbroe, 2001).

2.3.1 Glass Double Façades

Glass double façades (GDF's), also known as double skin façades or twin façades (Saelens and Hens, 2001), are characterized by two glazings in parallel forming a cavity through which air passes. Double skin façades, which are primarily used for reducing heating and/or cooling loads of a building, can also be used for acoustic and lighting control as well as ventilation (Gratia and De Herde, 2004). GDF's have been studied for natural, mixed and forced convection flows. In the past, the majority of the research has been focused on natural, or buoyancy-driven ventilation (Aung, 1972, Manz, 2004 and Xaman et al., 2005). As was previously mentioned, convection in the older AFW's was driven by two mechanisms: wind and buoyancy forces. The effects of wind are not easy

to quantify and as a result, often times neglected. The effects of temperature variations leading to buoyancy-driven flow between glazings has been analyzed analytically (Ciampi et al., 2003), numerically (Balocco, 2002) and experimentally (Balloco and Colombari, 2006).

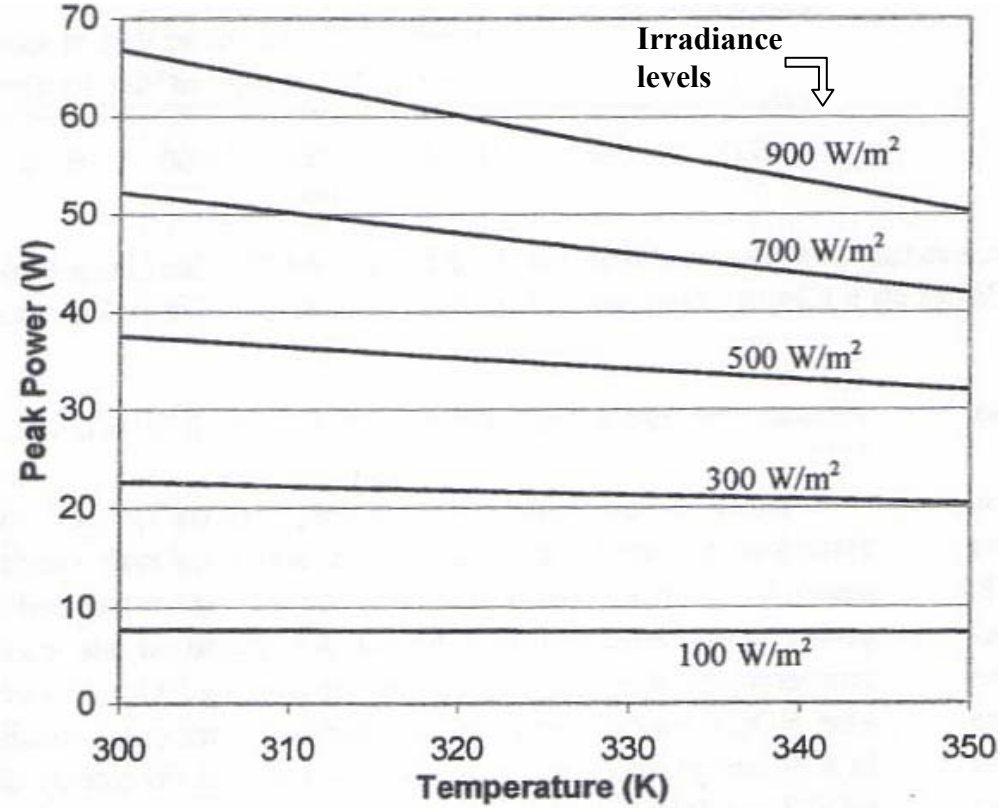

Figure 2.7: PV performance as a function of temperature and irradiance levels (reproduced from Davis et al., 2001).

In one of his studies, Ciampi et al. (2003) investigates the energy savings potential of buildings with ventilated façades during the cooling season. In particular, the influence of air duct thickness, mass flow rate, solar intensity, wall roughness, location, and resistance of the insulating layer on energy savings was investigated. With a well-designed ventilated façade, Ciampi demonstrates that a 40% energy savings can be realized; the energy savings increase as the indoor to outdoor temperature difference decreases. In the experimental study by Balocco and Colombari (2006), a non-dimensional analysis is performed on a mechanically ventilated double-façade. As part

of the analysis, 12 non-dimensional values were calculated and experimental data was used for validation. Balocco proposed non-dimensional values be used to evaluate the thermal performance of ventilated façades at various aspect ratios with and without shading devices.

The effects of wind on double façades are very important and much less predictable than buoyancy forces. One of the complications is due to the effects of varying terrain on the atmospheric boundary layer. The development of a boundary layer occurs faster for areas with large open expanses as compared to areas with many buildings such as large cities (Figure 2.8). Nonetheless, various attempts have been made to model wind effects. Gratia and De Herde (2004) modelled wind effects for buoyancy-driven flows using pressure coefficients to calculate the air flow (within the GDF) due to wind. The investigation focused on the effects of wind direction and solar gain on air temperature, flow rate and flow direction within the cavity using meteorological data from Belgium. According to their model, wind effects often dominate (over the stack effect) during the night, resulting in a reversed flow. During periods of high solar gain, stack effects were dominant. The degree to which wind or stack effects dominated was dependent on the orientation of the façade.

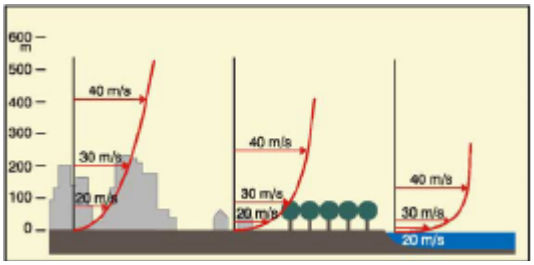

Figure 2.8: Boundary layer development as a function of terrain (reproduced from Gratia and De Herde, 2004).

2.3.2 Active Envelopes

Many studies have been performed on glazing systems with internal shading devices. For example, laminar natural convection for windows with between-the-panes venetian blinds has been studied by Tasnim and Collins (2004). The absorption of solar energy at each of an n-layer glazing/shading array has been studied by Wright and Kotey (2006). The errors associated with traditional methods of calculating performance indices of windows was investigated by Collins and Wright (2006). These studies however are for closed cavities where wind effects are insignificant. In open cavities wind can sometimes dominant the buoyancy forces.

Active envelopes are defined as glass double façades with the addition of a between-the-pane shading device (Saelens and Hens, 2001). This window system has all the same functions of a GDF with the additional benefit of controlling daylighting which provides better control over solar gains. The addition of a shading layer decreases the U-value of the fenestration system, making the system more energy efficient.

Heinrich Manz (2004) modelled active envelopes with free convection using two different modelling aids: WINDOW (1994) and FLOVENT (2001). The WINDOW software was used to acquire the spectral data required for the CFD model. FLOVENT was used to perform the transient analysis of a one-story GDF building with shading devices. The shading device used for the experimental analysis was a stationary metallized shading screen. Manz investigated two different experimental setups, both triple glazed. The sole difference was that a low-E glazing was used as the first layer in one case and a solar protective low-E glazing in the other. Temperatures in excess of 80°C were observed in the top of the cavity during days of high solar irradiance and high outdoor temperatures. The author warns that such temperatures could cause damage to

shading devices controlled by an electric motor. The author also noted that by changing the sequence of the given sets of layers, the total solar transmittance could change by as much as a factor of five.

In order to validate their proposed equations for modelling wind effects in an active envelope, Saelens and Hens (2001) used the Vliet building at the Laboratory of Building Physics in Leuven, Belgium. With a roller blind as the shading mechanism, the authors modelled the effects of wind and temperature difference in separate analyses. Having modelled each effect separately, the authors unified the two models to predict the pressure difference (ΔP) in the airflow cavity due to both wind and buoyancy. For wind speeds less than 1 m/s the following relationship was proposed:

$$\Delta P = 0.033 \cdot \Delta T - 0.011 \cdot W^2 \qquad \textbf{(2.3)}$$

where ΔT is temperature difference and all other variables are as previously defined. For higher wind speeds, the authors cautioned that only a detailed knowledge of the pressure distribution on a specific building can be used as an adequate input to the predictive model. The experimental data revealed that an upward flow occurred 90% of time in the summer and 73% of the time in the winter, thus confirming Gratia's (2004) findings of a reversed flow during periods of reduced solar gain.

The Effects of Operable Shading Devices: The aforementioned research of active envelopes pertains to airflow systems for which the shading devices are non-operable. However, research on operable shading devices, like slats for example, has also been performed; most of this research pertains to closed cavities.

Research on slats has been performed for many different regions since the impact of the shading device will vary with geographical location. Rheault and Bilgen (1989)

performed research pertaining to the Canadian climate with regards to venetian blinds hermetically sealed between two glazings. In this particular study, Rheault revealed that with the use of an automated blind system, up to 36% and 47% of the predicted HVAC load required for a Canadian climate could be saved during the winter and summer, respectively. The same authors later verified these claims experimentally (Rheault and Bilgen, 1990). A similar analysis was performed for the South Korean climate by Cho et al. (1995). Using the computer program TRNSYS, the authors determined that between-the-pane venetian blinds could help reduce the heating and cooling load of a building by 5% and 30%, respectively.

One of the main properties of shading devices that affect the windows U-value is the geometry. The geometrical effects of venetian blinds on window performance were studied by Ye et al. (1999) as a follow-up to the experimental work of Machin et al. (1997). In this study, Ye developed a numerical model to assess the influence of blind-to-wall spacing (denoted by d in Figure 2.9) as well as slat angle (θ). The numerical simulations were carried out for slat angles of 0°, 45°, 80° and -45° using a 2-D finite element model with free convection. Some of the assumptions for the model were that all of the surfaces can be considered isothermal and radiation exchange can be neglected. Ye found that the blind-to-wall spacing had a strong influence on the heat transfer except at sufficiently far distances from the wall where the blinds presence was not felt (Figure 2.10). The slat angle also had a larger impact on the heat transfer at a small blade-to-plate spacing; the authors observed a 13% drop in average heat transfer coefficient for a slat angle of -45° compared to 45°.

Very few studies, including the ones previously mentioned, investigate the effects of shading devices in airflow windows with forced convection. One of the few studies

that did was carried out by Safer et al. (2005). The authors used 2-D and 3-D numerical models to explore the effects of slat tilt angle, blind position and air outlet position on the flow dynamics and heat transfer. In order to reduce the number of nodes required for the 3-D model, Safer modelled the venetian blind as a homogeneous porous media. Congruent with the findings of Ye et al. (1999), Safer demonstrates that the distance between the blind and the external glazing has a very significant effect on both the air velocity and heat transfer. From the results of the 2-D model, the authors conclude that the optimal location for the blind in a double façade is next to the internal glazing. This ensures that the air velocity (and heat transfer) along the external glazing is high which will help reduce solar gains. The other advantage for the case where the blind is located near the internal glazing is that the tilt angle of the slat has only a small effect on airflow which means the occupant can choose any angle that may be visually appealing without compromising the thermal performance of the window.

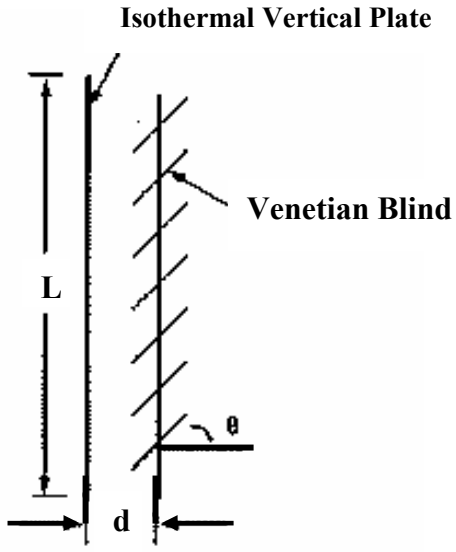

Figure 2.9: Schematic of model used by Ye et al. (reproduced from Ye et al., 1999).

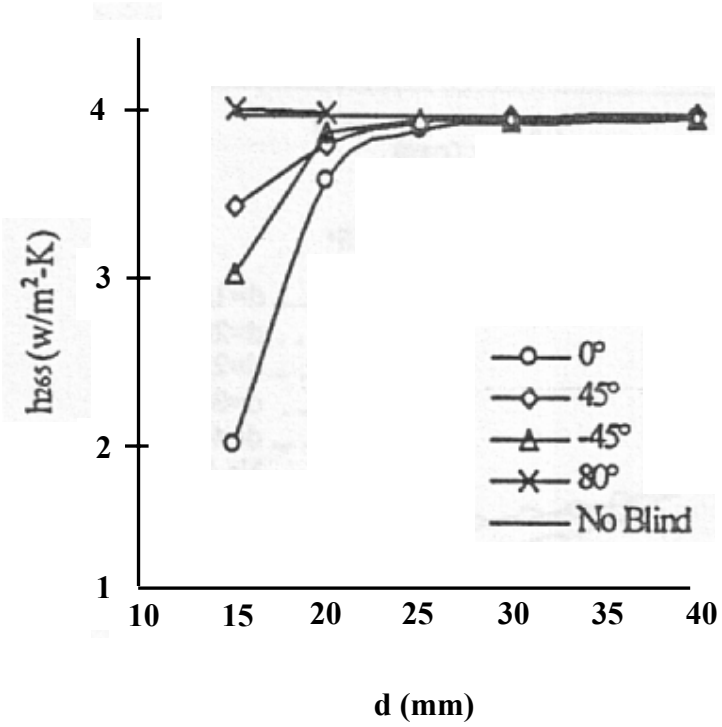

Figure 2.10: Average heat transfer coefficient as a function the distance between the wall and the blind for various blind angles (reproduced from Ye et al., 1999).

2.4 Concurrent Research

In 1997, Concordia University built the Solar Laboratory consisting of an outdoor building-integrated photovoltaics and thermal test facility (Figure 1.2). The purpose of the facility is to provide experimental data of an actual BIPV/T system which can be used to support the development of analytical and numerical models. In the end, the objective is to use the numerical models to optimize the BIPV/T system. Currently, the optimization of a BIPV/T system like the one at the Solar Lab has never been done. To date, any attempt at optimizing such a system has been done with either over-simplified boundary conditions or over-simplified energy models.

2.4.1 BIPV/T Set-up

The Solar Energy Laboratory is comprised of two different BIPV systems, both of which have been integrated with airflow windows. Both configurations provide electric and thermal energy and both have between-the-panes shading devices to control daylighting. The exterior surface of configuration 1 (Figure 1.3a) is comprised of a glazing and a PhotoWatt solar panel. Directly behind the solar panel in the lower section of the BIPV/T system is an insulation layer; a 92 mm air gap separates the two layers. In the upper section, a motorized roller blind fills the air gap which is enclosed with a second glazing.

Configuration 2 (Figure 1.3b) differs from Configuration 1 in several ways. The exterior surface of this second configuration is comprised entirely of a glazing. The solar panel, which is a Spheral PV panel, is located in the bottom half of the cavity behind the exterior glazing and in front of the insulation layer. In this configuration, a between-the-pane Venetian blind separates the internal and external glazings of the upper section.

For ease of control, both configurations have been integrated into a common building. The ducting systems are the same for both BIPV/T systems; air is drawn through a damper from the outside using a computer operated variable speed fan. The air intake is located at the base of the airflow windows and the volume of air entering the inlet is controlled by motorized dampers. Both BIPV/T systems use low-E coatings as part of their glazings and both cavities have the same height and length. The data acquisition system comprises particle image velocimetry (PIV) equipment, thermocouples, pressure sensors, weather sensors and control systems; a description of each is provided in Chapter 3.

2.4.2 Model Descriptions

To date, three models have been used to study the fluid dynamics and thermal behavior of the bottom portions of Configuration 1 and 2. The first model, developed by Charron (2004) was a 1-D model. The second model was a 2-D model which divides the cavities into control volumes and was developed by Charron and Athienitis (2003). Finally, a 2-D CFD model developed by Liao (2005) is used to provide an in-depth analysis of the flow within the lower portion of Configuration 1 as well as to validate the aforementioned models.

1-D Model: The first model of the BIPV/T system at Concordia University was a 1-D analysis of the bottom half (Figure 2.11) of the BIPV/T system (Charron, 2004). The 1-D model, in which all surfaces were assumed to be isothermal, was used as a basic predicting tool for the thermal behavior of the BIPV. This simple model was used to determine the temperature of the PV panel and insulation. Moreover, a mathematical expression for the air temperature inside the cavity as a function of height was derived. In order to determine the surface temperatures, a simple heat flow resistance network was employed.

An example of the resistance network used for the 1-D model applied to the bottom section of Configuration 1 can be seen in Figure 2.12. For this model, a single thermal conductivity coefficient (U) was used for both surfaces within the cavity. Furthermore, the long wave radiation was modelled by linearizing the radiation heat transfer equation. It should also be noted that the heat transfer to the room through the insulation is considered negligible. The expressions for the temperature of the PV and the insulation were therefore as follows:

$$T_b = \frac{T_{ma} \cdot U_b + T_R \cdot U_3 + T_{PV} \cdot U_r}{U_R + U_b + U_r} \tag{2.4}$$

$$T_{PV} = \frac{U_{out} \cdot T_{out} + U_a \cdot T_{ma} + U_r \cdot T_b + S'''_{PV}}{U_{out} + U_{ac} + U_r} \tag{2.5}$$

where the subscripts *ma, b, R, r, out* and *ac* stand for mean air, back suface (*B*), room, radiation, outside and airflow cavity. The volumetric source term is defined as *S'''*. The air temperature inside the cavity was determined to be an exponential function of the distance from the entrance of the cavity as follows:

$$T(x) = \frac{T_{PV} + T_B}{2} + \left[T_{out} - \frac{T_{PV} + T_B}{2} \right] \cdot e^{\frac{-2Y}{a}} \tag{2.6}$$

$$a = \frac{m \cdot C \cdot \rho}{w \cdot h} \tag{2.7}$$

where *w, h* and *Y* are the façade width and average heat transfer coefficient in the Y-direction (*Y*), respectively.

2-D Model: A more detailed analysis was performed using a two-dimensional control volume approach. Assuming a quasi-equilibrium state, an energy balance was performed at each control volume. The energy equation for the fluid (Eq. 2.8) (Figure 2.13) and solid (Eq. 2.9) (Figure 2.14) control volumes, respectively, were as follows:

$$0 = h_1 \left(T_i - T_j \right) dA + h_2 \left(T_k - T_j \right) dA + MC \left(T_{j-1} - T_j \right) \tag{2.8}$$

$$0 = S'''_i + q_{r,i} dA - \frac{k_i w dy_1}{dx} \left(2T_i - T_{i+1} - T_{i-1} \right) - h_{out} \left(T_i - T_{out} \right) dA - \left[\frac{0.5 dy_1}{k_i dA} + \frac{0.5 dy_2}{k_j dA} \right]^{-1} \left(T_i - T_j \right) \tag{2.9}$$

where *k* and *q* are the thermal conductivity and heat flow, respectively, and all other variables are as previously defined. The subscripts *i* and *j* represent the i^{th} and j^{th} components. It should be noted that the energy balance for the solid control volume has

been performed assuming a solid element on one side and fluid on the other. One of the improvements of the 2-D model is that a local heat transfer coefficients is used to model the convection as opposed to an average value, as was the case in the 1-D model. Furthermore, a radiosity analysis was performed to calculate the effects of long wave radiation. At each control volume, the absorbed radiation is the difference between the outgoing and the incident radiation as follows:

$$q_{abs} = q_{out} - q_{in} \tag{2.10}$$

where

$$q_{out} = \varepsilon\sigma T^4 + \rho q_{in} \tag{2.11}$$

$$q_{in} = \sum_{j=1}^{N} F_j q_j \tag{2.12}$$

where ε, ρ, F, are the emissivity, reflectivity and view factor, respectively. The subscripts *abs*, *out, in, and j* indicate the absorbed, incoming, outgoing and external surface portions of the radiation. As the radiosity analysis is non-linear, Broyden's method for solving non-linear systems of equations was required. Additional improvements to the 2-D model include the incorporation of thermal conduction effects in the vertical direction.

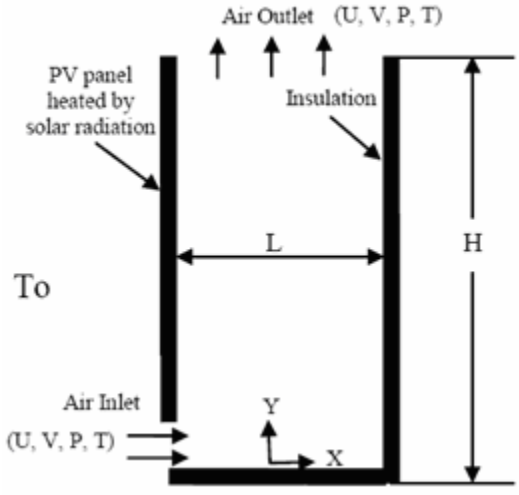

Figure 2.11: Schematic of the lower section of Configuration 1 (reproduced from Liao et al., 2005).

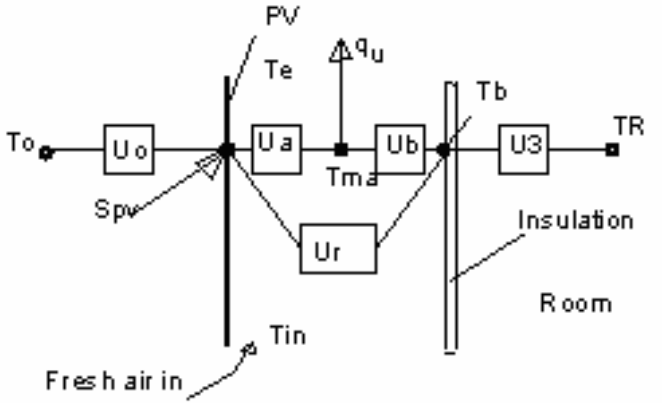

Figure 2.12: Resistance network used for 1-D model (reproduced from Athienitis et al., 2004).

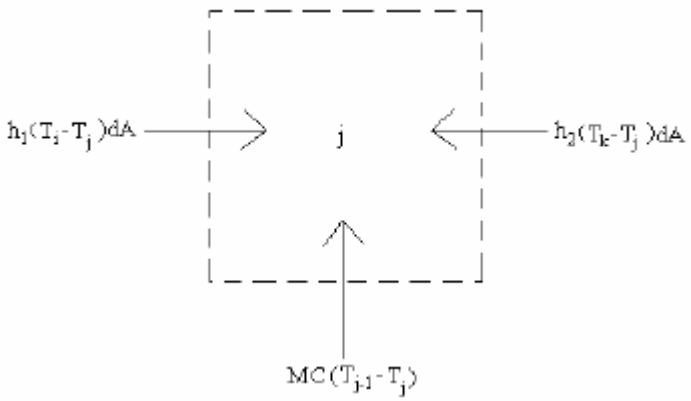

Figure 2.13: Elemental fluid control volume (reproduced from Charron and Athienitis, 2003).

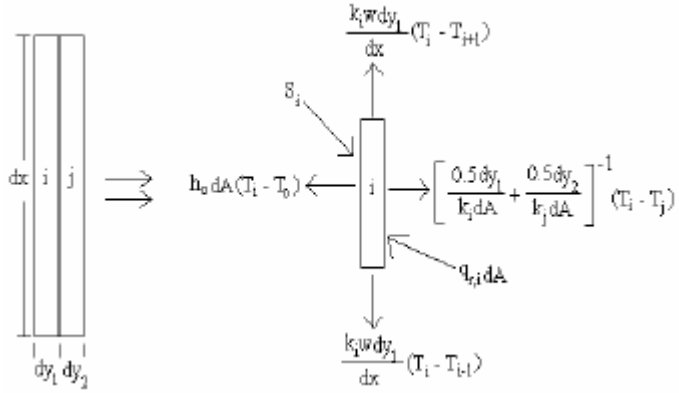

Figure 2.14: Elemental solid control volumes (reproduced from Charron and Athienitis, 2003).

In order to compare the differences between the 1-D and 2-D model, thirteen different environmental scenarios were applied to Configuration 2 (Table 2.1) whereby each

scenario differs from its predecessor by only one parameter. The results (Charron and Athienitis, 2003) from both models were then compared. One of the observations put forth by the authors was that the use of a linearized radiative heat transfer coefficient had minimal impact on the results. This was an important discovery as the radiosity analysis requires matrices to solve the system of non-linear coupled equations which are computationally expensive. Furthermore, it was determined that the effects of vertical conduction was negligible for all cases. Most of the large differences in the results, where they existed, could be attributed to the use of local versus average heat transfer coefficient. One of the major advantages of the 2-D model is the generation of a more accurate temperature profile for the PV section, which has implications for both the electrical and system efficiencies, defined as follows:

$$\eta_{electric} = \frac{P_{electric}}{q \cdot A_{PV}} \cdot 100\% \quad \textbf{(2.13)}$$

$$\eta_{system} = \frac{Q_{thermal} + P_{electric}}{q \cdot A_{PV}} \cdot 100\% \quad \textbf{(2.14)}$$

where η is the efficiency while $Q_{thermal}$ and $P_{electric}$ are the thermal energy and electric energy generated by the system. Although the 2-D model provides more accurate results, there continues to be major limitations to both models. For example, in order to generate temperature profiles, the knowledge of many parameters, often times unknown, were required. Ideally, only indoor and outdoor wind speeds, ambient temperatures and the specification of solar irradiation would be required as a full set of input parameters for a fully functioning model. Such a model can only be achieved through the use of CFD.

CFD Model: The third model that was developed at Concordia University was a numerical model. A CFD software, called FLUENT, was used to model (Liao, 2005) the

lower portion of Configuration 1. After performing an experimental investigation, it was determined that the flow could be accurately modelled using a 2-D numerical analysis. The geometry of the lower section of Configuration 1 is as shown in Figure 2.11 where the lengths L and H have dimensions 0.092 m and 1 m, respectively. The lower section of Configuration 1 can be subdivided into four regions: inlet, outlet, insulation and PV. The inlet air was modelled with a uniform and isothermal profile. The inlet velocity ranges from 0.5 m/s to 1 m/s depending on the speed setting of the fan. The outlet boundary condition was specified as a zero-pressure boundary. The velocity and temperature profiles at the outlet region are extremely important as they will be used as inputs to the upper AFW section. The surface with insulation was modelled as a smooth, adiabatic boundary with a no-slip condition. In order to model the PV surface, thermocouples were used to measure the temperatures along the back of the panel. The experimental temperature data was used to generate a continuous temperature profile. This profile was used as the temperature boundary condition along the PV. The PV was also modelled as a smooth wall with a no-slip boundary condition. The mesh that was used in FLUENT can be seen in (Figure 2.15). The fine mesh at the mall was used to resolve the steep near-wall gradients.

Given the inherent limitations of modelling, there are certain unavoidable discrepancies between the model and the Solar Lab results. For example, the entire lower cavity was assumed to be air tight, however air leakage is unavoidable. Furthermore, all surfaces were modelled as smooth when in reality all of the surfaces have some degree of roughness. Perhaps the largest variable pertains to the outside conditions and in particular the effects of wind on the air speed. The direction and magnitude of the wind near the inlet will greatly affect the airflow speed and direction through the inlet and into

the cavity. As was previously discussed in this thesis, wind perturbations are extremely difficult to model.

Scenario	h_o (W/m^2K)	G (W/m^2)	T_o (°C)	V_{front} (m/s)	V_{back} (m/s)	L_{front} (m)	L_{back} (m)	Blind #	L_{fin} (m)
1	12.91	600	20	1	1	0.05	0.05	1	n/a
2	12.91	600	20	1	1	0.05	0.05	2	n/a
3	12.91	600	20	1	1	0.05	0.05	3	n/a
4	12.91	600	20	1	1	0.05	0.05	4	n/a
5	25	600	20	1	1	0.05	0.05	1	n/a
6	12.91	600	20	1	1	0.05	0.05	1	0.015
7	12.91	100	20	1	1	0.05	0.05	1	n/a
8	12.91	600	20	0.5	0.5	0.05	0.05	1	n/a
9	12.91	600	20	2	2	0.05	0.05	1	n/a
10	12.91	600	20	1	1	0.025	0.025	1	n/a
11	12.91	600	20	1	1	0.15	0.15	1	n/a
12	12.91	600	-20	1	1	0.05	0.05	1	n/a
13	12.91	1000	20	1	1	0.05	0.05	1	n/a

Table 2.1: Parametric analysis comparing 1-D and 2-D model (reproduced from Charron, 2004).

When the air enters the bottom of the cavity via the inlet, it is traveling in the x-direction (Figure 2.11). Having crossed the inlet, the air is then forced to make a 90° turn. This direction change causes the air at the bottom to accelerate around the corner while the air near the top of the inlet is almost stagnant; a potential separation point exists at the bottom of the PV (as predicted by the CFD model in Figure 2.16). Downstream of the inlet (y = 1 m), at a velocity of 0.5 m/s, a peak in the velocity profile near the PV where the temperatures are greatest was predicted by the simulation (Figure 2.17). This buoyancy-induced peak indicates that at an inlet velocity of 0.5 m/s, the flow is characterized by mixed convection. However, beyond an inlet velocity of 0.5 m/s, forced convection can be seen to dominate. The cooling effect on the PV can be measured by

the heat transfer coefficient near the PV wall. Although high inlet velocities increase the heat transfer coefficient along the PV, a large inlet velocity results in a corresponding increase in pressure drop. If a large pressure drop exists, a larger fan will have to be used resulting in greater electrical needs. A large fan may therefore offset the benefits of the increased thermal gains of the system.

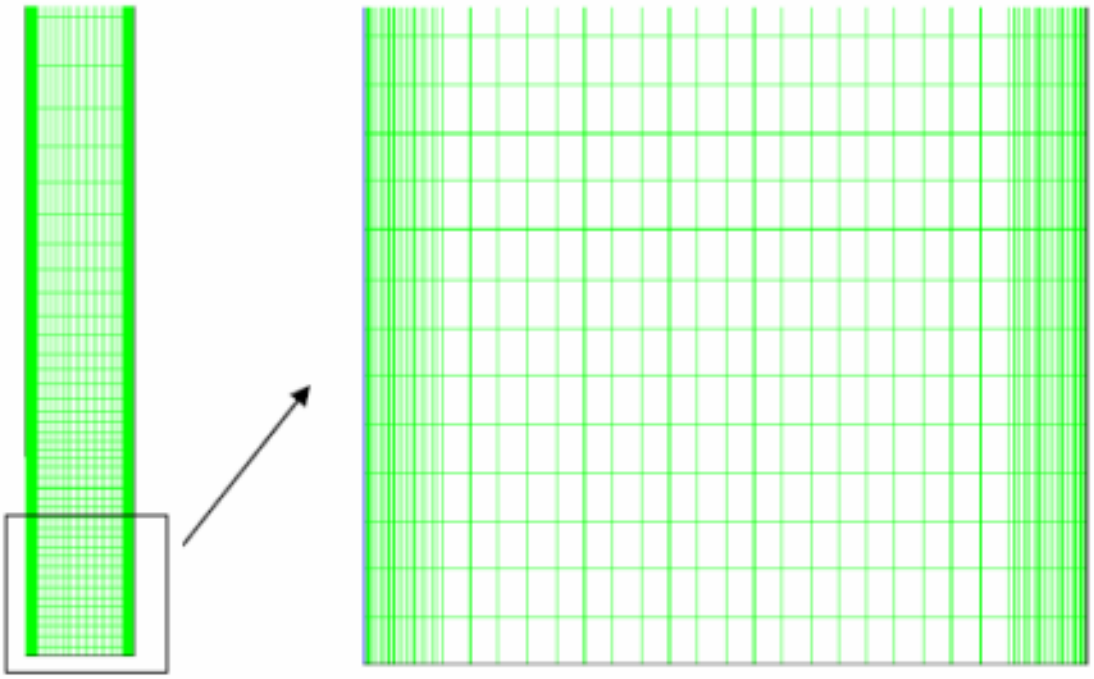

Figure 2.15: Mesh used by Liao (2005) to model bottom section of BIPV/T system (reproduced from Liao, 2005).

The potential separation zone, as identified by a CFD analysis (Liao, 2005) was later confirmed from experimentation. Vortex structures near the cavity inlet for fan frequencies of 15 Hz (mean velocity of 0.5 m/s) and 30 Hz (mean velocity of 1 m/s) were observed. For both cases, the recirculating flow was due to the flow having to suddenly turn the corner of the entrance region. For the 15 Hz case, the vortex was small and produced no noticeable backflow. With a fan speed of 30 Hz, backflow at the inlet was clearly noticeable (Figure 2.17).

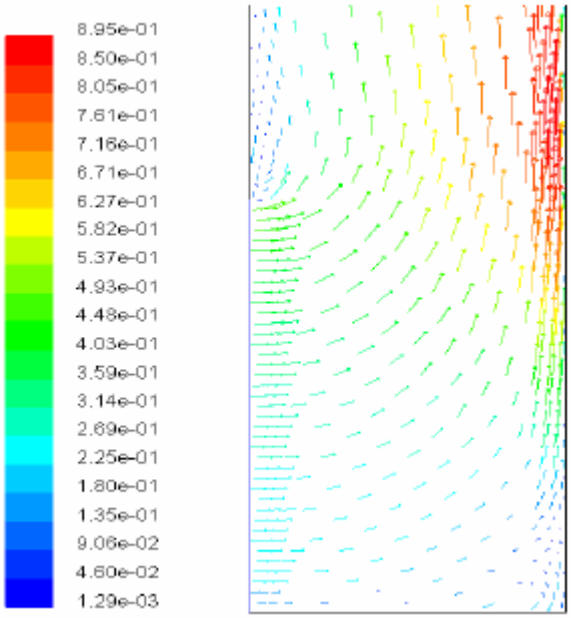

Figure 2.16: Velocity vectors produced from CFD analysis demonstrating stagnation point at the top of the inlet (reproduced from Liao, 2005)).

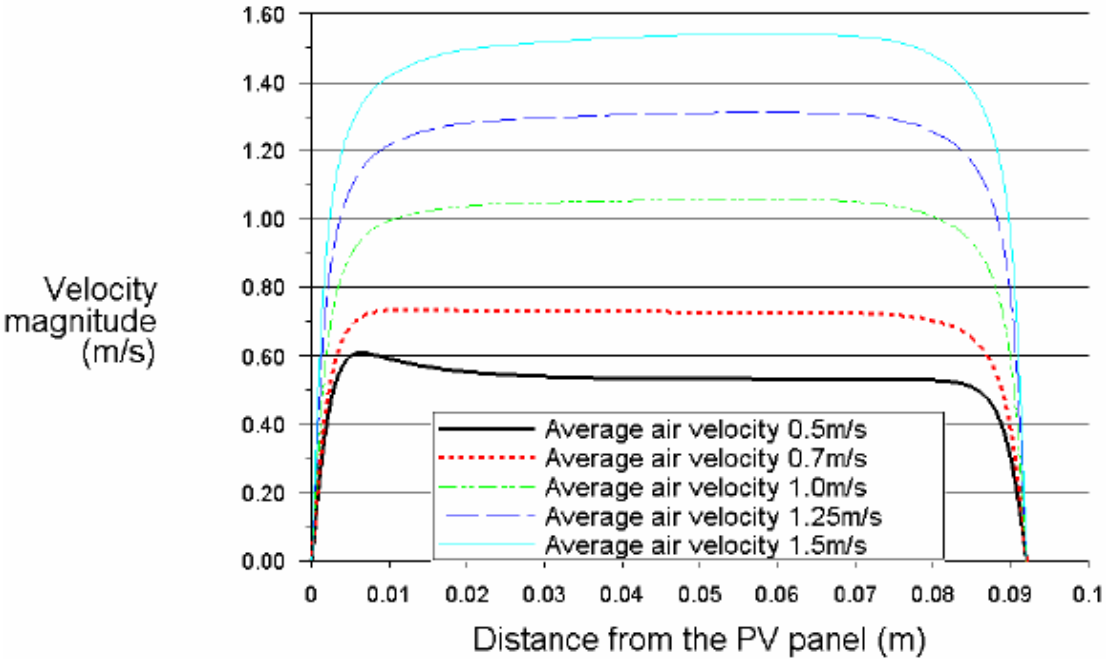

Figure 2.17: CFD Velocity profiles as a function of inlet velocity (reproduced from Liao, 2005).

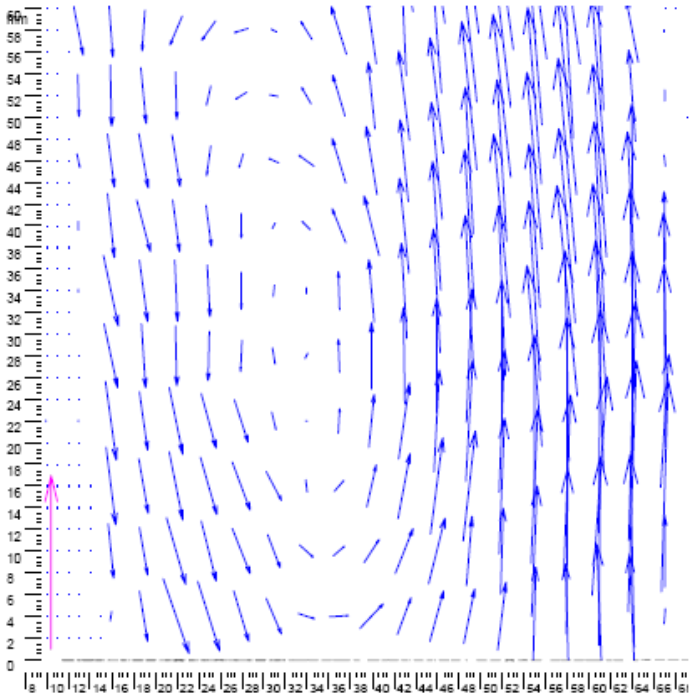

Figure 2.18: Vortex structure near inlet captured by PIV for a mean velocity of 1 m/s (reproduced from Liao, 2005).

Chapter 3

Model Development and Validation

3.1 Introduction

This chapter describes the development of the numerical model used to analyze the flow dynamics and heat transfer inside the AFW of the Concordia University BIPV/T system (Configuration 1 of Figure 1.2). The numerical modelling was accomplished using the computational fluid dynamics (CFD) software FLUENT (version 6.2), which employs the finite volume method to solve the governing conservation equations. A grid-sensitivity analysis was performed during a three-stage validation procedure. In the first stage, a numerical model for flow between parallel plates without radiative heat transfer was developed and compared to analytical solutions for both laminar and turbulent flow. In the second stage of validation, radiative heat transfer was added to the model. Software used for window analyses, called VISION, was utilized to validate the model for convective and radiative heat transfer between parallel plates for a closed cavity with buoyancy-induced convection (Wright, 1998). As part of the radiation validation, a between-the-panes shading device was added and the model was again validated using VISION. For the third and final stage, convection (forced) and radiation effects were modelled and compared to experimental data obtained from the Solar Lab at Concordia University (Liao, 2005).

3.1.1 Problem Statement

The AFW to be modelled is comprised of the following: two glazings, one between-the-panes roller blind, an inlet and an outlet (Figure 3.1). The indoor and outdoor glazings are both 21 mm thick while the between-the-panes roller blind is 0.75 mm thick and is made of a double-weave pattern. A low-E coating is present on the indoor glazing. The dimensions of the AFW in question are 1 m x 1 m x 0.092 m where the later dimension is the distance between the two glazings. As was discussed in Chapter 2, the airflow through the center of the cavity can be modelled as two-dimensional (ignoring end effects). The representative geometry is therefore a 1 m tall and 92 mm wide cavity, open at both ends where the inlet and outlet ports are modelled; the frame of this cavity can therefore be depicted as two parallel plates, 92 mm apart. The blind within Configuration 1 is located approximately 27.6 mm from the outer glazing. In its fully extended position, the blind is 1 m tall, stretching the entire length of the upper section. The ducting, located at the top of the AFW beyond the outlet of the parallel plates, is used to circulate the air into the building. As the exact geometry of this duct is not known, the outlet was simply left as an opening between the parallel plates.

3.1.2 Numerical Modelling Approach

The general approach that was used for the model development in FLUENT was to first begin with a very simple model which could be easily validated. Once the simple model was validated, sequential refinements were made, each time increasing the level of complexity. After each new addition, the validity of the model was again tested. Using this methodology, the model evolved from the simulation of laminar flow between parallel plates (without the effects of radiation) to that of turbulent flow between two

glazings with a between-the-panes shading device including the effects of conduction, advection and radiation. As was explained in Section 3.1, the validation process was achieved in three stages.

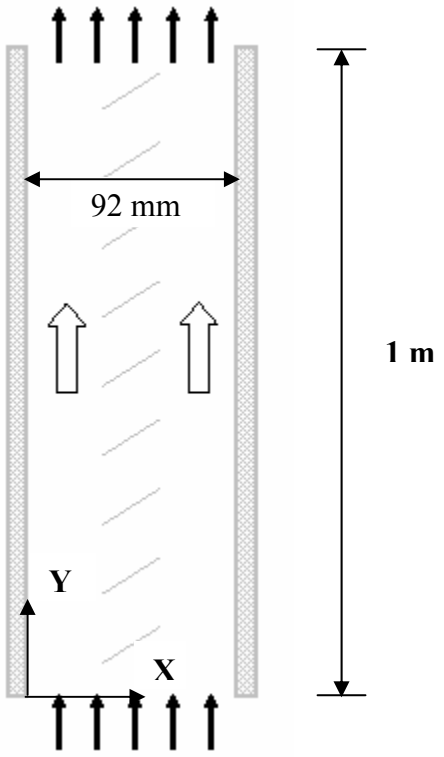

Figure 3.1: Schematic of AFW with roller between-the-pane roller blind.

3.2 Numerical Modelling Theory

The basic premise behind numerical modelling is to divide (discretize) a flow region of interest into smaller parts, called control volumes (CV's), and perform conservation calculations (refer to Section 3.2.1) for each CV. Due to modelling limitations, absolute convergence can not be achieved. Residuals across each CV are therefore calculated and used to help quantify convergence. The conservation equations, discretization process and other relevant CFD parameters employed by FLUENT are explained in subsequent sections of this chapter.

3.2.1 Conservation Equations

In general, numerical programs use conservation equations to calculate the unknown values (velocity, temperature, etc.) throughout the numerical domain. In general, for laminar flow, there are three basic conservation equations: mass, momentum and energy. Conservation of mass and momentum are applied to all problems while conservation of energy is employed only when heat transfer exists within the computational domain. For turbulent flow, additional transport equations are required; the number and the form of the transport equations will vary depending on the turbulence model (Section 3.3.3).

For a two-dimensional incompressible flow, the following steady-state mass conservation equation was used:

$$\frac{\partial u}{\partial x}+\frac{\partial v}{\partial y}=0 \qquad \textbf{(3.1)}$$

where u and v are the velocity components in the x- and y-direction, where the y-direction is in the direction of air flow. The conservation equations for x- and y-momentum, respectively, are:

$$\rho\frac{\partial(uu)}{\partial x}+\rho\frac{\partial(uv)}{\partial y}=-\frac{\partial P}{\partial x}+\frac{\partial}{\partial x}\left[\mu_{eff}\left(2\frac{\partial u}{\partial x}-\frac{2}{3}\left(\frac{\partial u}{\partial x}+\frac{\partial v}{\partial y}\right)\right)\right]+\frac{\partial}{\partial y}\left(\mu_{eff}\left(\frac{\partial u}{\partial y}+\frac{\partial v}{\partial x}\right)\right) \qquad \textbf{(3.2)}$$

$$\rho\frac{\partial(vv)}{\partial y}+\rho\frac{\partial(uv)}{\partial x}=-\frac{\partial P}{\partial y}+\frac{\partial}{\partial y}\left[\mu_{eff}\left(2\frac{\partial v}{\partial y}-\frac{2}{3}\left(\frac{\partial u}{\partial x}+\frac{\partial v}{\partial y}\right)\right)\right]+\frac{\partial}{\partial x}\left(\mu_{eff}\left(\frac{\partial v}{\partial x}+\frac{\partial u}{\partial y}\right)\right)+\rho g \qquad \textbf{(3.3)}$$

where μ_{eff} is the effective viscosity and g is the gravitational constant. A constant density was assumed throughout the numerical analysis*. The energy conservation equation is given as:

* Constant density was used throughout the modelling, with the exception of laminar flow where the Boussinesq approximation was used.

$$\rho\frac{\partial(uC_PT)}{\partial x}+\rho\frac{\partial(vC_PT)}{\partial y}=\frac{\partial}{\partial x}\left(k_{eff}\frac{\partial T}{\partial x}\right)+\frac{\partial}{\partial y}\left(k_{eff}\frac{\partial T}{\partial y}\right)+S''' \quad \textbf{(3.4)}$$

where the effective conductivity is $k_{\text{eff}} = k + k_t$ where k_t is the turbulent thermal conductivity and C_P is the specific heat capacity. The S''' term represents a volumetric heat source, such as absorbed radiation within a glazing. The energy equation is applicable for a steady-state control volume analysis involving conduction, convection and radiation. The air inside the AFW is considered to be a non-participating medium and therefore the source terms within the model are zero everywhere except at the walls. Equations specific to radiation can be seen in Section 3.4 where the radiation model is discussed.

3.2.2 Numerical Solution Methodology

Within FLUENT, a control-volume analysis was employed to transform the governing equations (Eq. 3.1 – 3.4) into algebraic equations. These algebraic equations were both non-linear and coupled. In order to solve for the unknowns, the equations were first linearized before being solved by a Gauss-Seidel solver (FLUENT, 2005). A segregated implicit solver scheme was employed to solve for the unknowns. A second order upwind scheme and second order central differencing scheme was used for advective flows and diffusive flows, respectively. During iteration, under-relaxation values were employed in order to ensure smooth convergence. After each iteration, residual values were calculated for each of the variables and were used to help quantify convergence. All equations were solved until the average scaled residual values reached 10^{-4} or below. Complete details about the discretization schemes, the under-relaxation factors, the convergence criteria, etc. have been presented in Appendix A.

3.3 Stage 1: Convection Validation

In this section, the validation process for flow between parallel plates is explained. A grid sensitivity analysis was performed to find the best grid density for modelling forced convection without considering the effects of radiation. The model validation began with the modelling of laminar flow between parallel vertical plates and was followed by a similar analysis for turbulent flow.

3.3.1 Introduction

In order to validate the model for flow between parallel plates, both a fluid dynamics and thermodynamics analysis was performed. To begin, a Nusselt (*Nu*) number analysis was used to determine the accuracy of various mesh densities for forced convection in both the laminar and turbulent flow regimes. The final grid was arrived at through a series of grid sensitivity studies. Using the temperature data obtained from FLUENT, the *Nu* values were calculated using two different equations:

$$Nu_A = \frac{\left.\frac{\partial T}{\partial x}\right|_{wall} D_h}{T_{wall} - T_m} \tag{3.5}$$

$$Nu_B = \frac{q''_{wall} D_h}{(T_{wall} - T_m)k} \tag{3.6}$$

where T_m is the mass-averaged local mean temperature between both walls:

$$T_m = \frac{\int \rho v C T}{\dot{m} C} dA_c \tag{3.7}$$

and the hydraulic diameter (D_h) is calculated as follows:

$$D_h = \frac{4A}{\wp} \tag{3.8}$$

where $\wp$ is the wetted perimeter. For the case of two parallel plates with infinite length, the hydraulic diameter is $D_h = 2w$ (White, 2003) where w is the distance between the plates (92 mm). Calculating two *Nu* numbers helped provide insight into the mesh performance, particularly in the region immediately adjacent to the wall where the velocity, temperature and shear gradients are most pronounced. With an infinitely fine grid and a perfect numerical model, Nu_A and Nu_B would be equal. Given the constraints of modelling however, one would expect that for a specified heat flux at the wall (q''_w), the value obtained from Nu_B should be more accurate as it is directly proportional to q''_w (Eq. 3.6). As the value for Nu_A is a function of the temperature gradient at the wall, the accuracy of Nu_A is dependent on the mesh density throughout the control volume (and particularly near the wall) as well as the accuracy of FLUENT's near-wall treatment methods. The value of Nu_A in relation to Nu_B was therefore used as a performance indicator for the different mesh configurations, helping quantify the accuracy of the near-wall gradients for each of the different mesh densities. Once a suitable mesh was obtained, a comparison between the analytical and the numerical velocity profiles was used to ensure accurate flow modelling.

3.3.2 Laminar Flow

Model Boundary Conditions: The parallel walls in Figure 3.1 were modelled as smooth surfaces with a no-slip boundary condition. A constant (and arbitrary) heat flux q''_w was applied to both vertical walls. A uniform velocity of 0.006 m/s was applied at the inlet boundary, corresponding to a Reynolds (*Re*) number of 70. Because the *Nu* number for a fully developed laminar flow with uniform surface heat flux is independent of the *Re* number (Kays, 1966), the only constraint was that the *Re* number had to be less than 2300

to remain in the laminar regime. The outlet boundary was defined in FLUENT as a pressure outlet with a static pressure of 0 Pa.

Meshing: In order to determine the hydraulic (Schlichting, 1979) and thermal (Kays and Crawford, 1980) entrance lengths for flow between parallel plates, the following correlations were used:

$$L_{fd,h} \approx 0.06 \,\mathrm{Re}\, D_h \qquad \textbf{(3.9)}$$

$$L_{fd,th} \approx 0.05 \,\mathrm{Re}_D \,\mathrm{Pr}\, D_h \qquad \textbf{(3.10)}$$

where *h, th* and *fd* refers to hydraulic and thermal entrance lengths and fully developed, respectively. According to Eq. 3.9 - 3.10, a fully developed flow is achieved in 0.77 m, dictated by the hydraulic entrance length. In order to ensure a nice stable flow, parallel plates of length 2 m were used for the validation. For all laminar flow models, a uniform grid density was applied throughout the solution domain.

Validation Data: In order to validate the mesh, the Nusselt (*Nu*) number at the wall was calculated using Eq. 3.5 and 3.6 and compared to published data for fully developed laminar flow. Because laminar flow between parallel plates is one of the fundamental heat transfer problems, many data sources for the fully developed *Nu* number existed (e.g. Burmeister, 1993, Rohsenow et al., 1985 and Kays, 1966). For constant axial wall heat flux, the *Nu* number is given as $Nu_{\mathrm{fd}} = 8.235$ (Rohsenow et al., 1985).

Results and Discussion: To begin the grid sensitivity study, a very coarse grid was initially used to calculate the fully developed *Nu* number. With each successive model, a

finer grid was employed and the results from each run were compared. A summary of the mesh characteristics and the resulting *Nu* numbers can be seen in Table 3.1.

Table 3.1: Fully developed Nusselt numbers for the laminar case with a uniform grid.

	Number (n) of Grid Spaces[*]		*Mesh Size*		**Results**	
Case	n_x	n_y	Δx	Δy	Nu_A	Nu_B
1	20	20	0.0046	0.1	8.177	8.239
2	40	20	0.0023	0.1	8.225	8.240
3	80	20	0.00115	0.1	8.247	8.251
4	40	40	0.0023	0.05	8.222	8.238
5	80	40	0.00115	0.05	8.232	8.237
6	80	80	0.00115	0.025	8.239	8.242
7	80	320	0.00115	0.00625	8.196	8.200

Note that the fully developed *Nu* values in Table 3.1 were calculated from numerical data taken 1.5 m upstream of the inlet; some variations in the *Nu* number were detected beyond the 1.9 m mark where end effects can affect data integrity. It can be seen from Table 3.1 that all mesh densities produce *Nu* numbers that are relatively close to the published value of 8.235 (Rohsenhow et al., 1985) with the Nu_B values being slightly more accurate than the Nu_A values. For both Nu_A and Nu_B, the mesh with 80 grid spaces in either direction appears to produce the most accurate results. No tangible benefits were realized when using more than 80 grid spaces in either the x- or y-direction. Moreover, it was observed that as the grid density increased, the *Nu* numbers began to deviate from the target value (especially for Nu_A) while the convergence time lengthened. These findings indicate that FLUENT operates best within a certain mesh-density range, which will be further discussed in Section 3.3.3.

The accuracy of the grid was also verified by comparing the fully developed velocity and temperature profiles of the numerical solution (Case 4 of Table 3.1) to

* n_x and n_y are the number of control volumes in the x and y direction, equivalent to $W/\Delta x$ and $L/\Delta y$, respectively.

profiles generated from analytical solutions. The analytical profiles can be expressed mathematically as:

$$u(y) = U_0\left(1 - \frac{y^2}{w^2}\right) \tag{3.11}$$

$$T(y) = \frac{3}{2} q_0'' \frac{w}{k}\left(\frac{y^2}{2w^2} - \frac{y^4}{12w^4} - \frac{5}{12}\right) + T_0 \tag{3.12}$$

as determined by a momentum and energy balance. It can be seen from Figures 3.2 and 3.3 that the temperature and velocity profiles obtained from FLUENT are in excellent agreement with the analytical profiles.

3.3.3 Turbulent Flow

Using the knowledge gained from the development of the laminar grid, a mesh for turbulent flow was then developed. As was the process for the laminar grid validation, a systematic grid sensitivity analysis was performed using the same fully developed *Nu* number analysis. Additionally, a *Nu* number analysis for developing flow was also used.

Model Boundary Conditions: Both wall surfaces were again modelled as smooth with a no-slip boundary condition. A *Re* number of 7,104 was chosen for the turbulent validation due to the preponderance of data at that *Re* number. A fully developed profile with a mean inlet velocity of 0.564 m/s was used at the inlet. A constant temperature boundary condition was also applied at the inlet. For fluid entering a duct, the use of constant turbulence values such as turbulent kinetic energy (κ), specific dissipation rate (ω) (for κ-ω model) or turbulent dissipation rate (ϵ) (for κ-ϵ model) was appropriate (FLUENT, 2005) and as such the default values for turbulence were used throughout the validation. An arbitrary uniform heat flux q''_w was applied on one wall only while the

other wall was modelled as adiabatic. The walls were assigned zero thickness; no conduction or heat generation was modelled. The *outflow* boundary condition was used at the outlet; all of the relevant values at the outlet were thus extrapolated from information within the interior of the solution domain.

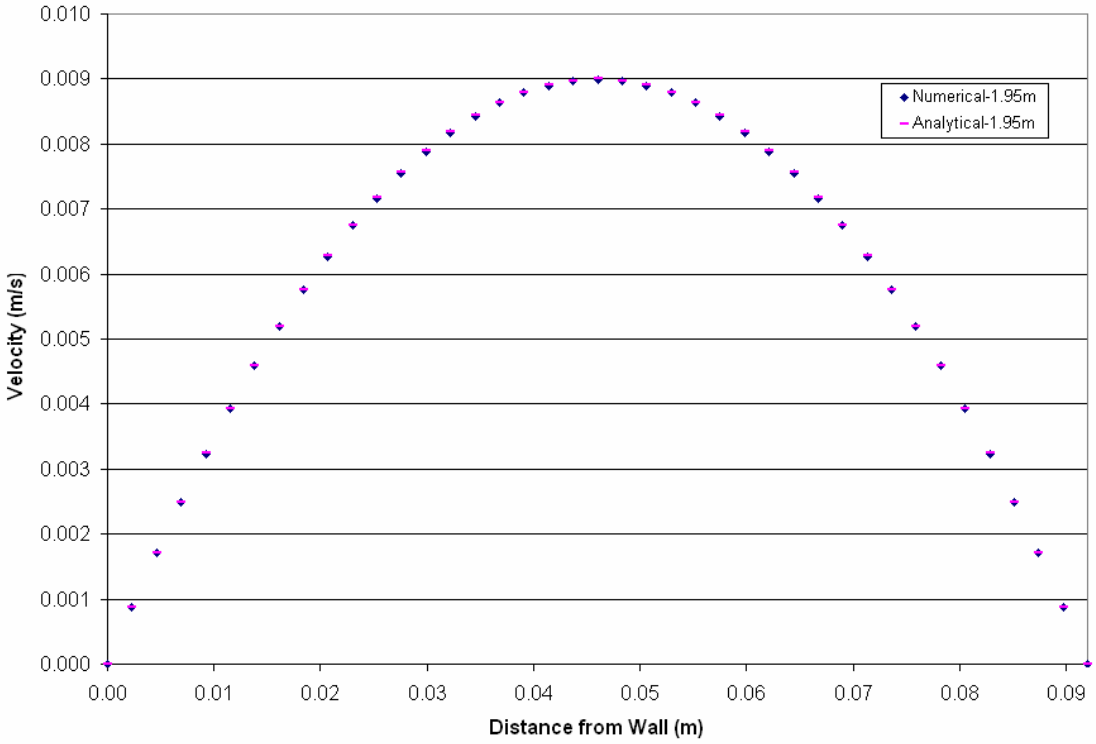

Figure 3.2: Velocity profile through cavity comparing numerical results to analytical results.

Meshing: The following approximations were used to help determine the entrance length for turbulent flow between parallel plates:

$$10 \le \frac{L_{fd,h}}{D_h} \le 60 \qquad \textbf{(3.13)}$$

$$L_{fd,t} \approx 4.4\,\mathrm{Re}_D^{1/6}\,D_h \qquad \textbf{(3.14)}$$

As determined from Eq. 3.13 (Kays and Crawford, 1980), the hydrodynamic entrance length can vary from approximately 1 m to 6 m. The thermal entrance length (White, 2003) was calculated to be approximately 4 m. As was done for the laminar case,

approximately double the required plate length (i.e. 10 m) was used for modelling to limit the influence of end effects on the results.

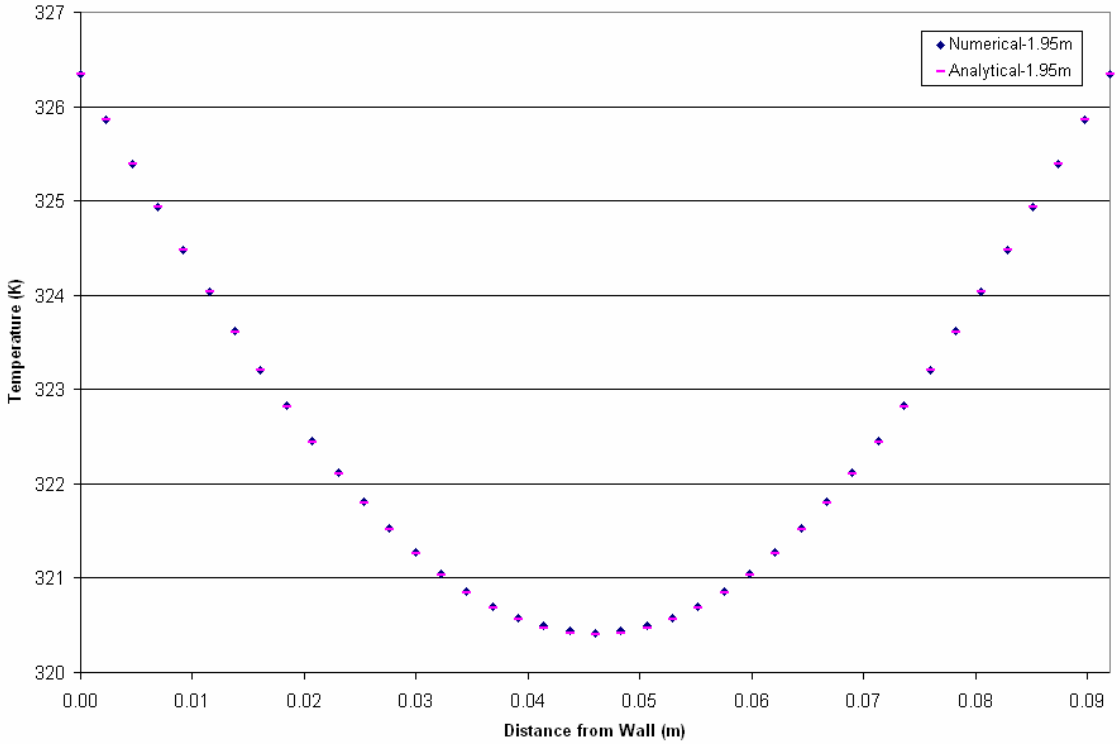

Figure 3.3: Temperature profile through cavity comparing numerical results to analytical results.

Validation Data: Unlike laminar flow, *Nu* data for turbulent flow cannot be derived analytically. Amongst the relevant literature, a large portion of the data is numerical. In this thesis, all of the flow validation was performed using uniform heat flux on one side and insulation on the other. Of the four fundamental solutions (Lundberg et al., 1963), this type of boundary condition best represented the actual case. Data from Azer and Choa (1960) and Hatton and Quarmby (1963) was used for a Prandtl (*Pr*) number of 0.7 and a *Re* number of 7104.

Modelling Approach: Within turbulent flow, many different scales of turbulent fluctuations exist, creating a modelling challenge. Numerically resolving all scales of

turbulent fluctuations cannot be achieved expeditiously and would require extreme computing power, neither of which is practical for most CFD applications. In order to provide timely results without requiring a super-computer, basic shortcuts are required. Within FLUENT, two such shortcuts exist for solving the Navier-Stokes (NS) equations for turbulent flow: Reynolds averaging and filtering methods (FLUENT, 2005). Filtering, also known as large eddy simulation (LES), is typically very computationally expensive as it requires a very fine mesh compared to the Reynolds-averaged Navier-Stokes (RANS) method. As the name implies, the LES method only resolves the large scale eddies while the smaller scale eddies are filtered (mathematically removed) from the governing equations. The RANS method models turbulence by modelling the transport of averaged flow quantities, which drastically reduces the required computer memory and CPU resources. Due to time and computing constraints, the RANS method was used throughout this thesis to model turbulence phenomenon.

Using a Reynolds-averaged solution, all variables in the NS equations are expressed as the sum of the mean and fluctuating components. The velocity components are therefore expressed as:

$$u_i = \bar{u}_i + u_i' \tag{3.15}$$

where i represents one of the three directional components. The scalar terms (e.g. pressure, energy) are expressed mathematically as:

$$\phi = \bar{\phi} + \phi' \tag{3.16}$$

It follows from Eqs. 3.1 and 3.2 that the turbulent governing transport equations for continuity and momentum, respectively, become:

$$\frac{\partial}{\partial x_i}\left(\rho \bar{u}_i\right) = 0 \tag{3.17}$$

$$\frac{\partial}{\partial x_j}\left(\rho \bar{u}_i \bar{u}_j\right) = -\frac{\partial p}{\partial x_i} + \frac{\partial}{\partial x_j}\left[\mu\left(\frac{\partial \bar{u}_i}{\partial x_j} + \frac{\partial \bar{u}_j}{\partial x_i} - \frac{2}{3}\delta_{ij}\frac{\partial \bar{u}_i}{\partial x_i}\right)\right] + \frac{\partial}{\partial x_j}\left(-\rho\overline{u_i' u_j'}\right) \qquad \textbf{(3.18)}$$

where δ is the Kronecker Delta function which is equal to one only when $i = j$. The use of the RANS method results in the addition of new terms in the governing equations called "Reynolds stresses" ($-\rho\overline{u_i' u_j'}$). In order to reduce computation time, the Boussinesq approximation was used to solve the Reynolds stresses as follows:

$$-\rho\overline{u_i' u_j'} = \mu_t\left(\frac{\partial u_i}{\partial x_j} + \frac{\partial u_j}{\partial x_i}\right) - \frac{2}{3}\left(\rho k + \mu_t \frac{\partial u_i}{\partial x_i}\right)\delta_{ij} \qquad \textbf{(3.19)}$$

The Boussinesq approximation introduces an extra term called the turbulent viscosity, expressed as μ_t. This term is computed as a function of two other variables, either κ and ω or κ and ϵ, depending on which turbulent model is employed. The differences between the κ-ω and the κ-ϵ models are discussed in the next sections.

Turbulence Models: Within FLUENT, seven different models exist for modelling the transport equations for turbulent flow. Of the seven models, the κ-ϵ and κ-ω as well as their variants represent five of those models. A comparison between the two models and their variants was therefore undertaken.

κ-ϵ versus κ-ω Model

In FLUENT, three variations of the κ-ϵ model are offered: *standard* κ-ϵ, *RNG* κ-ϵ and *realizable* κ-ϵ model. According to the FLUENT literature (FLUENT, 2005), the *realizable* model outperforms the *standard* model for separated flows involving complicated secondary flow characteristics whereas the *RNG* model is most applicable to rapidly strained flows. Neither separated flow regions nor rapidly strained flow regions

exist in the current AFW model and therefore, of the three κ-ϵ variations, the *standard* κ-ϵ model is best suited for the flow of interest.

Two variations of the κ-ω model exist: *standard* κ-ω and the *Shear-Stress Transport* (*SST*) κ-ω model. The *standard* κ-ω model is applicable to wall-bounded flows while the *SST* model is a mix of the standard κ-ϵ and the standard κ-ω model. In the near-wall regions, the *SST* model makes use of the *standard* κ-ω model while away from the wall, the *standard* κ-ϵ model is applied. A blending function is used to activate the appropriate model in the appropriate region and provide a mixture of the two otherwise. According to the FLUENT literature (FLUENT, 2005), all three models, namely the *standard* κ-ϵ, the *standard* κ-ω and the *SST* κ-ω models, are appropriate for modelling the given flow. As such, a mesh was developed for each of the three models and the results were compared.

Near-Wall Modelling: Experimental investigations have shown (Schlichting, 1979) that turbulence in the near-wall region can be modelled as three sublayers: viscous sublayer, buffer layer and fully-turbulent layer (Figure 3.4). The viscous sublayer is the innermost region in which the flow is almost laminar; in this layer, viscous shear forces dominate momentum and heat transfer. The fully-turbulent region is the outermost layer of the near-wall region in which turbulence effects dominate. The buffer layer, which is found between the viscous and turbulent regions, is a transition layer where viscous and turbulent effects are of similar importance.

In order to model these near-wall sublayers, FLUENT offers two different approaches: wall functions and near-wall treatments. The standard wall function (SWF) resolves the viscous sublayer and the buffer layer mathematically without requiring any

mesh in those regions. Wall functions make use of semi-empirical data to model the viscous-affected regions (viscous and buffer sublayers) (FLUENT, 2005). Near-wall treatments on the other hand require a very particular mesh near the wall in order to resolve the viscous sublayers. A schematic comparing both methods can be seen in Figure 3.5.

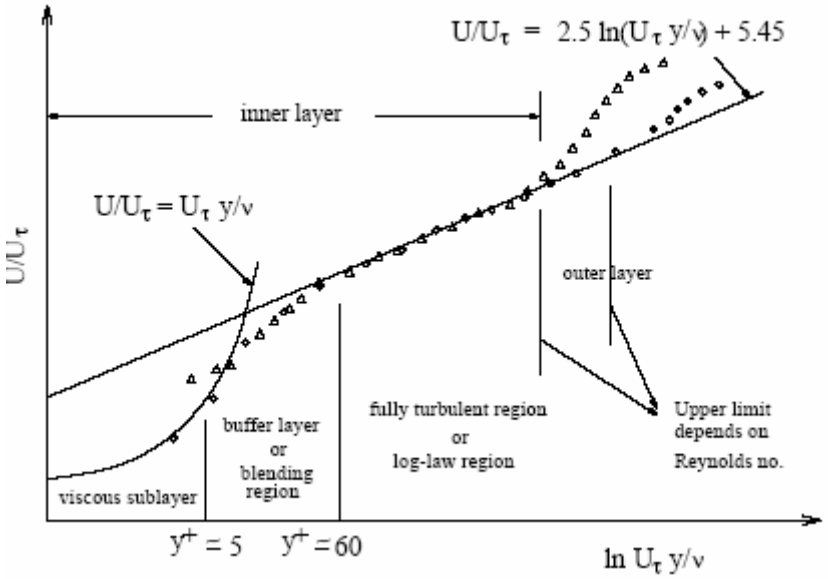

Figure 3.4: Schematic of near-wall regions for turbulent flow (reproduced from FLUENT, 2005).

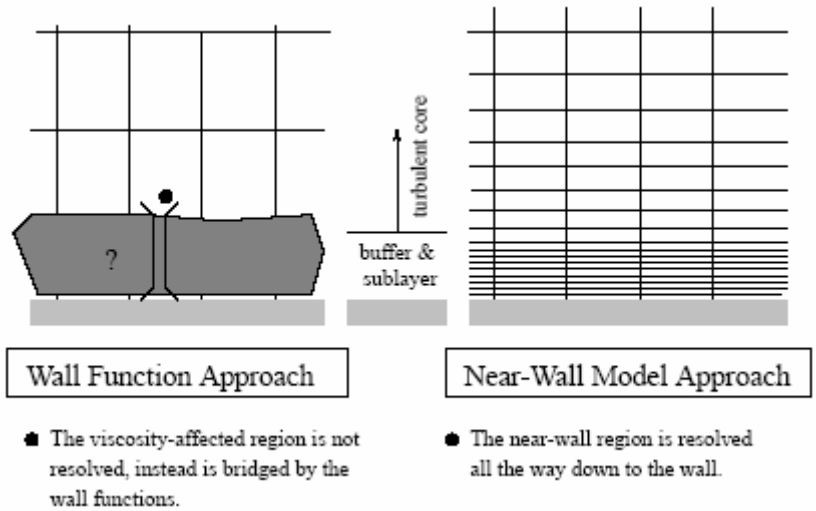

Figure 3.5: Wall function and near-wall model compared.

Standard Wall Function (SWF)

Two different wall functions are offered in FLUENT: SWF and non-equilibrium wall function. The SWF is the default function used in FLUENT while the equilibrium wall function is only recommended for separation and impingement flows and will therefore not be investigated. Using the SWF, the viscous-affected regions of a turbulent flow are split into two sublayers and modelled using laws-of-the-wall and near-wall formulae. Like the mean velocity laws, the laws-of-the-wall for the mean temperature are also split into two sublayers: thermal conduction sublayer and the turbulent region (FLUENT, 2005). These near-wall formulas are used to solve the production and dissipation of kinetic energy, for example.

When using the wall functions, an excessively fine grid near the wall can be detrimental in that the wall function will cease to be valid. A value of $y^+ \approx 30$ is therefore recommended in FLUENT (2005), where:

$$y^+ \equiv \frac{\rho u_\tau y}{\mu} \tag{3.20}$$

and

$$u_\tau \equiv \sqrt{\frac{\tau_w}{\rho}} \tag{3.21}$$

which is equivalent to a centroid location of y = 11.6 mm (where y is the distance from the edge of the left glazing as seen in Figure 3.1), using the approximation by White (2003):

$$\tau_w = \frac{\psi \rho V^2}{8} \tag{3.22}$$

where u_τ is the friction velocity the friction factor ψ is obtained from the Moody chart.

Near-Wall Treatments

Using the Reynolds-averaging method, the enhanced wall treatment (EWT) method uses a two-layer model in conjunction with enhanced wall functions to resolve near-wall gradients (FLUENT, 2005). The turbulent boundary layer is split between the viscous-affected region and the fully-turbulent region. The split between the two regions is demarcated in FLUENT by a turbulent Reynolds number:

$$\mathrm{Re}_y \equiv \frac{\rho y \sqrt{k}}{\mu} \tag{3.23}$$

where y is the distance from the nearest wall to the cell centroid location. The viscous-affected region is defined in FLUENT (2005) as $\mathrm{Re}_y < 200$ while the turbulent region begins at $\mathrm{Re}_y > 200$, equivalent to a distance of y = 4.5 mm away from the wall. The FLUENT (2005) literature recommends at least $y^+ < 5$ and ideally a value of $y^+ \approx 1$ be used in order to resolve the near-wall gradients. A value of $y^+ = 1$ corresponds to y = 0.39 mm. Furthermore, it is recommended that at least 10 cells be used within the viscous-affected region to effectively resolve the layer.

Model Selection: Having started with a large array of model and wall treatment options, the focus was narrowed to two different wall-treatments (SWF and EWT) and three different models (*standard* κ-ϵ, *standard* κ-ω and *SST* κ-ω). A fully developed *Nu* number analysis was undertaken to decide which wall treatment and which model would be best suited for modelling the upper portion of Configuration 1.

Fully Developed Nusselt Number Analysis

The first step towards developing a workable mesh for turbulent flow was to model the near-wall region based on a given near-wall treatment. In order to do that, the suggested guidelines from FLUENT (discussed above) were followed. Using SWT, the center of the first node was placed at $y^+ = 30$, corresponding to a distance of 11.62 mm from the wall. The remaining interior cells were spaced 2.53 mm apart, equivalent to 18 through the center of the cavity. For the EWT, the center of the first node was place at a distance of $y^+ = 0.97$, or y = 0.375 mm. Twenty cells of identical height (y = 0.375 mm) were used on both walls to resolve the near-wall region. Within the interior, twelve cells with height 5.19 mm were used. For both near-wall treatments, 40 cells were initially placed in the flow direction, corresponding to individual cell lengths of 250 mm. Both near-wall treatments were run for all three turbulence models, namely κ-ϵ, κ-ω and *SST* κ-ω. The fully developed *Nu* number was calculated based on the following equation by Lundberg et al. (1963):

$$Nu_i = \frac{Nu_{ii}}{1 - \left(\frac{q_0''}{q_i''}\right)\theta_i^*} \tag{3.24}$$

where Nu_i is the *Nu* number on the inner surface, q''_o and q''_i are the heat fluxes at the outer and inner surface, respectively, and θ^*_i is the *influence coefficient* on the inner side. The Nu_{ii} term represents the *Nu* number on the inner surface where only the inner surface is heated (Rohsenow et al., 1985). A similar equation can also be written for the outer surface, Nu_o and the two equations can be used to determine the fully developed *Nu* number for any combination of simultaneous heat fluxes to either surface (the designation of the inner or outer surface is arbitrary). In order to test the near-wall treatments, the

case of uniform heat fluxes on both surfaces was used ($q''_o = q''_i$). For this special case, the equation for Nu_i and Nu_o are the same. A uniform velocity of 0.8 m/s was used at the inlet (Re = 10,000). For this case, the *influence coefficient* is given as 0.220 (Rohsenow et al., 1985). The fully developed Nu number was therefore determined to be 35.64 from Eq. 3.24. The numerical results for all six cases are displayed in Table 3.2 below.

Table 3.2: Fully developed *Nu* number results.

Model	Nu_A	Nu_B
κ-ω *with EWT*	41.01	41.01
SST κ-ω *with EWT*	39.52	39.52
κ-ϵ *with EWT*	43.09	43.14
κ-ω *with SWF*	7.6	41.14
SST κ-ω *with SWF*	7.38	36.02
κ-ϵ *with SWF*	7.62	37.14

Having followed the recommended grid spacing provided by FLUENT (FLUENT, 2005), it was apparent that the WF method provides inaccurate information in the near-wall region, indicative by the low Nu numbers for Nu_A of Table 3.2. These inaccurate results are due to the relatively large distance between the wall and the cell centroid of the first cell (y = 11.62 mm). Using the WF, the temperature gradient $\frac{\partial T}{\partial x}$ is calculated using a linear slope (Figure 3.6) as opposed to the log variation as seen in Figure 3.4. Although the inaccurate results for Nu_A with SWF does not necessarily indicate erroneous results (as seen by the excellent results of Nu_B), it does indicate that there is no way of knowing how well the gradients are being resolved. It is due to this lack of information that the SWF could not be utilized. It was important at this early stage to know that all near-wall gradients are being resolved as further complexities, such as radiation, would be added to the model in the ensuing modelling stages. Comparing the three models which used EWT, the SST κ-ω model seemed to provide the most promise and as such it was decided

that the SST κ-ω model with EWT would be the model used for further model development.

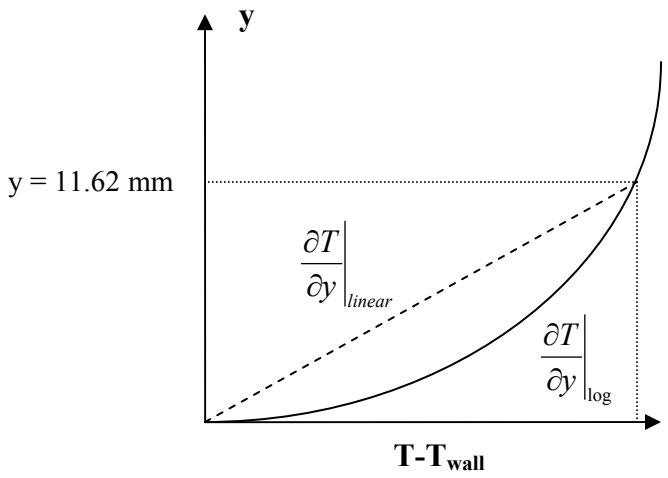

Figure 3.6: Schematic highlighting the WF method for calculating Nu_A near the wall.

SST κ-ω Model with EWT

Using the SST κ-ω model defined in the previous section, many refinements were made to the mesh to determine whether a more accurate fully developed *Nu* number could be obtained. The effects of increasing and decreasing the number of mesh nodes in both the near-wall region as well as the interior region were measured. In the end, a near-wall (NW) mesh with $n_{x,NW} = 20$ nodes spaced 0.775 mm apart was used with an interior mesh (IM) having $n_{x,IM} = 12$ nodes spaced 5.08 mm apart. The effects of increasing the grid density in the streamwise (SW) direction was also measured. It was found that a grid with 400 nodes in the y-direction did not provide any significant increase in accuracy compared to the original grid with $n_{y,SW} = 40$. Moreover, the extended convergence time made such a fine grid impractical. With this new mesh configuration, the fully developed *Nu* numbers were calculated to be: $Nu_A = 35.36$ and $Nu_B = 35.47$. As these values compared well with the published value of $Nu = 35.64$, it was decided that this mesh

would be used as the base model for a full scale grid sensitivity analysis. Henceforth, this model was referred to as the 'Base Case' model.

Grid Sensitivity Analysis – Turbulent Flow: Since it was known that the base model was capable of accurately measuring the fully developed *Nu* number for turbulent flow, the next step was to model the flow in the entrance region. In order to validate the model within this region, *Nu* numbers for developing flow was required.

Developing Nusselt Number Benchmarks

Within the literature, published data for developing flow between parallel plates (for air) was available at a *Re* number of 7104. Results from two different sources were used to validate the numerical results; both data sets were published in a paper by Hatton et al. (1964). The difference between the two sets of results resides in the ratio of eddy diffusivity of momentum to heat that was used. The first set of data, which is theoretical in nature, was obtained from work done by Azer and Choa (1960). Azer's *Nu* data is valid for *Pr* less than 15. For 0.6<Pr<15, the following simplified relation between the eddy diffusivity of momentum (γ_{mom}) and heat (γ_H) was used:

$$\frac{\gamma_H}{\gamma_{mom}} = \frac{1 + 135\,\mathrm{Re}^{-0.45}\exp\left[-\left(y/y_0\right)^{0.25}\right]}{1 + 57\,\mathrm{Re}^{-0.46}\,\mathrm{Pr}^{-0.58}\exp\left[-\left(y/y_0\right)^{0.25}\right]} \qquad \textbf{(3.25)}$$

The second set of results were from Hatton and Quarmby (1963); the ratio of eddy diffusivities for momentum and heat was assumed to be unity ($\gamma_H/\gamma_{mom}=1$). The eigen values and constants necessary to calculate the developing *Nu* numbers for the case of constant heat flux on one side and adiabatic conditions on the other are shown in Table 3.3:

Table 3.3: Eigen values for *Re* = 7104 (Hatton et al., 1964).

	γ_H/γ_m = equation (3.37)		γ_H/γ_m = 1	
	G_i 0.0376907		0.0448027	
Re = 7104	N	λ_n	C_n	λ_n	C_n
	1	8.8736	0.273419	7.7628	0.292106
	2	17.4189	0.101452	15.1606	0.119184
	3	25.1683	0.076028	21.9330	0.072589
	4	32.1251	0.064565	28.0676	0.072905

Using the given eigen values of Table 3.3, the developing *Nu* numbers for both cases were calculated using the following equation by Hatton and Quarmby (1963):

$$Nu = \frac{1}{G_i\left[1 - \sum_{n=1}^{\infty} C_n \exp\left(-8\lambda_n^2 y^+ / \mathrm{Re}\right)\right]} \qquad \textbf{(3.26)}$$

where y^+ is the dimensionless distance y/D_h where y is the distance from the entrance. A plot of both *Nu* values can be seen in Figure 3.7. The fully developed *Nu* numbers for the case of γ_H/γ_{mom} = Eq. 3.25 and γ_H/γ_{mom} = 1 are Nu_∞ = 26.50 and Nu_∞ = 22.30, respectively, which have been shown as solid lines in Figure 3.7.

Grid Sensitivity: Results and Discussion

Streamwise Mesh

As was previously mentioned, the Base Case for the SST κ-ω model, which was the starting point for the grid sensitivity analysis, was a mesh with 20 near-wall CV's on either side and 12 CV's across the interior; in the SW direction, 40 CV's were used. The local *Nu* values for the Base Case were plotted with the benchmarking data from Azer and Choa (1960) and Hatton and Quarmby (1963) (Figure 3.8). In order to quantify the grid sensitivity in the SW direction, the number of CV's in the y-direction was both doubled (Case 1) and halved (Case 2) while keeping the x-direction grid constant. The

results of all three cases can be seen in Figure 3.9. It can be seen that both Case 1 and Case 2 are in excellent agreement with the Base Case and that all three cases lie within the range of the published values. The one exception is the first node value of Case 2 which was 22% greater than the Base Case and outside of the benchmark data. The very beginning of the entrance region is therefore best resolved by the Base Case and Case 1. It can also be concluded that the *Nu* values along the wall are relatively insensitive to the mesh density in the streamwise direction. As there was little advantage to using the Case 1 mesh over the Base Case mesh, the y-direction mesh was kept at the Base Case value of $\Delta y = 0.25$ m for the present time.

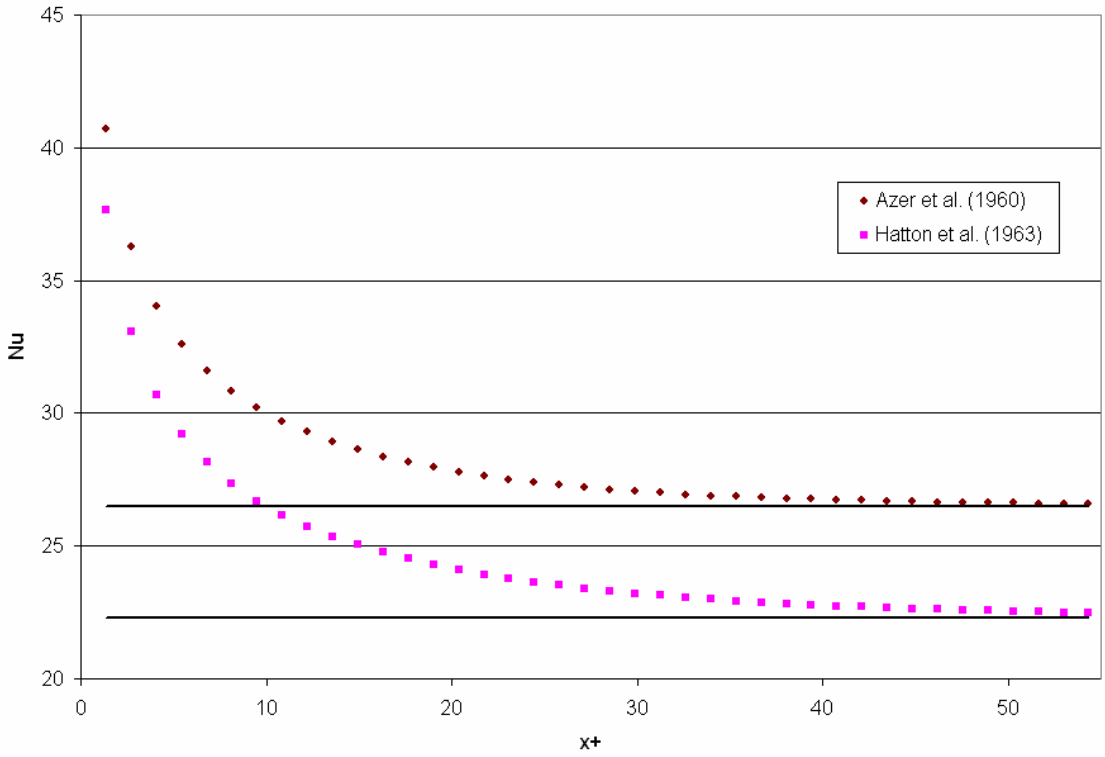

Figure 3.7: Benchmark data for developing *Nu* number along a wall with one wall at a constant heat flux and the other wall insulated.

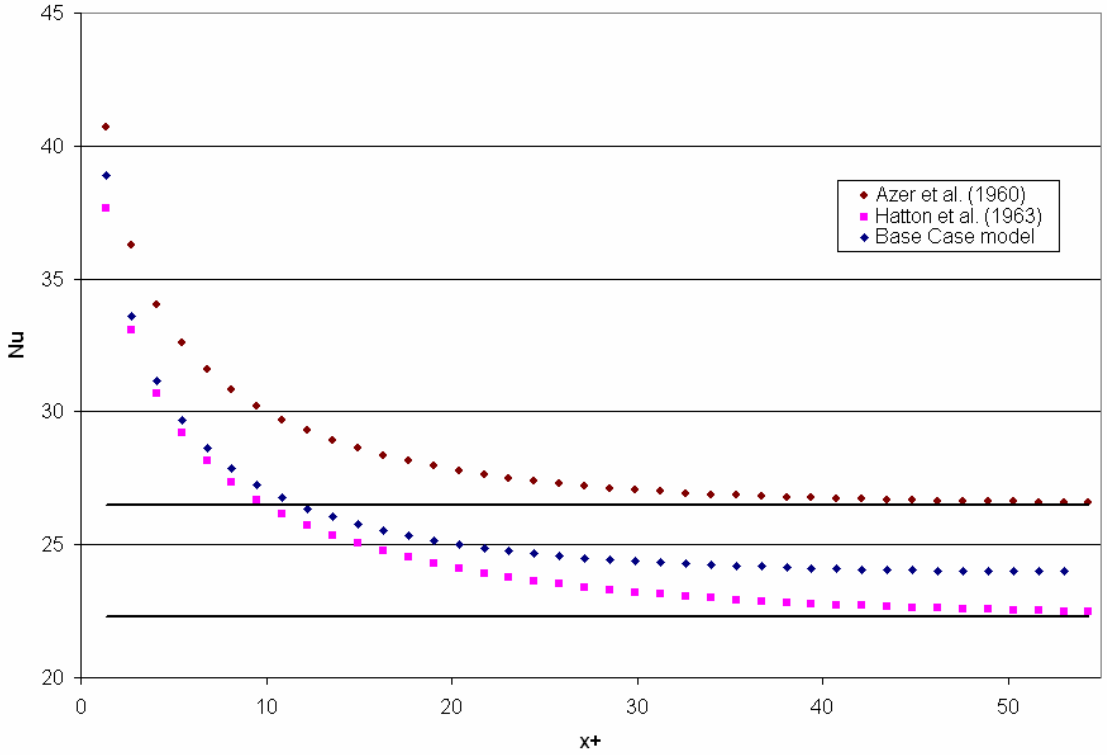

Figure 3.8: Base Case model compared to benchmarking data for developing *Nu* number.

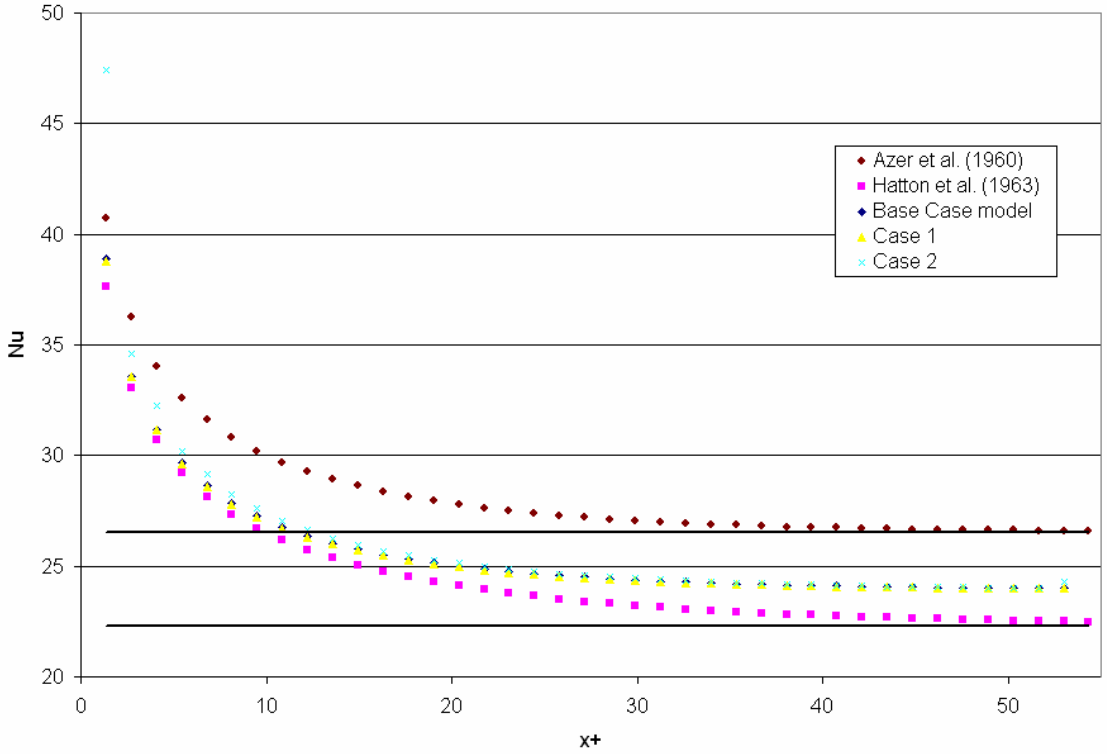

Figure 3.9: Comparison between Case 1 and Case 2 and the Base Case.

Cross-Stream Mesh

In order to test the models' sensitivity to the cross-stream mesh density, seven different cases were investigated. The properties of each mesh for the seven cases are shown in Table 3.4. Note that Cases 3 through 7 and the Base Case use a smaller mesh at the wall than in the interior. The mesh for Cases 8 and 9 was uniform mesh throughout the entire solution domain.

The results of the sensitivity study have been presented in Figure 3.10. Apart from Case 6, all of the data (beyond the first set of data points) lie between the two benchmarks. The first set of data points for both Case 3 and Case 5 were outside of the benchmarks; Case 5 was 16% greater than the data by Azer and Choa (1960). The trend in the data indicates that a higher mesh density results in a higher *Nu* number. Case 4, which has the lowest mesh density, follows the benchmark data by Hatton and Quarmby (1963) very closely. The data from Case 5, which has the second highest mesh density, follows the benchmark data from Azer and Choa (1960) very closely. The results from the Base Case as well as Case 3 and Case 7 are well positioned between both benchmarks.

Table 3.4: Summary of mesh configurations used for grid sensitivity analysis.

Case Identification	**# Nodes in boundary layer**	**# Nodes in center**	**# Nodes in y-direction**
Base Case (BC)	$n_{x,BC} = 20$	$n_{x,BC} = 12$	$n_{y,BC} = 40$
3	$n_x = n_{x,BC}*2$	$n_x = n_{x,BC}*2$	$n_{y,BC} = 40$
4	$n_x = n_{x,BC}/2$	$n_x = n_{x,BC}/2$	$n_{y,BC} = 40$
5	$n_x = n_{x,BC}*4$	$n_x = n_{x,BC}*4$	$n_{y,BC} = 40$
6	$n_x = n_{x,BC}*8$	$n_x = n_{x,BC}*8$	$n_{y,BC} = 40$
7	$n_x = n_{x,BC}*2$	$n_x = n_{x,BC}*1^{2/3}$	$n_{y,BC} = 40$
8	$n_x = 118$	NA	$n_{y,BC} = 160$
9	$n_x = 80$	NA	$n_{y,BC} = 160$

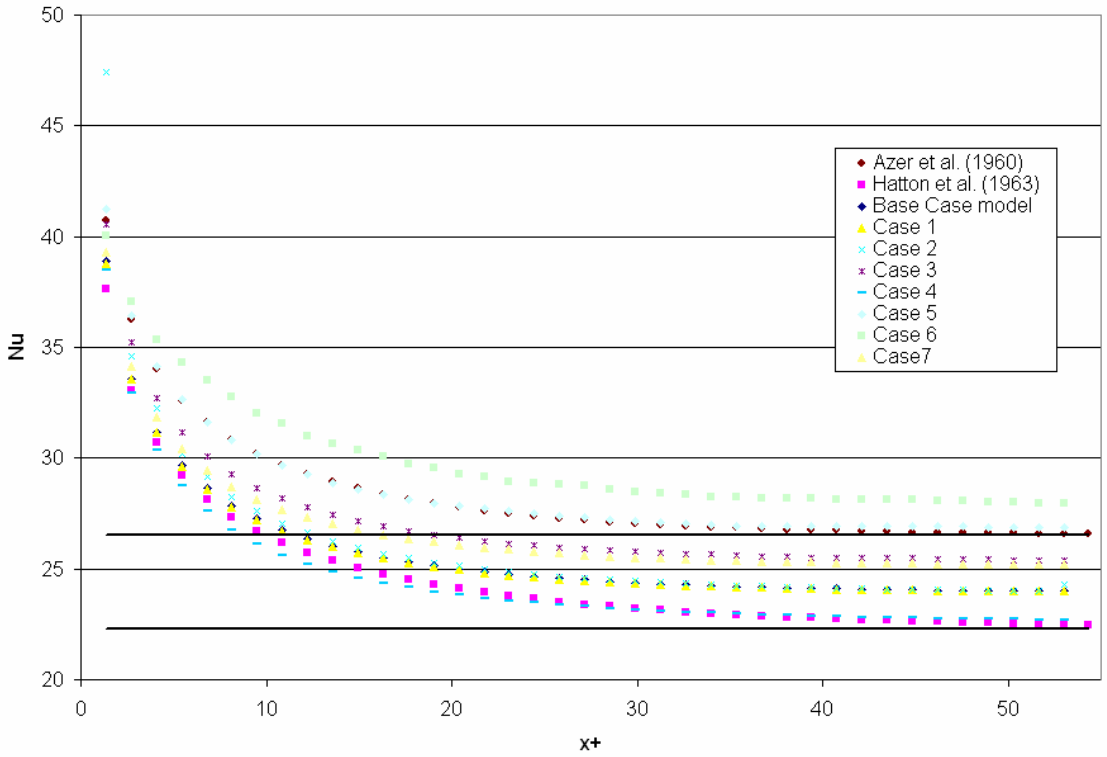

Figure 3.10: Results of sensitivity study for turbulent flow.

Two final grid sensitivity tests were performed to measure the effects of using a constant grid thickness in the cross-stream direction for the entire cavity width (Figure 3.11). The first such case, identified as Case 8, had the same mesh spacing across the cavity as was used in the near-wall treatment for the Base Case ($\Delta x \approx 0.78$ mm), resulting in $n_x = 118$. The second case, Case 9, used fewer cross-stream nodes with $n_x = 80$. Both meshes were tested with a tighter y-direction mesh of $\Delta y = 0.0625$ m or $n_y = 160$. The results were compared to the Base Case and the benchmark data and seen in Figure 3.11. It can be seen that the values for both Case 8 and 9 follow the Base Case values very closely with Case 8 displaying slightly higher *Nu* numbers compared to Case 9 due to the tighter grid. As both Case 8 and 9 converged relatively fast, it was decided that Case 8 provided the best possible grid for several reasons - not only was this grid able to accurately model turbulent flow within the developing and developed regions, the

large grid density and fast convergence bodes well for the next stage of modelling, Stage 2. In Stage 2, radiation heat transfer was added to the model as was a between-the-panes shading device; these additions to the model would best be accommodated with a uniform mesh, such as the Case 8 mesh.

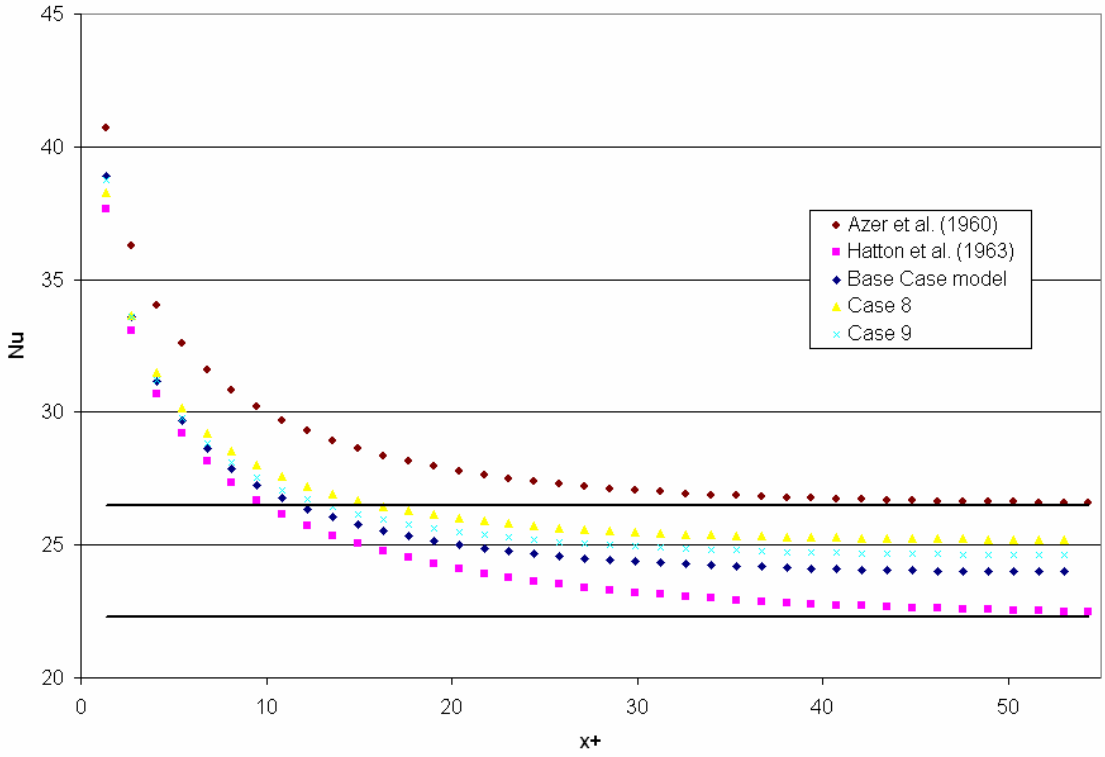

Figure 3.11: Comparison between Case 8 and Case 9 and the Base Case.

3.4 Stage 2: Radiation Validation

Having validated the mesh for forced convection between parallel plates, the focus was then placed on adding radiation heat transfer to the model. Using the validated mesh which was obtained from the sensitivity analysis described in the previous section, a series of validation exercises were run.

3.4.1 Introduction

In order to validate the mesh for radiative heat transfer, a two part analysis was required – an optical analysis and a heat transfer analysis. This type of approach is very

common for window software and is described in detail by Wright (1998). Because FLUENT does a poor job differentiating between long wave and short wave radiation, a separate short wave analysis was performed using VISION (UW, 1996) and the results were imported into FLUENT where the heat transfer calculations could then be performed; in this manner, a double-glazed window was modelled. As a window is a closed cavity, the convection is driven by buoyancy effects and not forced convection.

3.4.2 VISION

Algorithms capable of handling conduction, convection and long wave radiation heat transfer between multi-glazed windows with diathermanous layers and fill gases have been developed (UW, 1996). The VISION software is used to determine the U-factor for various window configurations. As such, only natural convection is present between glazing layers. By setting the indoor and outdoor conditions as well as the properties of each glazing layer, a short and long wave analysis is performed. For a given set of conditions, the energy absorbed at each layer can therefore be determined. The absorbed energy can then be used as a volumetric source term in FLUENT for the heat transfer analysis. The model algorithms in VISION are valid for one-dimensional center-of-glass heat transfer. For the purpose of validation, the temperature at each layer provided by VISION was compared to the temperature profiles generated by FLUENT. Although the FLUENT temperature profiles were two-dimensional and included end effects, a comparison between the center-of-glass temperatures obtained in VISION and surface-averaged temperatures obtained in FLUENT provided an excellent assessment of FLUENT's ability to model radiation heat transfer using the given mesh configuration (Case 8 of Table 3.4).

3.4.3 Modelling Radiation in FLUENT

Within FLUENT, five different models exist to solve radiation heat transfer. All of the equations solve the radiative transfer equation (RTE) (FLUENT, 2005):

$$\frac{dI\left(\vec{r},\vec{s}\right)}{ds}+\left(a+\sigma_s\right)I\left(\vec{r},\vec{s}\right)=an^2\frac{\sigma T^4}{\pi}+\frac{\sigma_s}{4\pi}\int_0^{4\pi}I\left(\vec{r},\vec{s}\right)\Phi\left(\vec{s}\cdot\vec{s}'\right)d\Omega \qquad \textbf{(3.27)}$$

where

$\vec{r}$ position vector,
$\vec{s}$ direction vector,
$\vec{s}'$ scattering direction vector,
l path length,
a absorption coefficient,
n refractive index,
σ_s scattering coefficient,
σ Stefan-Boltzmann constant (5.672 x 10^{-8} W/m^{2}K^4),
I radiation intensity (as a function of $\vec{r}$ and $\vec{s}$),
T local temperature,
Φ phase function,
Ω solid angle.

The transfer equation is related to the energy equation (Eq. 3.4) as follows:

$$S'''=q_r'''=\int_0^{\lambda}\iint_{4\pi}a_\lambda\left(I_{\lambda,b}-I\left(\vec{r},\vec{s}\right)\right)d\Omega\cdot d\lambda \qquad \textbf{(3.28)}$$

where b refers to a blackbody and λ refers to wavelength.

Each of the five radiation models have distinct strengths and are therefore best suited for specific applications. For problems involving semi-transparent walls, specular walls and non-gray radiation, only the Discrete Ordinates (DO) model can be used. Semi-transparent walls are required when modelling a diathermanous layer such as a between-the-panes roller blind. Although the modelling of specular and non-gray surfaces are beyond the scope of this project, the use of the DO model ensures that, if required, future complexities can be added to the model.

Discrete Ordinates Radiation Model: Using the DO model, the RTE can be solved for a specified number of solid angles. The RTE is essentially solved like any other transport equation, whereby the radiation intensity is transported from one solid boundary to another assuming the medium is non-participating (as is the case). The discretization of the DO model is discussed in the following section.

Angular Discretization and Pixelation

The DO model solves Eq. 3.27 for a specified number of discrete solid angles which is controlled by the user. As the model is two-dimensional, only four octants need to be resolved. Each octant is discretized into n_Θ x n_φ solid angles where Θ and φ are the polar and azimuthal angles in a Cartesian coordinate system, respectively (Figure 3.12). The default value of 3 x 3 was used for n_Θ x n_φ (FLUENT, 2005). In order to resolve any overhang issues (Figure 3.13), FLUENT further divides each solid angle into smaller pixels, $n_{\Theta P}$ x $n_{\varphi P}$ (Figure 3.14). The energy contained within each pixel is calculated as the sum of the incoming energy minus the sum of the outgoing energy. An increase in the pixilation will result in an increase in the computational resources. The effects of increasing the pixelation from its default value of 1 x 1 to 3 x 3 and 5 x 5 was measured and found to produce negligible differences as overhang is typically not a problem for well-structured meshes. A 3 x 3 pixel configuration was used to ensure the highest level of accuracy could be achieved with minimal effects on the computation time.

Boundary Conditions: In order to model the AFW with between-the-panes shading device, some assumptions were made. It was assumed that all reflections were purely diffuse, irregardless of the object from which the reflections were occurring. Furthermore, the radiation emanating from both the inside and outside environment was

considered to be from a blackbody. This is a valid assumption for any small surface in a large enclosure, irrespective of the absorptance and reflectance of the enclosure. Wavelength-independent properties were therefore assigned to each surface. Furthermore, the absorptivity of each surface was set equal to its emissivity by Kirchhoff's law. The amount of radiation emitted, reflected and absorbed at each surface was calculated in FLUENT (2005) as follows:

$$\textit{Emission (from wall)}: \ \varepsilon_w \sigma T_w^4 \tag{3.29}$$

$$\textit{Reflection (diffuse only)}: \ (1-\varepsilon_w) q_{in} \tag{3.30}$$

$$\textit{Absorption (at wall)}: \ \varepsilon_w q_{in} \tag{3.31}$$

where ε_w is the emissivity of the wall and q_{in} is the amount of radiant energy incident at any wall calculated as:

$$q_{in} = \int_{\vec{s}\cdot\vec{n}>0} I_{in} \vec{s} \cdot \vec{n} d\Omega \tag{3.32}$$

and the intensity I_{in} is obtained from the RTE (Eq. 3.27). The net radiation leaving a surface q_{out} and its intensity I_{out} is given by:

$$q_{out} = (1-\varepsilon_w) q_{in} + \varepsilon_w \sigma T_w^4 \tag{3.33}$$

$$I_{out} = \frac{q_{out}}{\pi} \tag{3.34}$$

As was previously mentioned, the amount of solar energy absorbed at each surface was determined from the VISION analysis.

Meshing: The dimensions of the glazings and the air cavity space used in the VISION analysis were different from the dimensions of the glazings and cavity width used in the Stage 1 validation. However, in order to ensure continuity between the convection

validation and the radiation validation, the mesh density obtained from the efforts of the Stage 1 validation was used for all radiation models in Stage 2.

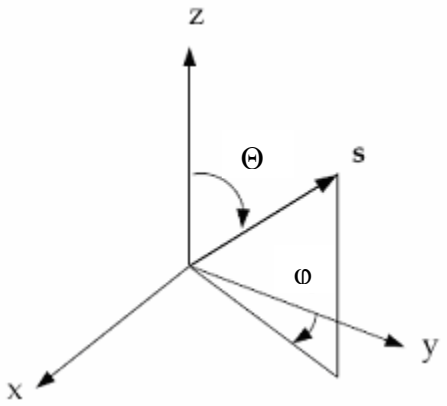

Figure 3.12: Angular coordinate system used in FLUENT.

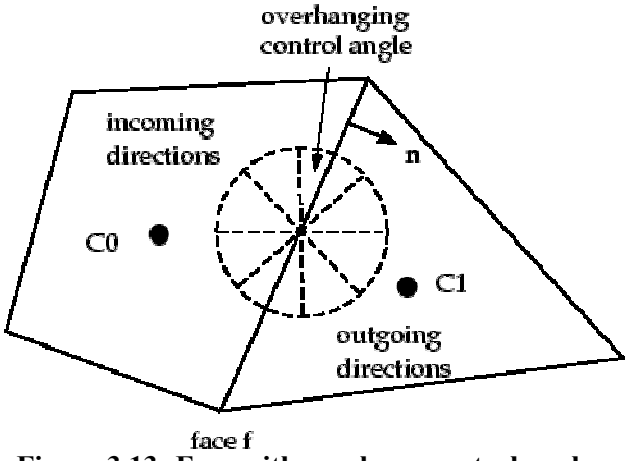

Figure 3.13: Face with overhang control angle.

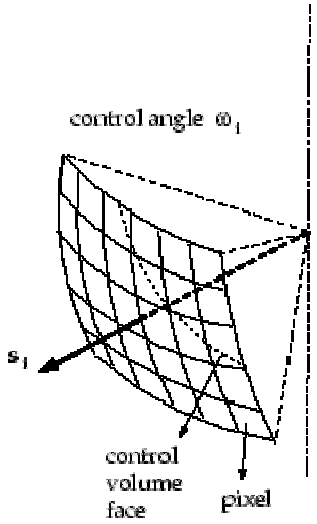

Figure 3.14: Pixelation of control angle.

Validation Data: In order to validate the numerical model, four different fenestration systems were modelled in VISION: single-glazing, double-glazing, triple-glazing and double-glazing with between-the-panes venetian blind. The temperature values generated at each surface in VISION were then compared to the temperature values obtained in FLUENT. A typical temperature profile obtained in FLUENT is relatively flat along the center-glass region with temperature variations near the ends where the tips were modelled as adiabatic surfaces.

Single Glazing

For the case of a single glazing, VISION was not required as an analytical analysis was sufficient. A 1 m tall glazing with a thickness of w = 30 mm and adiabatic tips was used for the validation; note that standard soda-lime thermal properties were used for all the validation exercises. A convective heat transfer coefficient of h = 0.5 W/m^{2}K and a surface emissivity of ε_w = 0.2 were assumed on both interfaces of the glazing. The ambient air temperature was set at T_∞ = 300 K and a volumetric source term of S''' = 1000 W/m^3 was used. The following analytical equation was used to calculate the wall temperature T_w:

$$S'''w + 2\varepsilon_w\sigma\left(T_\infty^4 - T_w^4\right) - 2h\left(T_w - T_\infty\right) = 0 \qquad \textbf{(3.35)}$$

From Eq. 3.35, the wall temperature was determined to be T_w = 308.44 K. Using the results from FLUENT, the average wall temperature on either side of the glazing was calculated as T_w = 308.46 K. The temperature values in FLUENT therefore compare extremely well to the analytical results for a single glazing.

Double-Glazed

Two parallel glazings, each 3 mm thick and 1 m tall, spaced 12.7 mm apart, were modelled in VISION. The emissivity of each side of the two glazings was set to ε_w = 0.84. With an input solar irradiance of G_s = 783 W/m^2 and a 100% cloud cover condition, the absorption (α) in the outer (A) and inner (B) glazing was determined by VISION to be $q_{\alpha A}$ = 73.3 W/m^2 and $q_{\alpha B}$ = 58 W/m^2, respectively. The outdoor temperature and heat transfer coefficient was 32°C and 16.77 W/m^{2}K, respectively, which is representative of summer conditions. The indoor temperature and heat transfer coefficient was 24°C and 3.04 W/m^{2}K, respectively. Using the boundary conditions from VISION as inputs to FLUENT and adding the appropriate volumetric source terms to each glazing, the temperature profiles at each interface of either glazing was generated. Using these temperature profiles, the average temperatures were then compared to the temperatures obtained in VISION. The following results were obtained (Table 3.5):

Table 3.5: Temperature comparison between VISION and FLUENT for a double-glazing.

		TEMPERATURE [K]	
Glazing	**Surfaces**	*VISION*	*FLUENT*
A	1	307.86	307.85
	2	307.93	307.93
B	3	305.96	305.93
	4	305.82	305.79

As can be seen, the values in FLUENT compare extremely well to those in VISION. Not only are the values accurate, the net change in temperature across any two surfaces was also very consistent. For example, both models show a temperature rise from Surface 1 to Surface 2 and a temperature drop from Surface 3 to Surface 4.

Triple-Glazed Façade

For the case of three glazings, the same dimensions and surface properties as the double-glazed case were used. An irradiance of G_s = 780 W/m^2 incident upon the façade with overcast conditions was assumed. From VISION, the solar energy absorbed by each of the three glazings, A, B and C, was determined to be $q_{\alpha A}$ = 76.1 W/m^2, $q_{\alpha B}$ = 61.7 W/m^2 and $q_{\alpha C}$ = 48.8 W/m^2, respectively. The inside and outside convective heat transfer coefficients were set at 3 W/m^{2}K and 20 W/m^{2}K, respectively. Winter conditions were assumed with indoor and outdoor temperatures of 21.1°C and -17.8°C, respectively. Using these quantities in FLUENT, the following temperature values were obtained at each surface (Table 3.6):

Table 3.6: Temperature comparison between VISION and FLUENT for a triple-glazing.

Glazing Identification		**Temperature [K]**	
Glazing	**Surfaces**	*VISION*	*FLUENT*
A	1	263.55	263.48
	2	264.05	263.99
B	3	284.75	284.90
	4	285.05	285.18
C	5	293.75	293.82
	6	293.85	293.91

Once again, the temperatures obtained from FLUENT compared very well to those obtained in VISION. Moreover, the temperature drops across each surface predicted by FLUENT were also very close to those produced in VISION. The results obtained in FLUENT for one, two and three glazing window systems with conduction, (natural) convection and radiation appear to be in excellent agreement with VISION indicating that the mesh obtained from the convection validation holds for radiation heat transfer as well. The final step to the radiation validation (Stage 2) was to analyze the results for a double-glazed system with a between-the-panes shading device.

Double-Glazed Façade with Between-the-Panes Shading Device

A window with three surfaces, comprising two glazings and an internal shading device, was modelled in FLUENT. The glazings had the same dimensions and surface properties as the double-glazed case. The interior surface (blind) was modelled as a diathermanous layer - a surface that transmits long wave radiation due to its openness. In VISION, a 3 mm thick Teflon layer with long wave transmissivity, emissivity and reflectivity of 0.15, 0.10 and 0.75, respectively, was employed. The Teflon had a short wave transmissivity of 0.76, an index of refraction of 1.34 and a conductivity of 0.9 W/mK. The same environmental conditions that were used for the triple-glazed system were used for this case. The solar energy absorbed by each of the three layers, A, B and C, was therefore $q_{\alpha A}$ = 76.1 W/m^2, $q_{\alpha B}$ = 61.7 W/m^2 and $q_{\alpha C}$ = 48.8 W/m^2, respectively. The following temperature values were obtained from FLUENT (Table 3.7):

Table 3.7: Temperature comparison between VISION and FLUENT with between-the-panes shading device.

Glazing Identification		**Temperature [K]**	
Glazing	**Surfaces**	*VISION*	*FLUENT*
A	1	266.35	266.69
	2	266.75	267.46
B	3	299.93	299.95
	4	300.23	300.00
C	5	301.75	300.23
	6	301.75	300.16

As was the case for the three previous validation scenarios, FLUENT was able to accurately calculate the surface temperature for all three surfaces. As such, it was concluded that the given mesh density can be used with utmost confidence to predict radiation heat transfer between parallel surfaces with conduction and convection. All that remained at this point was to validate the model for forced convection with between-the-

panes shading device including the effects of radiation. This portion of the validation required data from the Solar Lab at Concordia University.

3.5 Stage 3: Combined Convection-Radiation Validation

Having effectively validated the numerical model for forced convection (with both laminar and turbulent flow) as well as radiation (with natural convection), only the third and final validation stage remained. The final mesh validation step (Stage 3) was to validate the model for forced convection with radiation with a between-the-panes shading device. This was achieved using experimental data obtained from the Solar Lab at Concordia University.

3.5.1 Introduction

At Concordia University, there exists a Solar Lab which houses both Configuration 1 and Configuration 2 (Figure 1.2). A full scale acquisition system is used to gather experimental data. The acquisition system includes a host of sensors used to measure environmental conditions as well as particle image velocimetry (PIV) to measure the flow dynamics.

3.5.2 Experimental Instrumentation

In order to measure the outside conditions, a LICOR weather station, model LI-1401 Agro-Meteorological Station, was used (Liao, 2005). The LICOR weather station, in conjunction with an Agilent data logger (Liao, 2005), stores information such as solar irradiation, air temperature, wind speed and direction, relative humidity, etc. A damper controller, model LM24-SR-2.0 US from the Belimo Company (Liao, 2005), is used to

control the flow of air into the BIPV/T system. The air is propelled by a variable speed fan, model M1105SB from the AC Technology Corporation (Liao, 2005). Information within the BIPV/T cavity is acquired through two pressure sensors, a host of T-type thermocouples and by the method of PIV.

PIV: Due to the relatively small width of the cavity, obtaining flow dynamic measurements within the BIPV/T system is challenging. Traditional methods, such as hot wire anemometry, introduce probes into the flow which alter the fluid dynamics and may result in false readings both upstream and downstream of the instrumentation. Other techniques, like laser Doppler anemometry are time consuming as they are single-point measurements. PIV is non-obtrusive as no instrumentation is inserted into the flow. Moreover, PIV is a whole-field method which means it is not as time consuming as other techniques.

PIV is based on the direct measurement of two fundamental dimensions of velocity: length and time (Johnson, 2005). If the distance traveled by a particle in the flow is known as is the time required to travel such a distance, a velocity vector for that particle can be generated. By performing this measurement on an entire field of particles within the flow, a set of velocity vectors, representative of the entire flow can thus be obtained. The distance traveled by each particle is measured using two lasers in tandem that are directed into the flow (Figure 3.15). The lasers are set to pulse at different times and a high speed camera is used to capture an image for each pulse of light; the laser, which illuminates the flow, thus creates a light-sheet. The camera uses the light-sheet in order to capture the images of the particles. The particles which are exposed by the light sheet and captured by the high speed camera are called tracer particles. These tracer

particles, which are injected into the flow, must be representative of the flow field. Tracer particles which are either too heavy or too light will not follow the fluid motion and will thus not adequately represent the flow. Due to the high resolution required, a specialized charge-coupled device (CCD) is used to convert light from the photons into an electric charge (electrons) (Johnson, 2005). During the exposure, the electrons that accumulate are stored into cells which are divided into pixels. The data from the pixels that are stored on the CCD are used as interrogation windows where a statistical process known as cross-correlation is performed. In this process, all noise is filtered out (mathematically) and the path of the particle is determined by calculating the probability of the said particle to travel from its original position (captured by the first image) to any other nearby position (captured by the second image). The path which has the highest probability of occurrence (Figure 3.16) is said to be its path of travel and a velocity vector is thus generated. An example of a set of velocity vectors was shown in Figure 2.14. An example of actual PIV images captures by the two lasers in succession is shown in Figure 3.17a and 3.17b.

The PIV setup at Concordia University can be seen in Figure 3.18. Due to a lack of space, the laser and camera were mounted parallel to each other and a mirror was used to ensure that the light sheet and camera image were perpendicular to one-another. Smoke particles, which acted as the tracer particles, were injected into the flow near the inlet damper. Sixty pairs of images were captured for each PIV data set. The sixty images were statistically averaged and a representative velocity field was created. Each image spanned an area that was approximately 100 mm x 100 mm. Thermal information within the cavity was obtained using T-type thermocouples equipped with radiation shields. The thermocouples were mounted at thirteen locations within the cavity and the

data was stored by a Agilent 34970A data logger (Liao, 2005). In this manner, both fluid dynamic and thermal dynamic information was obtained for the upper section of Configuration 1.

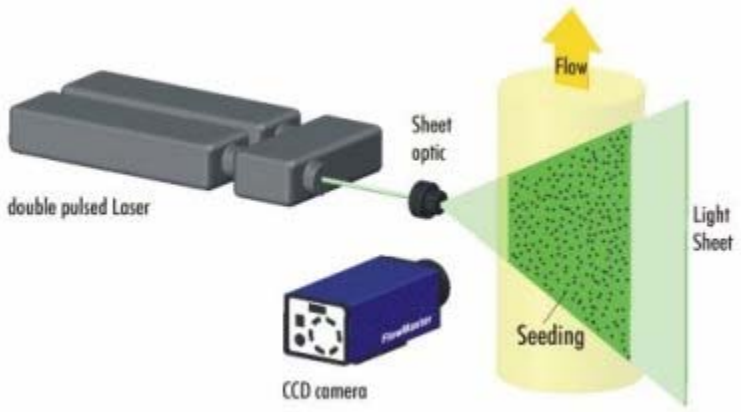

Figure 3.15: Components of a PIV experiment (reproduced from LaVision).

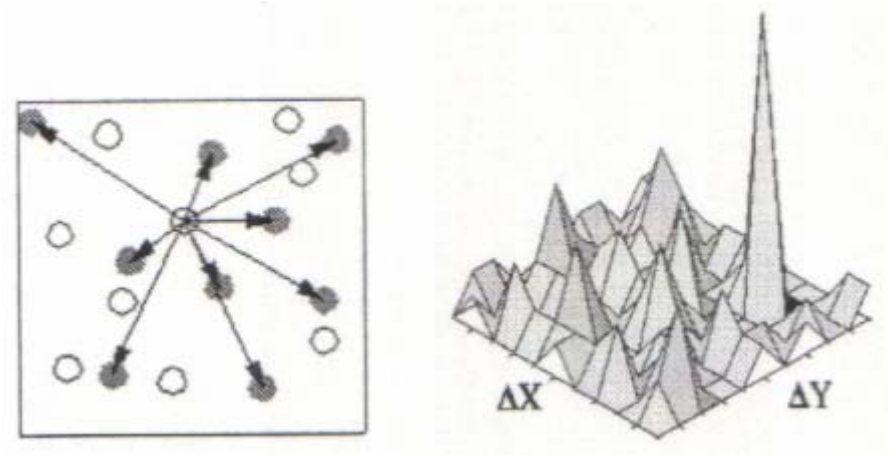

Figure 3.16: Spatial correlation for PIV (reproduced from Johnson, 2005).

3.5.2 Model Boundary Conditions

Experimental data from two different days was used to complete Stage 3 of the validation. The first set of data, obtained May 3rd 2005, was used to validate the velocity profile generated in FLUENT while the second set of data, collected March 13th 2006, was used to measure FLUENT's thermodynamic capabilities. For the sake of simplicity, data collected May 3rd will herein be referred to as data set A while data set B will refer

to the data collected on March 13th. As data was collected on two distinct days, two different sets of boundary conditions exist.

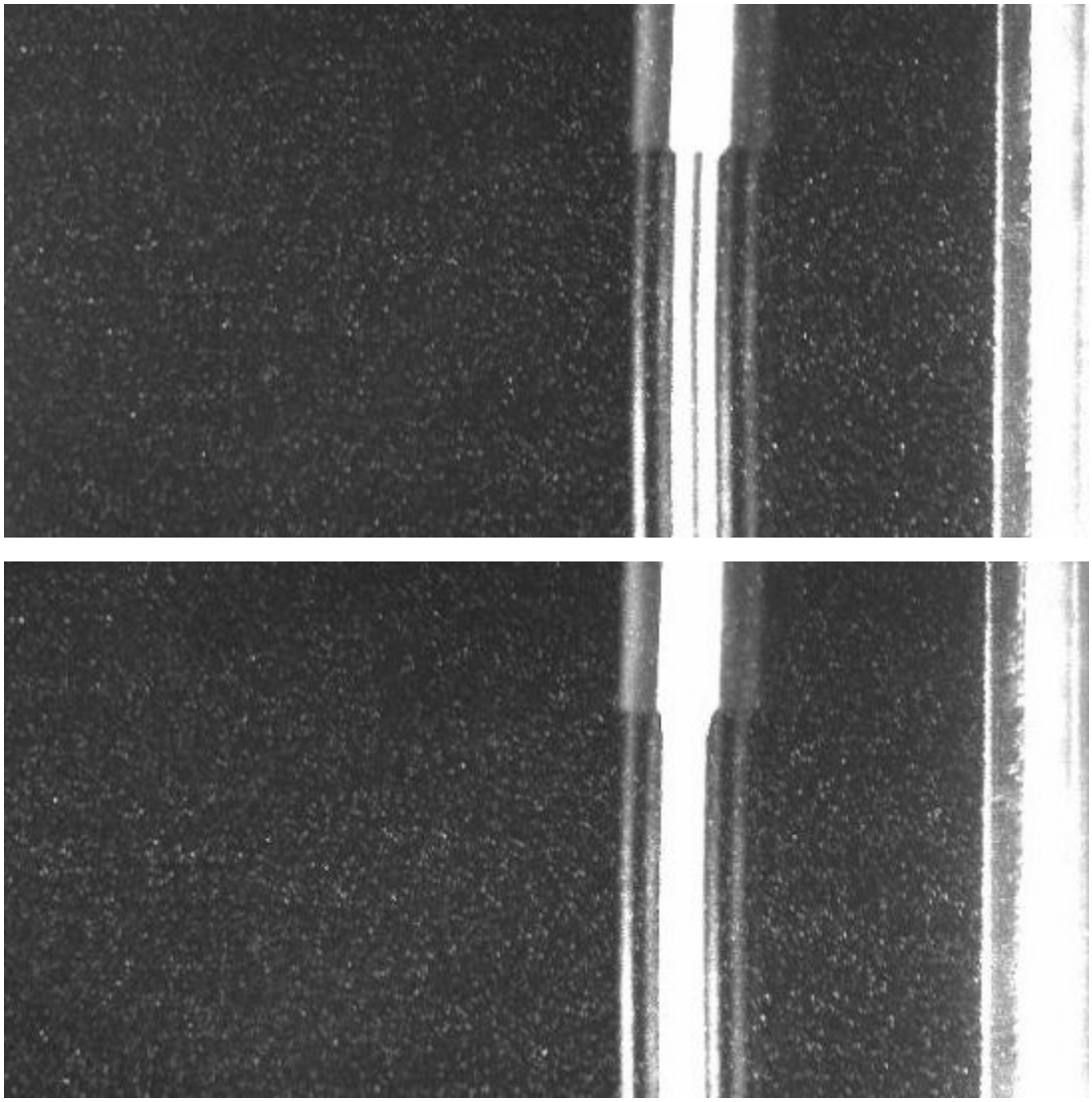

Figure 3.17: A set of PIV images captures at Concordia University (top – 3.17a and bottom – 3.17b).

Data Set A: The sample of the data collected on May 3rd at 10:49 am, which was used to validate the velocity profile inside the AFW, can be seen in Appendix B. The solar irradiance, outdoor ambient temperature and wind speed at the time the data was collected were 774 W/m^2, 8.3°C, and 3.6 m/s, respectively. As always, the walls were modelled as smooth surfaces with a no-slip boundary condition. The velocity profile at the entrance of the upper section was obtained from measurements of the velocity profile

at the outlet of the lower section. The outlet of the AFW was simply modelled as a zero pressure outflow region.

Figure 3.18: PIV setup including camera, mirror and laser (reproduced from Liao, 2005).

Data Set B: The data collected on March 13th at 1:31 p.m. was used to validate the temperature profiles inside the AFW section. Although the majority of the relevant environmental data was collected during experimentation, certain values had to be approximated using the existing data as well as some assumptions. The following table (Table 3.8) is a summary of the experimental data that was collected on March 13th as well as the data that had to be approximated. In addition to the data presented in Table 3.8, thirteen temperature values were collected. The relative location of the data points have been shown in Figure 3.19; the corresponding temperature data is shown in Table 3.9.

The outdoor wind speed data collected on March 13th was used to calculate the outdoor heat transfer coefficient (Table 3.8) using the following correlation by Beckman and Duffie (1991):

$$\bar{h}_{conv,out} = \max\left[5, \frac{8.6W^{0.6}}{Z^{0.4}}\right] \quad \textbf{(3.36)}$$

where Z is calculated as the cube root of the building volume in meters and W is the wind speed in m/s. The wind speed was measured as 1.16 m/s and Z was previously calculated as 2.97 m, resulting in an outdoor convective coefficient of $\bar{h}_{conv,out}$ = 6.1 W/m^{2}K, where *conv* is the abbreviation for convection.

Table 3.8: Experimental data collected on March 13th at 1:31 p.m.

Model Inputs	*Value*	*Explanation*
Outdoor Boundary Conditions		
Solar irradiance (G_s)	39.9 W/m^2	Solar irradiance incident upon Solar Lab
Heat transfer Coefficient ($h_{c,out}$)	6.1 W/m^{2}K	Convective coefficient calculated using Eq. 3.35
Free stream temperature ($T_{ext,\ out}$)	4.4°C	Temperature of outside air
External emissivity ($\epsilon_{ext,\ out}$)	1	Emissivity of surroundings (assumed)
Indoor Boundary Conditions		
Heat transfer Coefficient	2 W/m^{2}K	Convective coefficient calculated using Eq. 3.36
Free stream temperature ($T_{ext,\ in}$)	24.7°C	Temperature of air inside Solar Lab
External emissivity ($\epsilon_{ext,\ in}$)	1	Emissivity of surroundings (assumed)

The average inside heat transfer coefficient was estimated using a correlation by Fohanno and Polidori (2006):

$$\bar{h}_{conv,in} = 1.174 \exp(0.0355H) \cdot \left[q''_W\right]^{0.24} \quad \textbf{(3.37)}$$

where H is the height of the wall and q''_W is the heat flux through the wall. This correlation is commonly used in building applications (Fohanno and Polidori, 2006) and is valid for walls up to 3 m in height. The height of the wall inside the Solar Lab is known to be 2.9 m. The heat flux through the wall had to be approximated using a thermal resistance network for one-dimensional heat transfer:

$$q''_W = \frac{\Delta\bar{T}}{R''_{tot}} \quad \textbf{(3.38)}$$

where the $\Delta\overline{T}$ is the temperature difference between the inside and outside air. The total resistance R''_{tot} was calculated as:

$$R''_{tot} = \frac{1}{h_{in}} + \frac{1}{h_{out}} + R''_{wall} \tag{3.39}$$

where R''_{wall} was known to be approximately 4.5 m^2K/W (Athienitis, 2006). Because R''_{wall} was an order of magnitude greater than the other two resistances, both the inside and outside resistances could be neglected. Having calculated the heat flux through the wall, Eq. 3.36 was used to calculate the indoor convective heat transfer coefficient. As can be seen from Table 3.8, a value of 2 W/m^2K was used. From this information, the inside wall temperatures of the Solar Lab on March 13th were approximated to be 1°C below the ambient air temperature, or 23.7°C.

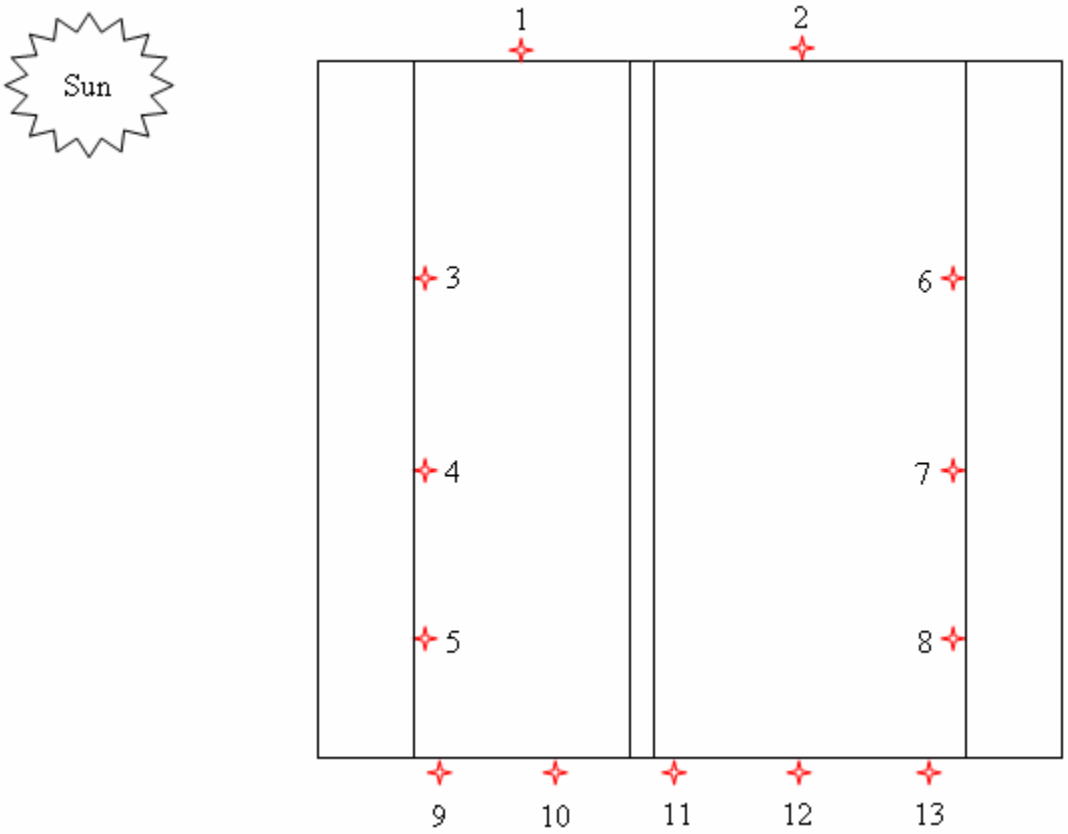

Figure 3.19: Schematic of T-type thermocouple positions within AFW.

Table 3.9: Temperature values obtained on March 13th (Figure 3.19).

Location	*Temp. [°C]*
1	5.6
2	8.6
3	5
4	4.9
5	4.8
6	9.9
7	9.9
8	8.4
9	5.2
10	5.3
11	5.5
12	5.7
13	5.4

Solar Optical Properties

When modelling glazing systems with incident solar radiation, both beam and diffuse components must be considered. The transmissivity (τ), absorptivity (α) and reflectivity (ρ) of any glazing layer are functions of incidence angle and wavelength. In general, if one were to average the optical properties for each surface, an integral would be performed over all wavelengths and over all solid angles and the sum of these three values would sum to unity (i.e. $\tau + \alpha + \rho = 1$). When using VISION, averaged optical values are required in order to calculate the solar gain through the glazing system. The determination of the solar optical properties for any glazing also depends on the nature of insolation; insolation can be characterized as either beam, diffuse, or both. In a typical glazing system, incident beam radiation is reflected and transmitted specularly while incident diffuse radiation is reflected and transmitted diffusely at each interface. For this type of analysis, software such as VISION provides trustworthy results. However, when a shading layer (such as a roller blind) is incorporated into a glazing system, incoming beam radiation can be scattered, leading to diffuse radiation (Wright and Kotey, 2006).

For this type of analysis, VISION does not have the tools to effectively model such glazing/shading layers. Nonetheless, recent research was conducted by Wright and Kotey (2006) which developed new solar optical algorithms for modelling glazing systems with shading devices. The results of such a model does provide the absorbed solar radiation in each layer as well as the transmitted and reflected fluxes. For cases where both beam and diffuse irradiation is present, the model by Wright and Kotey (2006) is required for the optical analysis. Having measured the solar irradiance on March 13th at 1:31 p.m., which was used to represent the average solar irradiance between 1-2 p.m. for that day, a calculation was performed to determine the ratio of diffuse-to-beam radiation. It was determined (Appendix C) that only 0.5% of the total radiation measured by the spectrophotometer at that time was due to beam radiation. As such, all of the incoming irradiation was therefore treated as purely diffuse and VISION could therefore be used to perform the optical analysis. According to Brandemuehle and Beckman (1980), the optical properties of glazings under purely diffuse radiation is tantamount to calculating the optical properties for beam radiation incident at 58°. The formulas used to calculate the optical properties of the glazing layers are shown in the following section. The solar optical properties of the shading layer, on the other hand, had to be determined by direct measurement. Note that the optical properties in the visible range for either the glazings or shading device were not calculated as daylighting issues was not considered in this thesis.

Clear Glass: The calculation of the optical properties for clear glass was performed assuming beam radiation at an incidence angle of 60°; for clear glass, the following equations were used to calculate the optical properties:

$$\tau_a = e^{\frac{-Kz}{\cos(\theta_L)}} \tag{3.40}$$

$$\tau_s = \frac{\tau_a(1-r_s)}{1-r_s^2\tau_a^2} \tag{3.41}$$

$$r_s = \frac{n-1}{n+1} \tag{3.42}$$

$$\rho = r_s(1+\tau_a\tau_s) \tag{3.43}$$

where

τ_a transmissivity, which is the amount of light which directly passes through the medium (Figure 3.20),
τ transmittance of the medium which includes direct transmissivity as well as additional transmission due to internal reflections (Figure 3.20),
K extinction coefficient,
Z thickness of the medium,
r_s reflectivity of the medium (Figure 3.20),
ρ reflectance, which includes the reflectivity as well as additional reflection due to internal reflections (Figure 3.20),
θ_L angle of incidence (Figure 3.20).

From previous measurements, it was determined that transmittance of the clear glass at normal incidence was $\tau_{s,N} = 0.8$ where N refers to normal incidence. Using Eq. 3.40, the extinction coefficient for the glass was calculated by setting τ_a to 0.8, L to 0.021 m and the incidence angle to zero ($\theta_L = 0$). The transmissivity of the clear glass for an incidence angle of 60° could then be calculated using Eq. 3.41 where τ_a was recalculated using Eq. 3.40 for an incidence angle of 60°. Having obtained this transmissivity, the transmittance at 60° was then calculated using Eq. 3.41. The reflectivity of the glass r_s at normal incidence was calculated using Eq. 3.42 assuming an index of refraction for glass of n = 1.52. Knowing the normal reflectivity, the normal reflectance of the clear glass was then calculated using Eq. 3.43. In order to calculate the reflectance of at 60°, the following three equations were required:

$$\sin\theta_L = n\sin\theta_{tr} \tag{3.44}$$

$$r_A = \left[\frac{\sin(\theta_L - \theta_{tr})}{\sin(\theta_L + \theta_{tr})}\right] \tag{3.45}$$

$$r_B = \left[\frac{\tan(\theta_L - \theta_{tr})}{\tan(\theta_L + \theta_{tr})}\right] \tag{3.46}$$

where *L* and *tr* are the incident and transmitted components and A and B represent the perpendicular and parallel polarized components of the reflectivity. Since it was assumed that the radiation was non-polarized, the average reflectivity was calculated as:

$$r = \frac{r_A + r_B}{2} \tag{3.47}$$

Having calculated the average reflectivity at 60° using Eqs. 3.44 and 3.47, the reflectance was then calculated using Eq. 3.43.

Low-E Glass: Having calculated the solar optical properties for clear glass, the following equations were used to calculate the solar optical properties for the low-E glass:

$$\tau_{60}(LE) = \left[\frac{\tau_{60}(CG)}{\tau_N(CG)}\right]\cdot\tau_N(LE) \tag{3.48}$$

$$\rho_{60}(LE) = 1 - \left[\frac{(1-\rho_{60}(CG))}{(1-\rho_N(CG))}\right]\cdot(1-\rho_N(LE)) \tag{3.49}$$

where *LE, CG* and *N* are abbreviations for low-E, Clear Glass and Normal incidence, respectively. The optical properties of both the clear glass and the low-E are shown in Table 3.10.

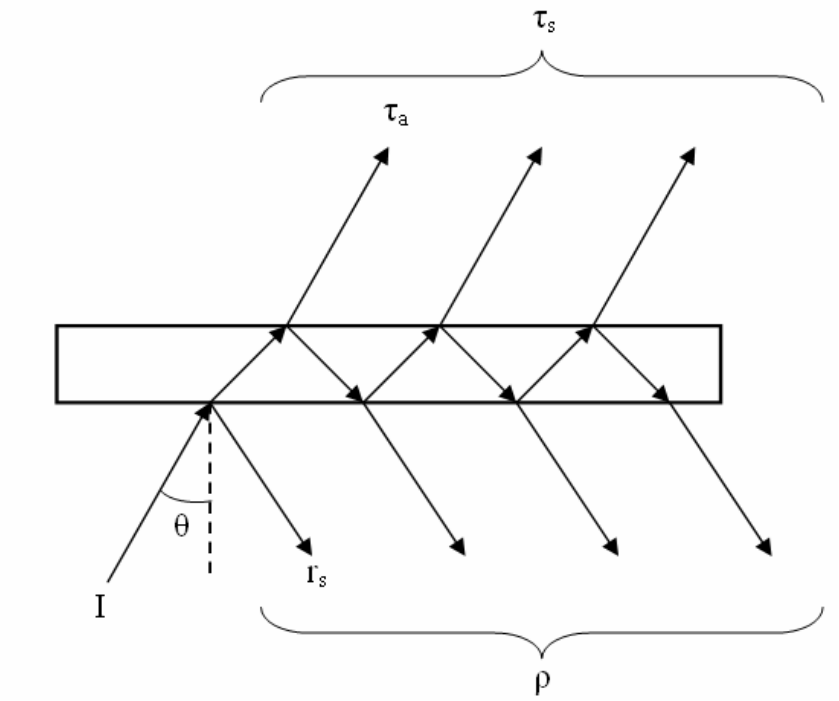

Figure 3.20: Example of internal reflections within a glass medium.

Table 3.10: Optical properties of glazings for upper section of Configuration 1.

	τ (normal)	ρ (normal)	τ (60°)	ρ (60°)
Clear Glass	0.80	0.07	0.72	0.13
Low-E Glass	0.70	0.12	0.63	0.18

Shading Layer: The solar optical properties of the shading device were determined by direct measurement using a CARY 5000 spectrophotometer. The spectral data obtained from the spectrophotometer was averaged over the entire solar spectrum and determined to be as follows:

Table 3.11: Optical properties of roller blind.

	τ	ρ	α
Roller Blind	0.10	0.60	0.30

Long Wave Properties

Due to the long wave transmittance of the blind, a special measuring procedure (Christie and Hunter, 1984) was required for the measurement of the transmittance and reflectance.

Using the Gier-Dunkle DB-100 Infrared Spectrometer, the blind sample was placed at the port of the spectrometer while two different specimens (back reflecting surfaces), one at a time, were placed behind the blind. According to Christie, an air gap must exist between the sample and the back reflecting surfaces. Reflectance measurements were made for each case and the results were used in Eqs. 3.50 and 3.53:

$$\rho_{\lambda M1} = \rho_{\lambda} + \frac{\tau_{\lambda}^2 \rho_{\lambda B1}}{1 - \rho_{\lambda B1}\rho_{\lambda}} \tag{3.50}$$

$$\rho_{\lambda M2} = \rho_{\lambda} + \frac{\tau_{\lambda}^2 \rho_{\lambda B2}}{1 - \rho_{\lambda B2}\rho_{\lambda}} \tag{3.51}$$

$$\rho_{\lambda} = \frac{\left(\rho_{\lambda B1} / \rho_{\lambda B2}\right)\rho_{\lambda M2} - \rho_{\lambda M1}}{\left(\rho_{\lambda B1} / \rho_{\lambda B2}\right) + \rho_{\lambda B1}\left(\rho_{\lambda M2} - \rho_{\lambda M1}\right) - 1} \tag{3.52}$$

$$\tau_{\lambda} = \sqrt{\frac{\left(\rho_{\lambda M1} - \rho_{\lambda}\right)\left(1 - \rho_{\lambda}\rho_{\lambda B1}\right)}{\rho_{\lambda B1}}} \tag{3.53}$$

where $\rho_{\lambda M1}$ is the reflectance of the blind and first back reflecting sample as measured by the DB-100. The reflectance of the blind and the second back reflecting sample is $\rho_{\lambda M1}$ while $\rho_{\lambda B1}$ and $\rho_{\lambda B2}$ are the reflectances of the first and second back (B) reflecting surfaces, respectively (Figure 3.21).

The long wave properties of the clear glass and the low-E were obtained from the manufacturer. The long wave properties are presented below in Table 3.12.

Table 3.12: Long wave properties of all materials.

	τ	ρ	α
Clear Glass	0.0	0.16	0.84
Low-e Glass	0.0	0.90	0.10
Roller Blind	0.11	0.22	0.67

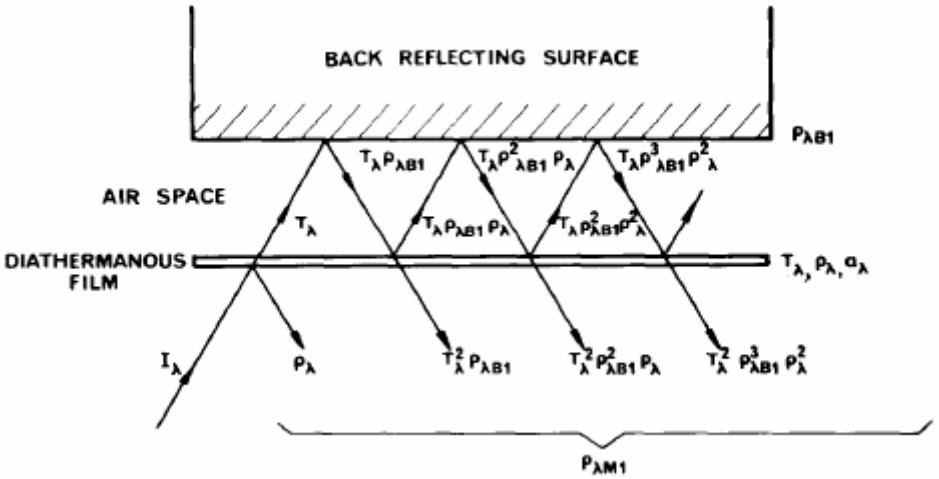

Figure 3.21: Reflectance measurements of a diathermanous layer (reproduced from Christie and Hunter, 1984).

3.5.3 Results and Discussion

Data set A: The velocity profile obtained from FLUENT was compared to that obtained from the experimental data. It should be noted that, during the experiments, certain difficulties arose. Due to the forced convection air currents, the blind was observed to be moving from side to side. Furthermore, due to the weight of the stopper attached to the bottom of the blind, the blind did not hang perfectly vertical. This observation, as will be seen, was reinforced by the results which showed that the angle of the blind with respect to vertical, although slight, did affect the flow pattern. Additional problems were encountered when dealing with the high-speed camera. Although the camera was positioned to be exactly in line with the blind so that only the true thickness of the blind was visible during the image capturing process, a perfect alignment was unobtainable; due to wear and tear and overall aging of the blind, the blind was curved and small undulations could be observed, causing a false thickness to be captured by the camera. As a result of all of these factors, the thickness of the blind, as captured by the high-speed camera, was close to 7 mm, or approximately 10 times the actual thickness.

When the experimental data was first compared to the numerical results, one of the first discernable discrepancies between the two was the difference in peak velocities. The velocity profile generated by FLUENT would indicate that an equivalent maximum velocity on either side of the blind could be expected. From the experimental data, it was observed that the velocity on the left side of the blind had a larger peak velocity than the right side. These findings indicated that the air on the left side of the blind was accelerating while the air on the right side of the blind was decelerating, indicative of a change in area for both cavities. More specifically, the data indicates that the area to the left of the blind was decreasing while the area to the right of the blind was increasing, coinciding with the observation that the blind did not hang perfectly vertical (Figure 3.22). The reason for the poor alignment was due to the weight of the stopper attached to the bottom of the blind which had the effect of pulling the blind back towards its center of mass (in line with the vertical axis of the spindle). In order to verify the effect of this observation, the blind angle was approximated as 3° and modelled as such in FLUENT. The results can be seen in Figure 3.23 where the non-vertical designation refers to the case where the blind was modelled at 3° off-vertical. The velocity profile corroborates the suspicion that the angle of the blind was affecting the velocity profile, as discussed above. With this correction made in FLUENT, the numerical data matches very well with the experimental data.

Unfortunately, while the experimental data was being gathered, a probe was left in the region of the flow, whose affects can be seen to the right of the blind where a sudden drop in the velocity profile is observed. This deceleration of the flow immediately adjacent to the probe would cause an acceleration of the flow outside of this region by conservation of mass principles. This acceleration explains the more rounded

profile one would expect from laminar flow as compared to the sharp boundary layer associated with turbulent profile, as observed with the velocity profile to the left of the blind.

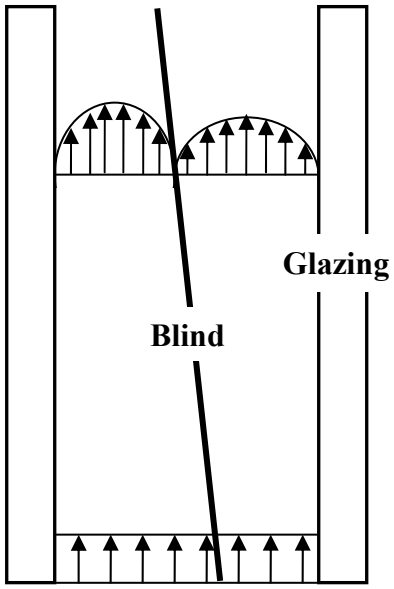

Figure 3.21: Schematic depicting effect of sloping blind on air velocity through cavity.

Data set B: Temperature profiles for all surfaces were generated in FLUENT and compared to the experimental data (Table 3.9). In particular, the temperatures of the two glazings (Figure 3.24) were compared to the numerical results.

It can be seen from Figure 3.24 that the temperature profiles predicted by FLUENT match very closely the experimental data. Error bars have been added to both the right and left glazing data points. The error bars for the left glazing show 10% error on either side while the error bars for the right glazing show 5% error on either side. The discrepancy between the numerical and the experimental data can be attributed to the many assumptions that were previously stated.

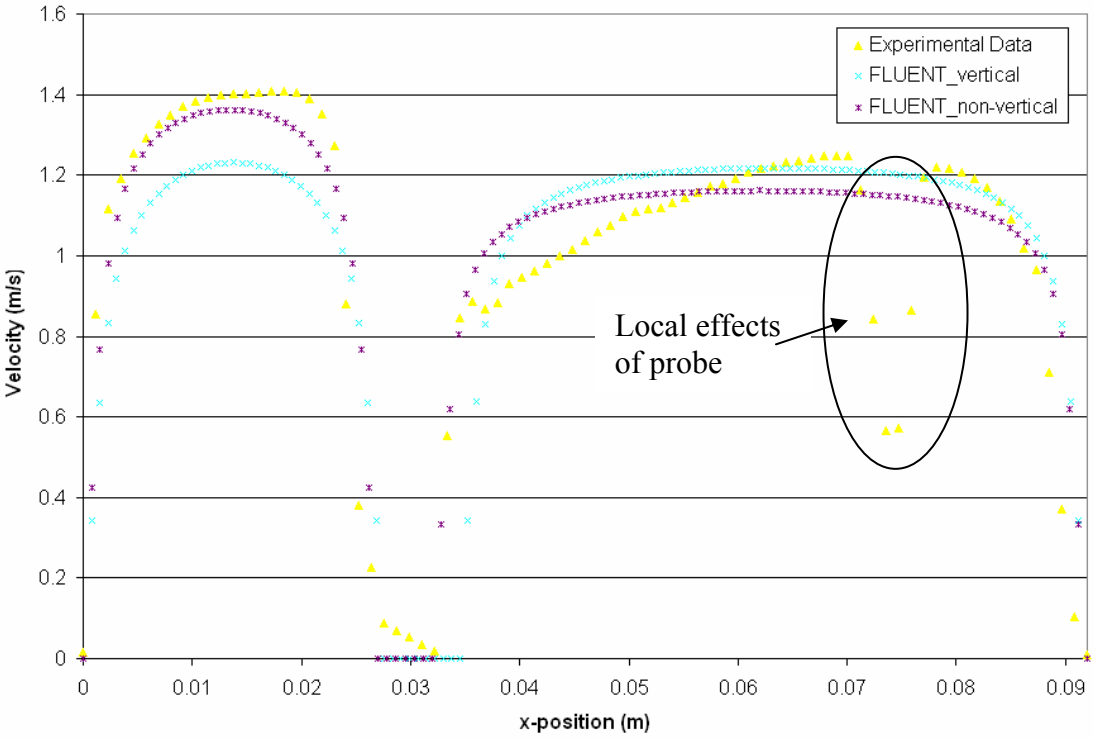

Figure 3.23: Velocity profile comparing experimental data to FLUENT results.

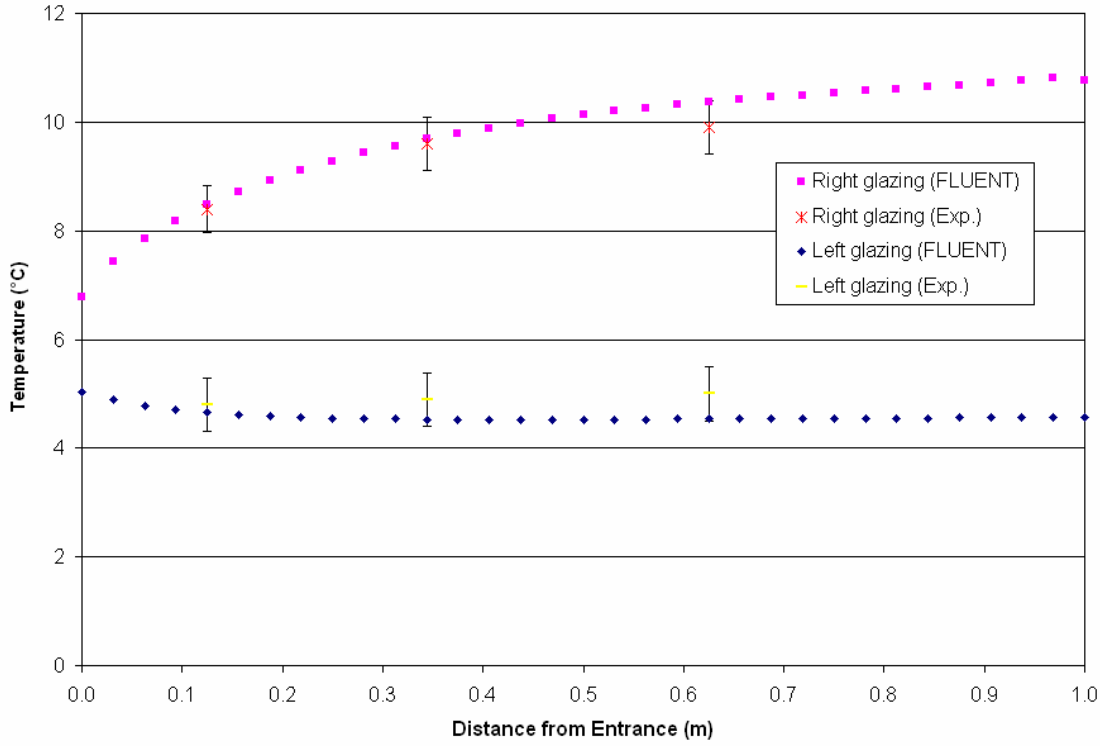

Figure 3.24: Temperature profile comparing experimental data to FLUENT results.

Given the exhaustive validation exercise detailed in this chapter, it is believed that the model performs to a high standard and that investigations aimed at the optimization of such a system can now be performed with utmost confidence in the results.

Chapter 4

Parametric Analysis of Airflow Window

4.1 Introduction

Having completed the validation of an AFW model with a between-the-panes shading device, the next step was to perform a parametric analysis. Although the intent is to eventually optimize the BIPV/T system for both winter and summer conditions, the current focus of the design optimization is for the winter season, where the thermal energy can be used for space heating. For the parametric analysis, model inputs were varied and the corresponding changes to the system performance were measured. The performance of the system was rated in terms of the total useful heat generated (q_{useful}):

$$q_{useful} = q_{out,left} + q_{out,right} - q_{in,left} - q_{in,right} - q_{room} \quad \textbf{4.1}$$

where the first four terms represent the heat transfer due to advection and the last term (q_{room}) represents the heat loss from the room. Each of the four terms of Eq. 4.1 are depicted in Figure 4.1.

As the current analysis pertains to winter conditions, historical weather data for Montreal, Quebec was used to generate the design conditions that make up the boundary conditions to the numerical model. A list of the relevant model inputs are presented in Table 4.1.

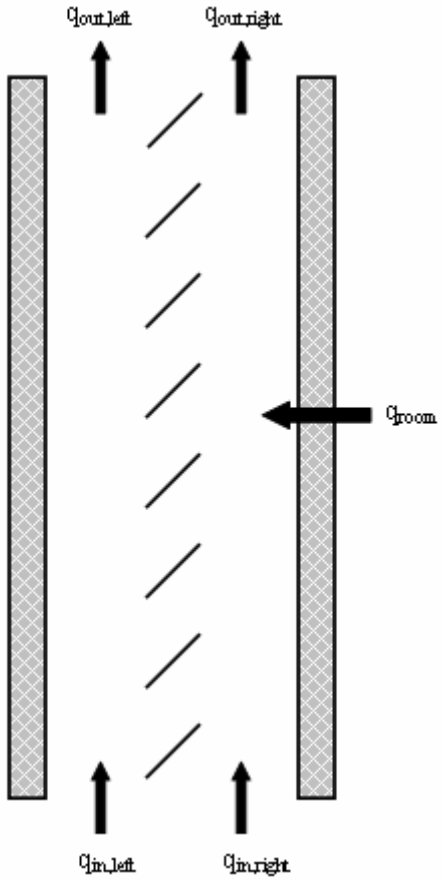

Figure 4.1: Schematic of net energy exchange within the AFW with between-the-panes roller blind.

Table 4.1: Model inputs for winter design conditions.

Parameter	***Value***	***Explanation***
G_s (W/m^2)	0, 165, 330 and 660	normal incident solar irradiance (insolation)
$h_{conv,out}$ (W/m^{2}K)	13.75	outdoor convective coefficient
$h_{conv,in}$ (W/m^{2}K)	2	indoor convection coefficient
T_{out} (°C)	-10	outdoor ambient temperature
T_{in} (°C)	21	indoor ambient temperature
T_w (°C)	20	indoor wall temperatures
$T_{air,in}$ (°C)	-5.7	air temperature at AFW inlet

4.2 Design Conditions

Solar irradiance: The solar irradiance values (G_s) in Table 4.1 were derived from historical values of the monthly average daily radiation in January for the Montreal region. Using a monthly-averaged daily radiation value of 5.30 MJ/m^2 (Beckman, 1991)

and the knowledge that there are approximately 9 hours of daily sunlight during the month of January, an average flux of 165 W/m^2 is obtained. As this is simply an average, peak insolation levels exceeding this value will also be incident upon the AFW. Hence, insolation values of 330 and 660 W/m^2 were also used to measure the performance of the AFW. In order to test for a complete range of irradiance values, the limiting case of no irradiance was also investigated. For the sake of classification, the insolation values of 165, 330 and 660 W/m^2 will be referred to as low, medium and high irradiances'. As explained in Section 3.5.2 of Chapter 3, the use of VISION to calculate the absorbed energy of the two glazings and the shading device requires the incident radiation to be completely diffuse. As such, overcast conditions were used for all of the models in this chapter whereby the sky temperature is set equal to the outside ambient temperature.

Outdoor convection coefficient: The outdoor heat transfer coefficient for convection was calculated using Eq. 3.47. The average wind speed for the month of January in Montreal for the year 2006 was approximately 4.5 m/s (Environment Canada), resulting in an average outdoor convective heat transfer coefficient of 13.75 W/m^{2}K.

Indoor convection coefficient: The indoor heat transfer coefficient for convection was determined using a thermal resistance network between the indoor and outdoor environment. The details of the analysis were explained in Section 3.5.2 of Chapter 3. A value of 2 W/m^{2}K was used, resulting in an approximate indoor wall temperature of 20°C, which is a 1° drop from the inside ambient air temperature.

Indoor, outdoor and inlet temperatures: According to ASHRAE Fundamentals (2005), 21°C is a comfortable indoor temperature during the winter season. In Montreal, for the month of January, historical data (Beckman, 1991) indicates that the average outdoor

temperature is approximately -10°C. The temperature of the sky was also set at -10°C as the sky was assumed to be completely overcast. According to Liao (2005), for a solar irradiance of 150 W/m^2, an increase in air temperature of 4.3° was measured through the BIPV section of the PhotoWatt configuration. As this was the only data available, this temperature rise was used to determine the air temperature at the inlet of the AFW section. For an outdoor ambient temperature of -10°C, a 4.3° temperature rise results in an average air inlet temperature of -5.7°C for the AFW section. Note that this temperature rise was used for all levels of insolation, with the exception of zero irradiance, where no temperature rise was used.

Using the above described parameters as boundary conditions, a set of models were developed and the results are presented in the following sections.

4.3 Low-emissivity coatings

For regular fenestration systems, low-E coatings are used to decrease the U-value. During the winter, coatings reduce the heat loss from the inside environment to the outdoors (Section 1.6.3 of Chapter 1). Low-E coatings are effective in glazing systems where the radiative heat transfer coefficient is of the same magnitude as the convective coefficient. For applications where convection dominates, it is reasonable to believe that the effectiveness of the low-E coating is reduced to the point of being invaluable. This observation was verified by modelling two identical systems, one with the low-E and one without. The useful heat gain (Eq. 4.1) of the AFW was measured for a mean inlet velocity of 0.7 m/s (Re = 8,800) for all three irradiance values, namely 165, 330, 660 W/m^2. The difference between the system with low-E and the system without was evaluated and the results presented in Table 4.2.

Table 4.2: Effect of low-E coating on q_{useful}.

G_s (W/m^2)	*Difference (%)*
165	5.7%
330	0.4%
660	0.9%

The difference, in percentage, was calculated as:

$$\frac{q_{useful,low-E} - q_{useful}}{q_{useful,low-E}} \times 100\% \quad \textbf{(4.2)}$$

where q_{useful} is the useful heat gained by the AFW without low-E ($\epsilon = 0.84$). Note that the emissivity of the low-E coating is $\epsilon = 0.1$. As expected, the results indicate that use of a low-E coating in conjunction with an AFW is relatively ineffective.

4.4 Mass Flow Rate versus Outlet Temperature

One of the parameters that is used to control the heat output of the system is the mass flow rate. Increasing the mass flow rate will increase the convective heat transfer coefficient inside the air cavity. Although an increase in mass flow rate will increase the heat transfer coefficient, it will reduce the temperature of the air leaving the cavity. Depending on the HVAC system, it may be critical to maintain a particular air temperature at the outlet of the AFW. Due to the presence of the shading device, the air leaving the BIPV section will be split into two distinct air streams. The air temperature at the outlet is plotted as a function of mean inlet velocity for both the left and right side of the blind in Figure 4.2 and 4.3, respectively. Note that the data has been plotted for a range of velocities of which the lowest velocity, namely 0.1 m/s, corresponds to laminar flow; all other velocities produce turbulent flow. As the mass flow rate is increased, the average outlet temperature is observed to approach the temperature at the inlet of the AFW. As a point of reference, the outdoor ambient temperature has also been plotted, which is 4.3°C cooler than the inlet temperature.

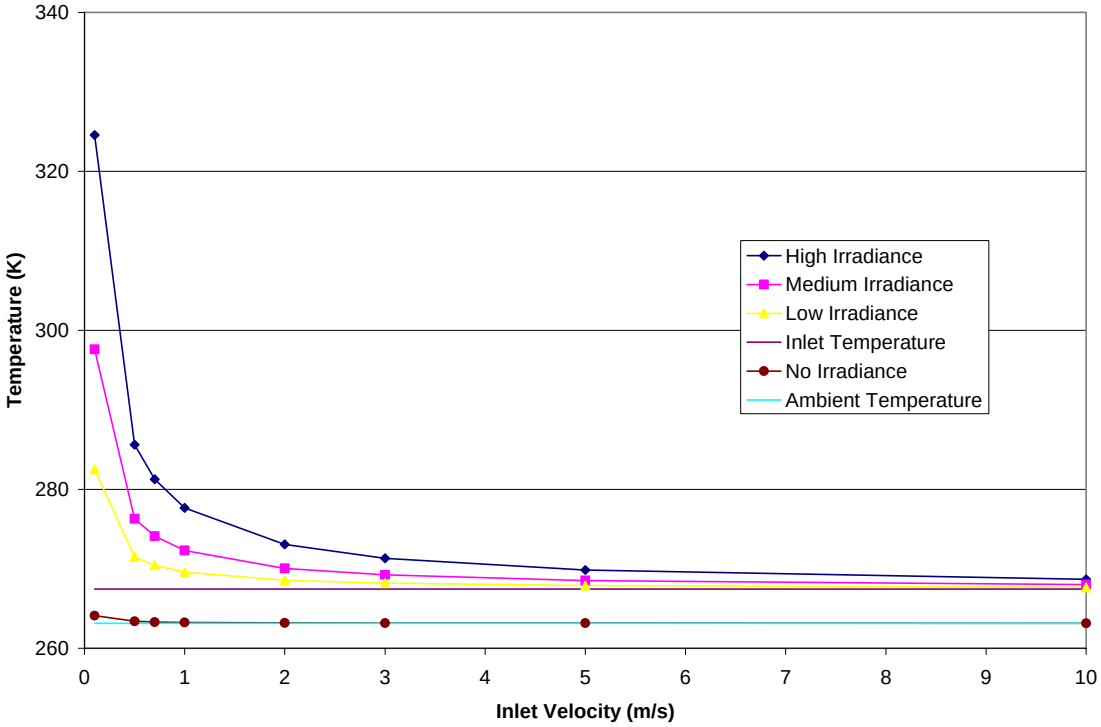

Figure 4.2: Effect of velocity on outlet temperature for left side of shading device.

At higher irradiance values, the flow rate has a greater effect on the air temperature as there is more thermal energy available to the air. For example, when the inlet velocity increases from 0.1 m/s to 0.5 m/s, the average temperature of the air at the outlet drops by 39°C for 660 W/m^2 of insolation compared to only 11°C an insolation value of 165 W/m^2, respectively. Temperatures on the left side of the blind tend to be higher as the solar absorption in the outside glazing is greater than that of the inside glazing. For the case with zero irradiance, the outlet air temperature on the left side of the blind is equal to the ambient air temperature, except at very low velocities where the air will warmed by modest amounts due to the energy lost by the room. That energy lost by the room is also responsible for the slight rise in temperature at the right side of the blind.

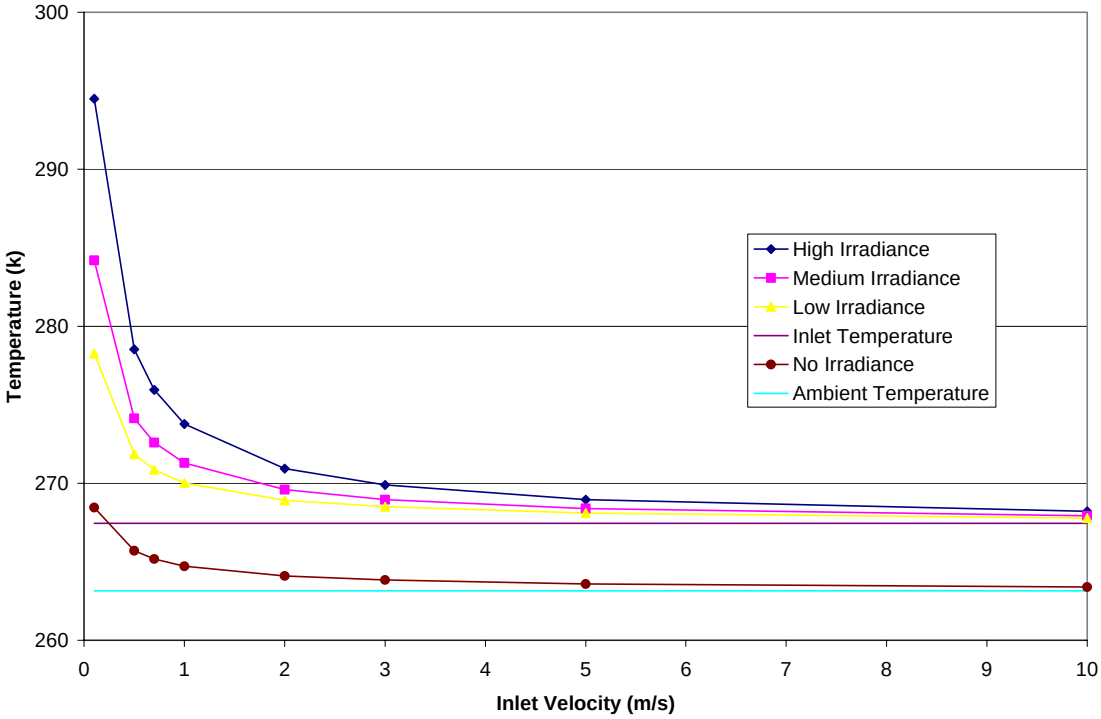

Figure 4.3: Effect of velocity on outlet temperature for right side of shading device.

4.5 Useful Heat Captured versus Inlet Velocity

The thermal efficiency of system (and hence its performance) can be measured by calculating the total useful heat gained by the building (Eq. 4.1). For each of the four irradiance values, the total useful heat gain was plotted as a function of mean inlet velocity. Due to the similarities between the first three cases, only the low irradiance and the zero irradiance cases are shown (Figure 4.4 and 4.5). For each plot, a distinction was made between the gains due to advection and the losses from the room; the useful heat gain to the building is the sum of sum of the gains and losses. What is interesting to note is that the useful energy gains grow very rapidly initially but show diminishing returns at higher inlet velocities. In Figure 4.4, the useful heat gained for the low irradiance case levels off around 190 W. Beyond 10 m/s, it is expected that very little change will occur as the advective gains begin to slow. Although the convective coefficient continues to

increase with increasing mass flow rates, the difference between the wall and the bulk fluid temperature decreases. At high flow rates, the bulk fluid temperature approaches the inlet temperature (as seen in Figures 4.2 and 4.3) while the wall temperature drops, resulting in small advective gains. A similar trend was seen for the two higher irradiance cases where only marginal gains were realized above 3 m/s. For comparison purposes, all four irradiance cases have been presented together as a function of inlet velocity in Figure 4.6. For all irradiance cases, there appears to be a velocity beyond which an increase in flow rate is no longer beneficial.

For the zero irradiance case (Figure 4.5), very little heat is gained at any mass flow rate. At 10 m/s, the heat gain is approaching 25 W. Note that for this case, it was assumed that the inlet air temperature to the AFW was the same temperature as the ambient air. This would be the case during the night or early morning when the system has been cooled to ambient and no heat is being produced from the BIPV (unlike during periods of passing cloud cover where irradiance may be zero but heat continues to emanate from the PV).

Effects of Outside Temperature: The effects of outdoor ambient temperature were investigated for the low irradiance case (Figure 4.7). It can be seen that at cooler temperatures, more heat gain is obtained due to the greater temperature gradient. A comparison of the three curves in Figure 4.7 indicates that a similar operating point would exist for all three cases. It is therefore evident that a potential operating point is more a function of the irradiance level than it is of the ambient outdoor temperature.

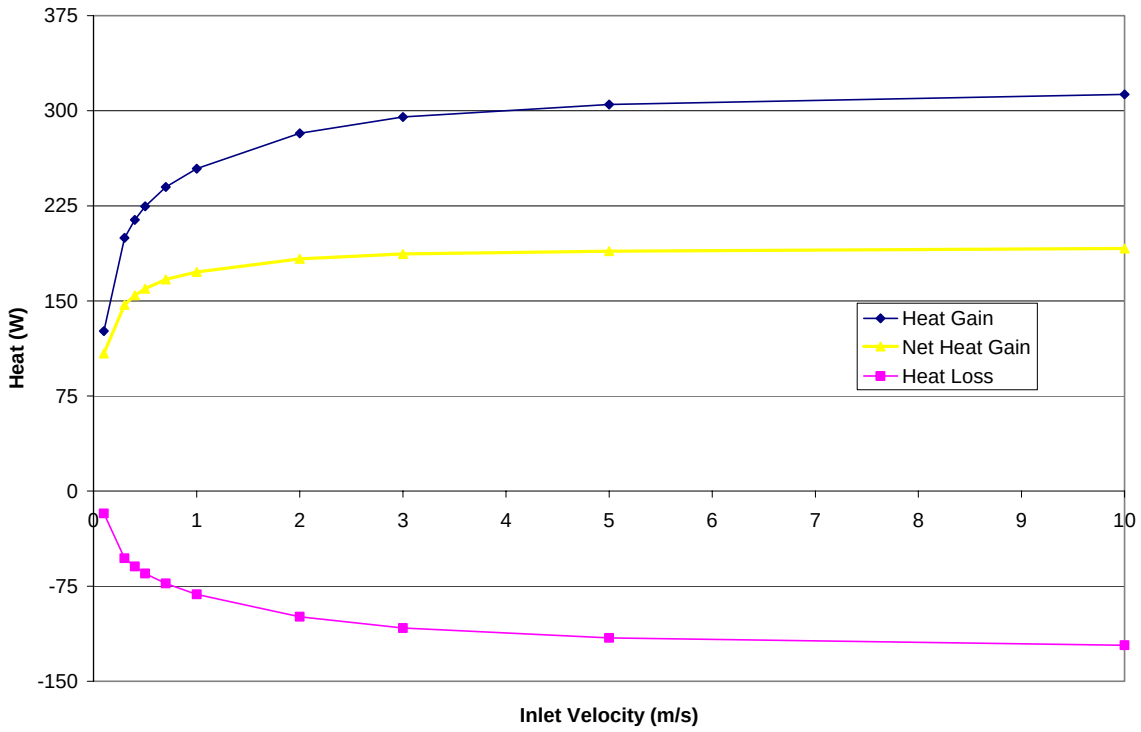

Figure 4.4: Overall heat exchange within the BIPV/T system for low irradiance (165 W/m^2).

4.6 Fan Performance

Although speculation pertaining to operating points can be made based on the profiles of each curve presented in Figure 4.6, a conclusive statement can not be made without knowing the energy draw from the fan which is providing the forced convection. The fan system used to provide the forced convection was an AC Tech model with part number M1105SB whose operating frequencies varied from 0 – 120 Hz (Liao, 2005). A figure describing the fan power and torque as a function of frequency was obtained from the AC Tech website and is shown in Figure 4.8. At 60 Hz the power required to turn the fan was 370 W; the total torque required at that frequency was calculated using:

$$HP = J\Psi \tag{4.3}$$

where the angular velocity of the fan was

$$\Psi = 2\pi f \tag{4.4}$$

where f is the frequency of the fan, J and HP are the torque and power required to turn the fan, respectively, and Ψ is the fan's angular velocity. Once the torque was obtained for a frequency of 60 Hz, Figure 4.8 was used to obtain the power demand of the fan for any frequency between 0 and 120 Hz. The performance curve of the fan was superimposed on Figure 4.6 as seen in Figure 4.9. By subtracting the fan power consumption from the useful power gained through the AFW, the net heat gain of the system was determined and plotted in Figure 4.10. For the case where no irradiance is present, the results indicate that it is best to not operate the fan as a net loss is incurred for all mass flow rates. For the case with low irradiance, an operating velocity of approximately 0.3 m/s (Re = 3,800) provides the maximum net heat gain to the system (122 W). As the irradiance levels rise, the operating point shifts towards higher mass flow rates. For the medium and high irradiance cases, the operating points were found to be approximately 0.6 m/s (Re = 7,600) and 1 m/s (Re = 12,600), respectively. For the medium and high irradiance levels, a maximum net heat gain of 295 W and 700W were obtained, respectively.

From the data of Figure 4.10, operating points for the fan were plotted as a function of insolation level (Figure 4.11). The points in Figure 4.11 can be fitted with a second order polynomial curve and mathematical expressions can be used to obtained the ideal inlet velocity (Eq. 4.5) or Re number (Eq. 4.6) as a function of insolation (G_s):

$$U = -8 \cdot 10^{-7} G_S^2 + 0.002 G_S \quad \textbf{(4.5)}$$

$$\mathrm{Re} = -0.0101 G_S^2 + 25.766 G_S \quad \textbf{(4.5)}$$

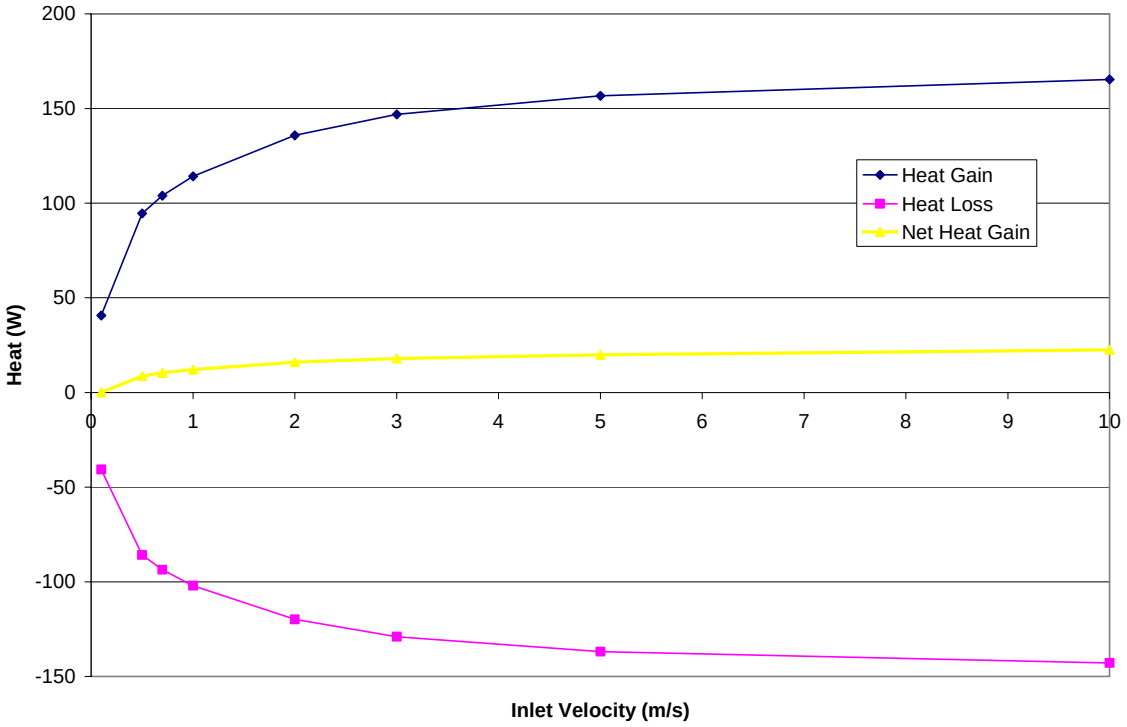

Figure 4.5: Overall heat exchange within the BIPV/T system for zero irradiance (0 W/m^2).

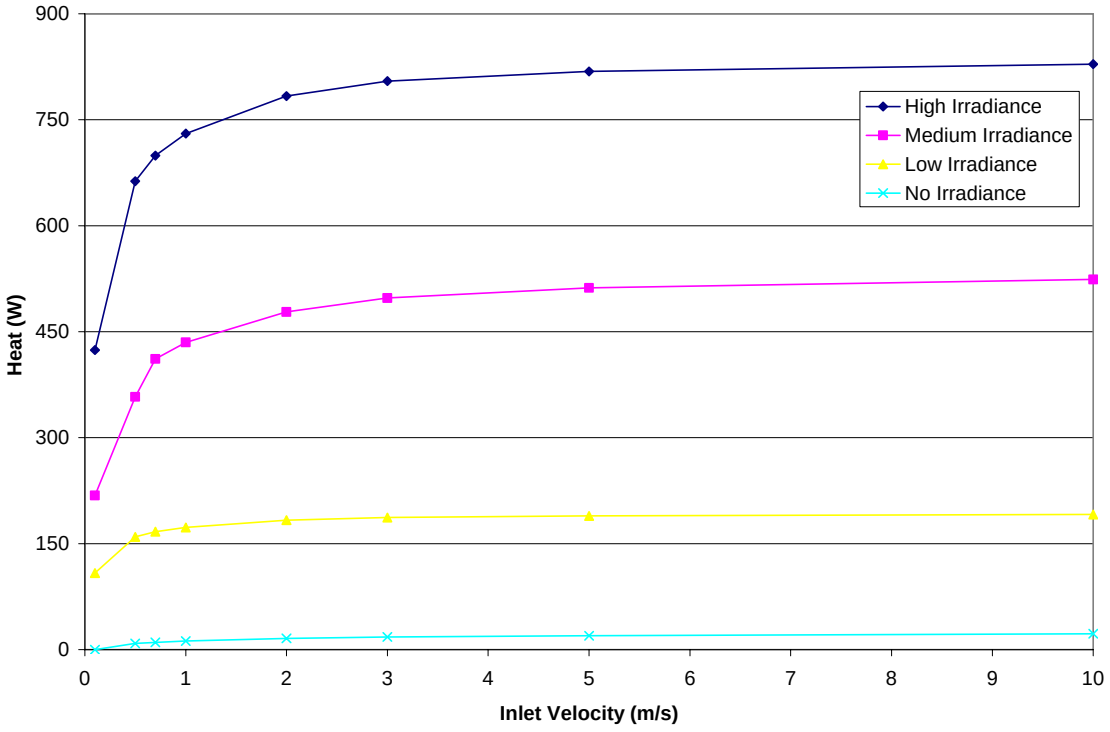

Figure 4.6: Effect of velocity on useful heat gain as a function of irradiance.

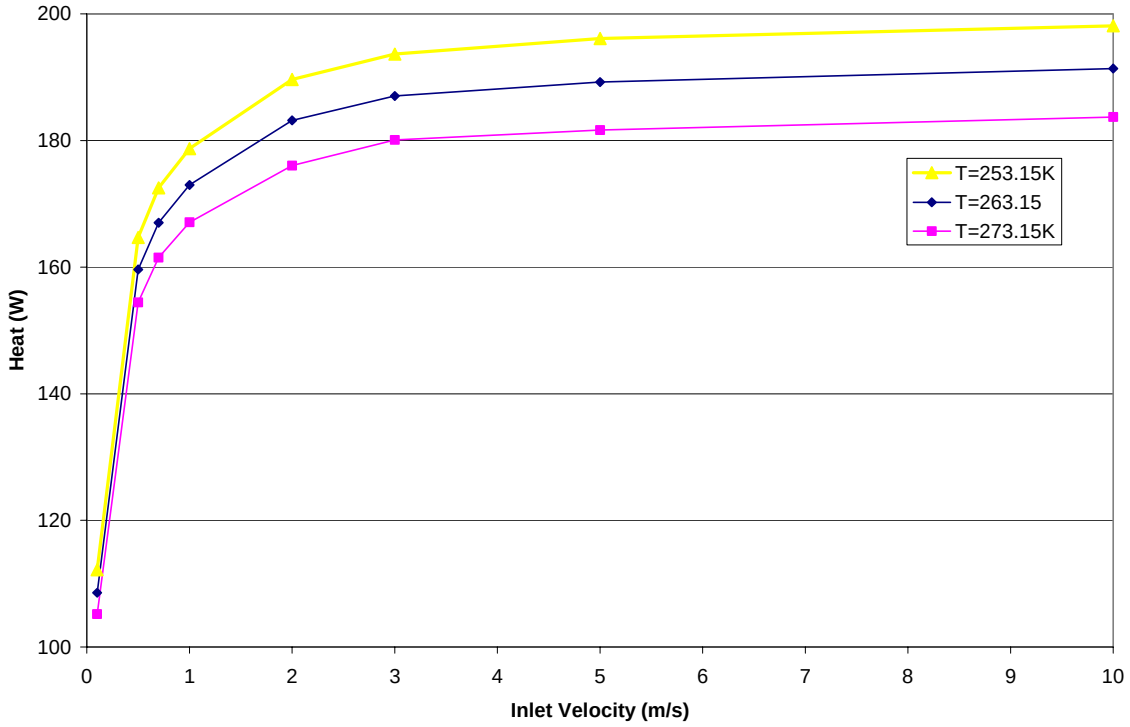

Figure 4.7: Useful heat gain as a function of temperature for low irradiance case (165 W/m^2).

Effects of Outside Temperature: The effects of outdoor ambient temperature on the operating velocity were also evaluated (Figure 4.12). As can be seen, the outdoor temperature has no noticeable effect on the operating point. These results are consistent with the data plotted in Figure 4.7.

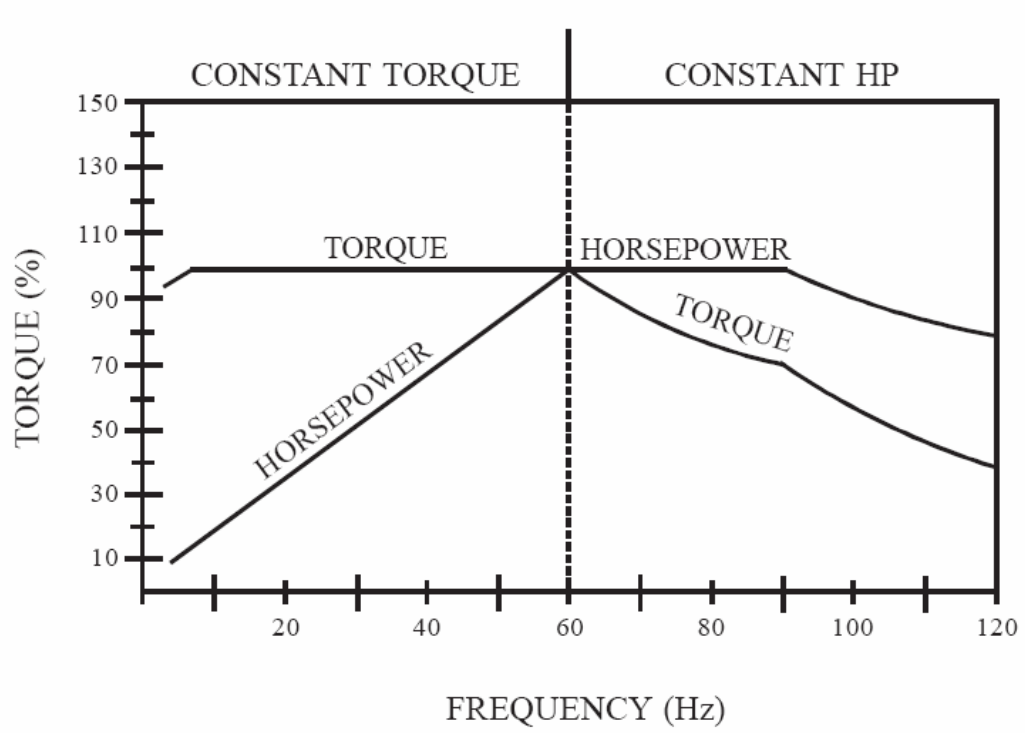

Figure 4.8: Fan power and torque as a function of frequency (AC Tech).

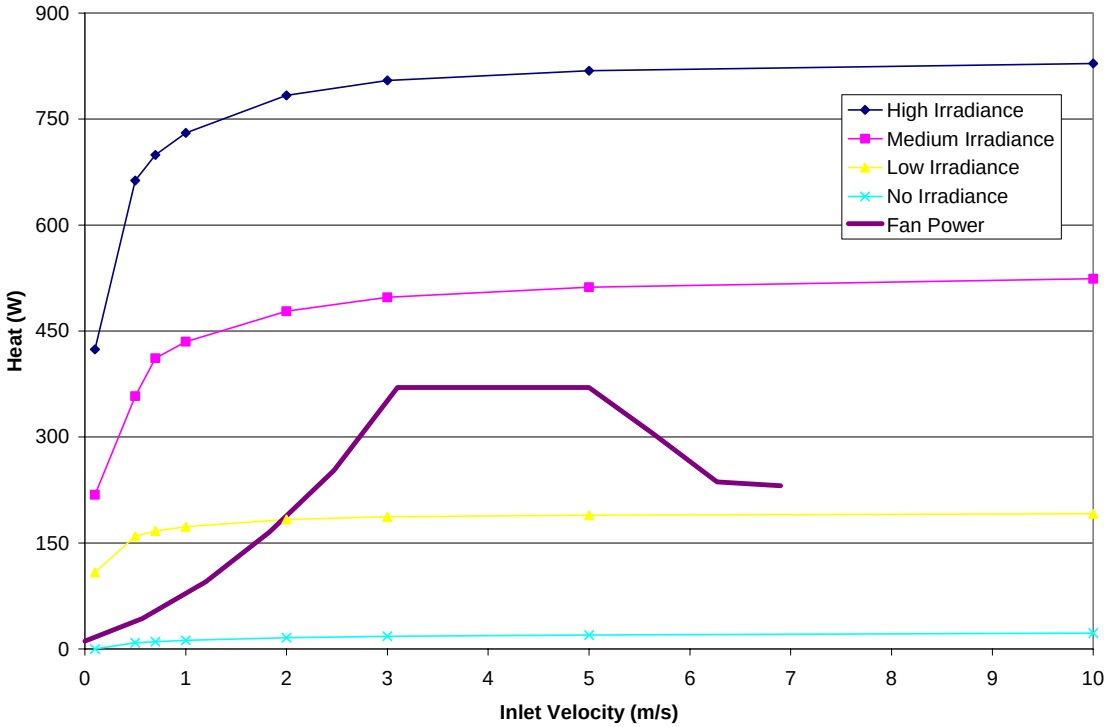

Figure 4.9: Effect of velocity on useful heat gain as a function of irradiance including fan performance curve.

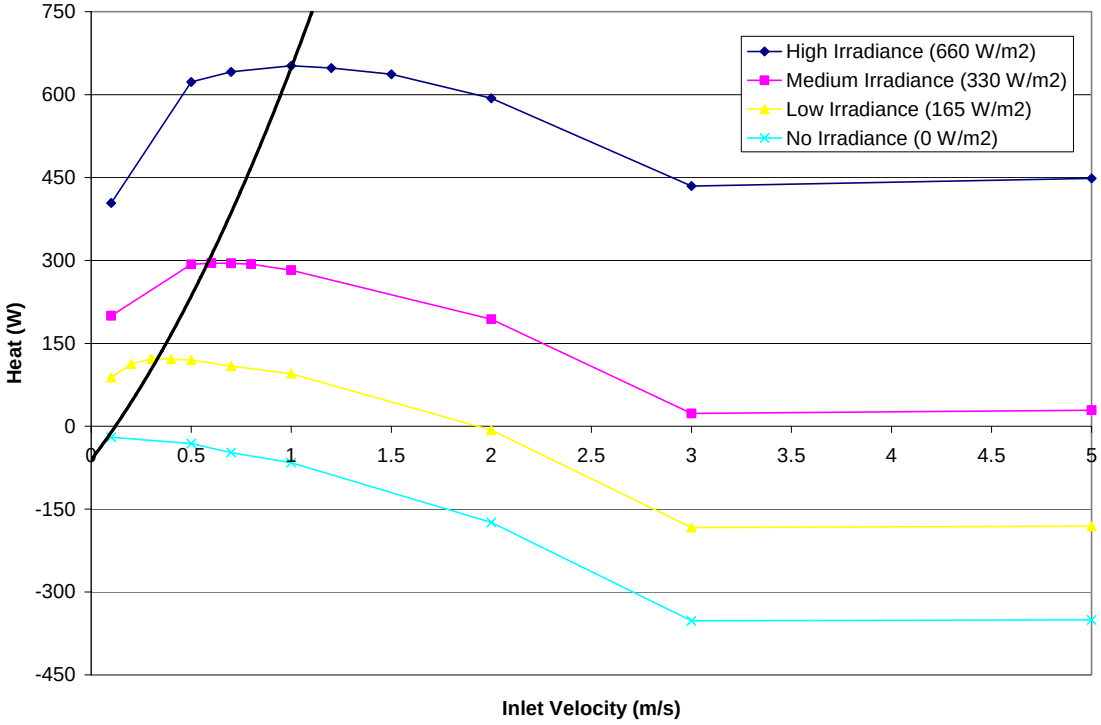

Figure 4.10: Net useful heat gain including fan losses.

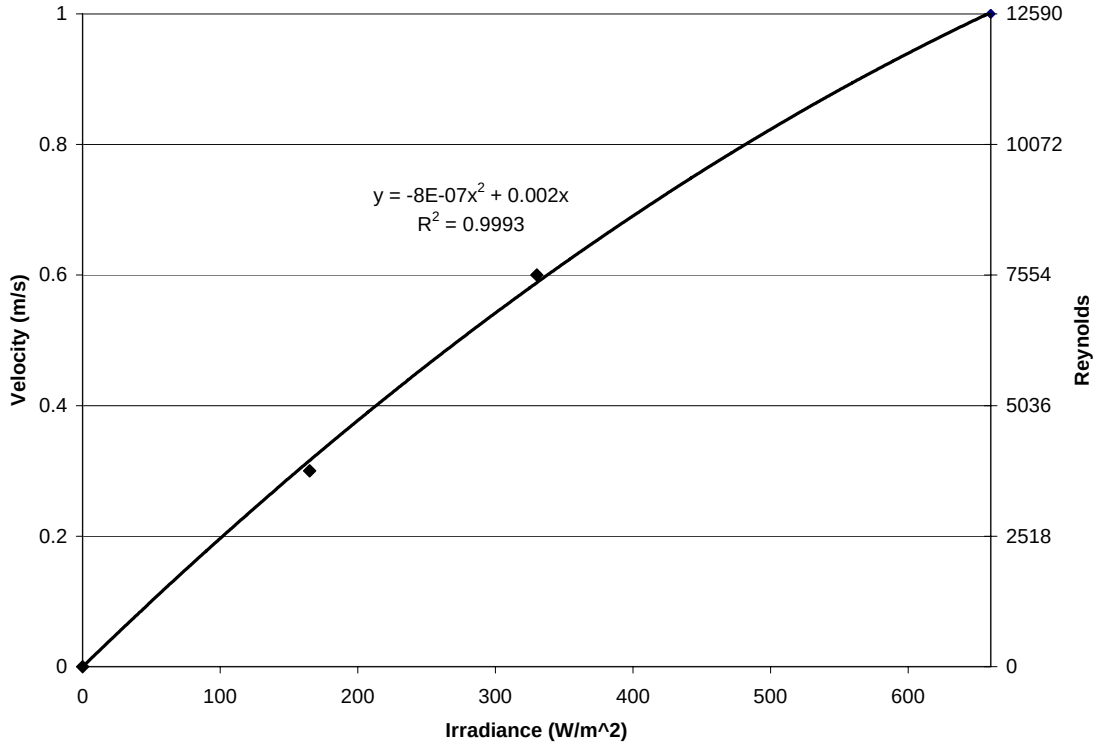

Figure 4.11: Operating point as a function of irradiance for the AFW section of Configuration 1.

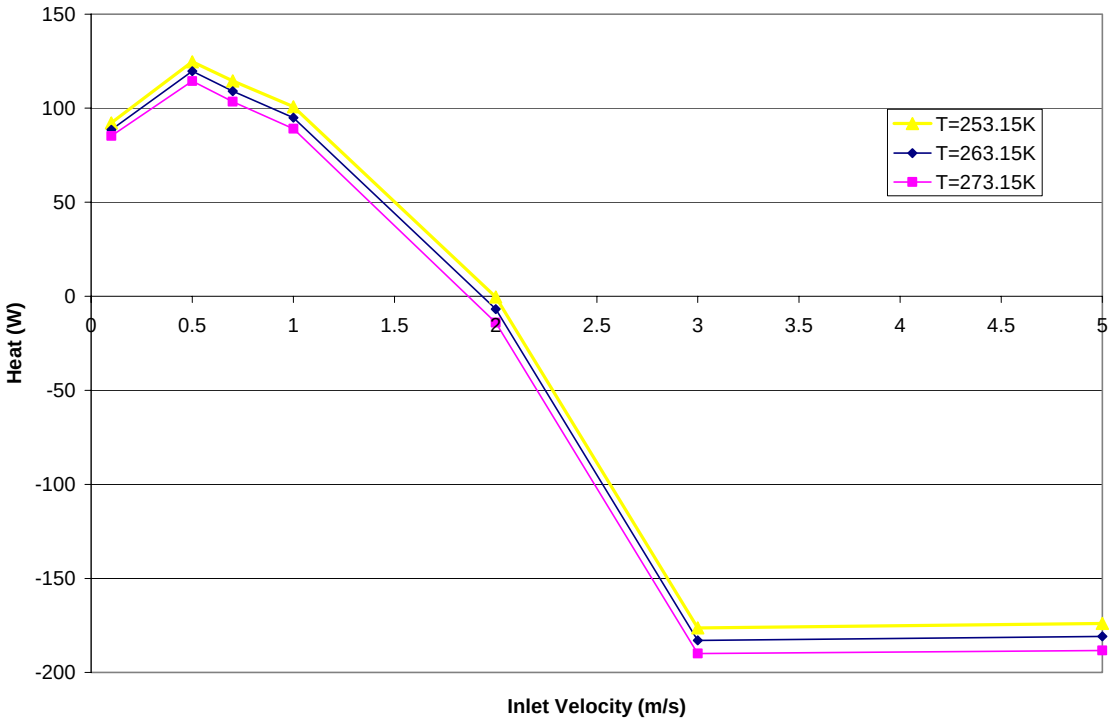

Figure 4.12: Net useful heat gain as a function of outside ambient temperature for low irradiance case (165 W/m^2).

Chapter 5

Conclusions and Recommendations

5.1 Conclusions

A numerical model of an AFW comprising two glazings with a between-the-panes shading device has been validated for forced convection without radiation, natural convection with radiation and finally forced convection with radiation. Results from the numerical model were compared to data obtained from the Solar Lab at Concordia University. Both the hydrodynamic and thermodynamics results from the model compared well with experimental data.

With the fully validated model, the useful energy generated by the AFW as a function of mass flow rate was calculated. By subtracting the power required by the fan, the net useful energy of the system as a function of insolation was obtained. From this data, the operating points for four different levels of insolation, namely 0, 165, 330 and 660 W/m^2 were determined. Furthermore, an accurate representation of the data was achieved using a second order polynomial curve fit:

$$\mathrm{Re} = -0.0101 G_S^2 + 25.766 G_S$$

where the x-value is the irradiance and the y-value is the corresponding Reynolds value. Although the operating points were strongly dependent on insolation values, the outdoor ambient temperature seemed to have little effect on the operating point. Although low-E in a typical fenestration system provides useful benefits, the use of low-E for an AFW was shown to be of little value as the convection heat transfer was dominant of the radiative heat transfer.

5.2 Recommendations

- With the current model, the outlet boundary was modelled as an opening between two plates. In reality, upon leaving the AFW section, the air takes a 90° turn through an exit duct. A representative duct should therefore be added to the existing model. It is expected that an increase in pressure drop will be observed which will have an effect on the fluid dynamics of the system.

- Having modelled the roller blind, it is recommended that venetian blinds be modelled. The use of venetian blind may be a more attractive solution as enhanced heat transfer can be accomplished with slats. As described in Chapter 2, the heat transfer within a thin cavity is affected by the angle of the slats and can be used to maximize the thermal efficiency of the AFW section.

- Both the BIPV and AFW sections have now been modelled. It is recommended that the two models be combined into a single unifying model. Currently, velocity and temperature profile at the inlet of the AFW section is approximated using either experimental or numerical data from the PV section. By unifying the two models, fewer approximations and assumptions will be required, thus making the model accurate.

- During the validation of the model, experimental data was used for which all of the insolation was purely diffuse. Due to the diffuse nature of the radiation, the software VISION could be used to provide the appropriate volumetric source terms for each layer. However, as explained in Chapter 3, VISION should not be used for shading devices when beam radiation is present. It is therefore recommended that the model developed by Wright and Kotey (2006) be used to obtain the absorbed quantities at each layer.

References

AC Tech, *MC1000 Series Installation and Operation Manual*. Retrieved July 19, 2006, from http://www.actech.com/index.html.

ASHRAE, 1993, *Handbook of Fundamentals*, F26.17-39, New York.

ASHRAE, 2005, *Handbook of Fundamentals,* Chapter 8 – Thermal Comfort, Atlanta.

Athienitis, A., Liao, L., Charron, R., Collins, M., Poissant, Y., Park, K.W., 2004, Experimental and Numerical Results for a Building-Integrated Photovoltaics Test Facility with Generation of Electricity and Heat, *Proc. Solar Energy Societyof Canada Inc.*, August 21-25, Waterloo, Ontario, Canada.

Athienitis, A., 2006, *Personal Communications,* April.

Aung, W., 1972, Developing Laminar Free Convection Between Vertical Flat Plates with Asymmetric Heating, *Int. J. Heat Mass Transfer*, Vol. 15, pp. 2293-2308.

Azer, N.Z. and Choa, H.T., 1960, A Mechanism of Turbulent Heat Transfer in Liquid Metals, *Int. J. Mass Transfer 1*, pp. 121.

Balocco, C., 2002, A Simple Model to Study Ventilated Energy Performance, *Energy and Buildings*, Vol. 34, June, pp. 469-475.

Balocco, C., Colombari, M., 2006, Thermal Behaviour of Interactive Mechanically Ventilated Double Glazed Façade: Non-dimensional Analysis, *Energy and Buildings*, Vol. 38, January, pp. 1-7.

Bansal, S.N.K. and Gaur, R.C., 1996, Application of *U* and *g* Values for Sizing Passive Heating Concepts, *J. Solar Energy*, Vol. 57, pp. 361-373.

Beckman, W.A. and Duffie, J.A., 1991, Solar Engineering of Thermal Processes, Second Ed., *John Wiley & Sons, Inc.*, pp. 175.

Brandemuehle, M.J. and Beckman, W.A., 1980, Transmission of Diffuse Radiation Through CPC and Flat-Plate Collector Glazings, *J. Solar Energy*, Vol. 24, pp. 511-513.

Brinkworth, B.J., Marshall, R.H. and Ibarahim, Z., 2000, A Validated Model of Naturally Ventilated PV Cladding, *J. Solar Energy*, Vol. 69, pp. 67-81.

Burmeister, L.C., 1993, Convective Heat Transfer, Second Ed., *John Wiley & Sons, Inc.*, New York, pp. 140.

Charron, R. and Athienitis, A.K., 2003, A Two-Dimensional Model of a PV-Integrated Double-Façade, *SESCI 2003 Conference*, August 18-20, Kingston, Ontario, Canada.

Charron, **R**., 2004, One- and Two-Dimensional Modelling of Ventilated Façades with Integrated Photovoltaics, *MASc Thesis*, Concordia University, Montreal, Quebec, Canada.

Cho, S.H., Shin, K.S and Zaheer-Uddin, M., 1995, The Effect of Slat Angle of Windows with Venetian Blinds on Heating and Cooling Loads of Buildings in South Korea, *Energy (Oxford)*, Vol. 20, December, pp. 1225-1236.

Christie, E.A. and Hunter, A.J., 1984, Total Infrared Radiation Property Measurements of Diathermanous Films with a Reflectometer, *J. Solar Energy*, Vol. 33, June, pp. 613-618.

Ciampi, M., Leccese, F. and Tuoni, G., 2003, Ventilated Façades Energy Performance in Summer Cooling of Buildings, *J. Solar Energy*, Vol. 75, December, pp. 491-502.

Collins, M.R. and Wright, J.L., Calculating Performance Indices for Windows with Diathermanous Layers, *ASHRAE Transaction,* Vol. 112 (2).

Davis, M.W., Hunter, F.A. and Dougherty, B.P., 2001, Prediction of Building Integrated Photovoltaic Cell Temperatures, *J. Solar Energy Engineering*, Vol. 123, August, pp. 200-210.

DOE (U.S. Department of Energy), 2002*,* Buildings Energy Databook, *Office of the Energy Efficiency and Renewable Energy.*

DOE (U.S. Department of Energy), 2004a, Annual Energy Review, *Office of the Energy Information Administration*.

DOE (U.S. Department of Energy), 2004b, Energy Consumption, Expenditures, and Emissions Indicators, 1949-2004, *Office of the Energy Information Administration*.

DOE (U.S. Department of Energy), 2005a, Buildings Sector Energy Consumption - U.S. Residential and Commercial Buildings Total Primary Energy Consumption, *Office of the Energy Information Administration, 2005 Buildings Energy Databook.*

DOE (U.S. Department of Energy), 2005b, Residential Sector Energy Consumption – 2003 Residential Energy End-Use Splits, by Fuel Type, *Office of the Energy Information Administration, 2005 Buildings Energy Databook.*

DOE (U.S. Department of Energy), 2005c, Commercial Sector Energy Consumption – 2003 Commercial Energy End-Use Splits, by Fuel Type, *Office of the Energy Information Administration, 2005 Buildings Energy Databook.*

Environment Canada, Weather for Montreal, Quebec: Wind Speed. Retrieved July 7, 2006, from http://montreal.weatherstats.ca/wind_speed.

Erbs, D.G., Klein, S.A. and Duffie, J.A., Estimation of the Diffuse Radiation Fraction for Hourly, Daily, and Monthly-Average Global Radiation, *Solar Energy*, Vol. 28, 293.

FLOVENT Version 3.2, 2001, Manual, Flomerics Ltd., Hampton Court, UK.

FLUENT 6.2, User's Guide, 2005.

Fohanno, S. and Polidori, G., *Energy and Buildings,* Modelling of Natural Convective Heat Transfer at an Internal Surface, Vol. 38, May, pp. 548-553.

Gratia, E. and De Herde, A., 2004, Natural Ventilation in a Double-Skin Façade, *Energy and Buildings*, Vol. 36, February, pp. 137-146.

Hatton, A.P. and Quarmby, 1963, The Effect of Axially Varying and Unsymmetrical Boundary Conditions on Heat Transfer with Turbulent Flow Between Parallel Plates, *Int. J. Heat Mass Transfer*, Vol. 6, pp. 903-915.

Hatton, A.P., Quarmby, A. and Grundy, I., 1964, Further Calculations on the Heat Transfer with Turbulent Flow Between Parallel Plates, *Int. J. Heat Mass Transfer*, Vol. 7, pp. 817-823.

Hollands, K.G.T., Wright, J.L., Granqvist, C.G., 2001, *Solar Energy – The State of the Art – ISES Position Papers,* James & James Ltd. Ch. 2 (Glazings and Coatings), pp. 29-107.

Huang, N.Y., 2005, Thermal Performance of Double Glazed Windows with Inter-Pane Venetian Blinds, *MASc Thesis*, University of Waterloo, Waterloo, Ontario, Canada.

Hunter, A.F. And Dougherty, B.P., 2001, Measured Performance of Building Integrated Photovoltaic Panels, *Int. Solar Energy Conference, Solar Engineering 2001, Proc. Int. Solar Energy Conference,* pp. 295-304.

Incropera, F.P. and DeWitt, D.P., 2002a, Fundamentals of Heat and Mass Transfer, Fifth Ed., *John Wiley & Sons, Inc.*, New York, pp. 540-570.

Infield, D.G., Mei, L., Lee, W.M. and Loveday, D.L., 2003, Thermal Aspects of Building Integrated PV Systems, *Proc. 3rd World Conference on Photovoltaic Energy Conversion*, May 11-18, Osaka, Japan, pp. 2354-2357.

Infield, D., Mei, L. and Eicker, U., 2004, Thermal Performance Estimation for Ventilated PV Façades, *J. Solar Energy*, Vol. 76, pp. 93-98.

Johnson, D., 2005**,** *Personal Communications – ME 770 Course Notes*, March.

Kays, W.M., 1966, Convective Heat and Mass Transfer, *McGraw-Hill, Inc.*, USA, pp. 102-145.

Kays, W.M. and Crawford, M.E., 1980**,** Convective Heat and Mass Transfer, *McGraw-Hill*, New York.

LaVision, *System Components for Particle Image Velocimetry* . Retrieved August 1, 2006, from http://www.piv.de/.

Liao, L., Athienitis, A., Park, K.W., Collins, M. and Poissant, Y., 2005, Numerical Study of Conjugate Heat Transfer in a BIPV-Thermal System, *Proc. International Solar Energy Conference*, August 6-12, Orlando, FL.

Liao, L., 2005, Numerical and Experimental Investigation of Building Integrated Photovoltaic-Thermal Systems, *MASc Thesis*, Concordia University, Montreal, Quebec, Canada.

Limb, N., 2002, Low-E Growth – Slow, But Definitely Not Low, *USGlass Magasine*, Vol 37, Issue 8, August.

Lloret, A., Andreu, J., Merten, J., Puigdollers, J., Aceves, O., Sabata, L., Chantant, M. and Eicker, U., 1998, Large Grid-Connected Hybrid PV System Integrated in a Public Building, *Progress in Photovoltaics: Research and Applications*, Vol. 6, Nov-Dec, pp. 453-464.

Lundberg, R.E., McCuen, P.A. and Reynolds, W.C., 1963, Heat Transfer in Annular Passages: Hydrodynamically Developed Laminar Flow with Arbitrarily Prescribed Wall Temperatures or Heat Fluxes, *Int. J. Heat Mass Transfer,* Vol. 6, pp. 495-529.

Machin, A.D., Naylor, D. and Oosthuizen, P.H., 1997, An Interferometric Study of the Effect of Louvers on Free Convection from a Vertical Surface, *Experimental Heat Transfer Conference Proceedings Fluid Dynamics and Thermodynamics*, pp. 2175-2182.

Manz, H., 2004, Total Solar Energy Transmittance of Glass Double Façades with Free Convection, *Energy and Buildings*, Vol. 36, February, pp. 127-136.

Mei, L., Infield, D., Eicker, U. and Fux, V., 2003, Thermal Modelling of a Building with an Integrated Ventilated PV Façade, *Energy and Buildings*, Vol. 35, July, pp. 605-617.

Messadi, T. and Augenbroe, G., 2001, A Configurable Smart Façade Unit for Onsite Calibration and Control Optimization, *ASHRAE Proc. Thermal Performance of the Exterior Envelopes of Buildings VIII: Integration of Building Envelopes*, December 2-7, Clearwater Beach, FL.

Owens, M. 1994, Building small, thinking big, *New York Times*, 21 July.

Rheault, S. and Bilgen, E., 1989, Heat Transfer Analysis in an Automated Venetian Blind Window System, *J. Solar Energy Engineering*, Vol. 111, pp. 89-95.

Rheault, S. and Bilgen, E., 1990, Experimental Study of Full-Size Automated Venetian Blind Windows, *J. Solar Energy*, Vol. 44, pp. 157-160.

Ripatti, H., 1984, Airflow Window System – Making Fenestration the Solution Rather than the Problem in Energy Use, *ASHRAE Trans*, 90, 1B, 917-924.

Rohsenow, W.M., Hartnett, J.P. and Ganic, E.N., 1985, Handbook of Heat Transfer Fundamentals, Second Ed., *McGraw-Hill, Inc.*, USA, pp.7-56.

Saelens, D. and Hens, H., 2001, Experimental Evaluation of Airflow in Naturally Ventilated Active Envelopes, *Journal of Thermal Envelope and Building Science*, Vol. 25, October, pp. 101-127.

Safer, N., Woloszyn, M. and Roux, J.J., 2005, Three-Dimensional Simulation with a CFD Tool of the Airflow Phenomena in Single Floor Double-Skin Façade Equipped with a Venetian Blind, *J. Solar Energy*, Vol. 79, August, pp. 193-203.

Santamouris, M., 2001, Solar and Natural Resources for a Better Efficiency in the Built Environment, *Solar Energy – The State of the Art – ISES Position Papers*, Ch. 1, James & James Ltd. pp.1-22.

Schlichting, H., 1979, Boundary Layer Theory, 7th Ed., *McGraw-Hill*, New York.

Tao, L.N., 1960, On Combined Free and Forced Convection in Channels, *J. Heat Transfer*, Vol. 82, pp. 233-238.

Tasnim, S. and Collins, M., (2004), Laminar Natural Convection Heat Transfer in Windows with Between-the-Panes Venetian Blinds, *Proc. Solar Energy Society of Canada Inc.*, August 21-25, Waterloo, Ontario, Canada.

Tripanagnostopoulos, Y., Bazilian, M., Zoulia, I. and Battisti, R., 2002, Hybrid PV/T System with Improved Air Heat Extraction Modification, *Proc. Int. Conference PV in Europe*, Oct 7-11, Rome.

Tripanagnostopoulos, Y., Nousia, T. and Souliotis, M., 2000, Low Cost Improvements to Building Integrated Air Cooled Hybrid PV-Thermal Systems, *Proc. 16th European PV Solar Energy Conference*, May 1-5, Glasgow, UK, pp. 1874-1877.

TRNSYS Reference Manual, 1996, Solar Energy Laboratory, *University of Wisconsin-Madison*.

U.S. Census Bureau, 2005, 1990 Census of Population and Housing, *1990 Population and Housing Unit Counts: United States*.

UW, 1996, VISION4, Glazing System Thermal Analysis: Users and Reference Manuals, University of Waterloo, Ontario.

White, F.M., 2003, Fluid Mechanics, Fifth Ed., *McGraw-Hill*, New York, pp.343-377.

Wigginton, M. and McCarthy, B. 2000, *Environmental Second Skin Systems*, June 1st, from http://www.battlemccarthy.demon.co.uk/research/doubleskin/mainpage.htm.

WINDOW 4.1, 1994, A PC program for analyzing window thermal performance in accordance with standard NFRC procedures. Lawrence Berkeley Laboratory (LBL), Berkeley, USA.

Wright, J.L., 1998, Calculating Center-Glass Performance Indices of Windows, *ASHRAE Trans,* Vol. 1004, 1B, SF-98-12-4, pp. 1230-1241.

Wright, J.L. and Kotey, N.A., 2006, Solar Absorption by Each Element in a Glazing/Shading Layer Array, *ASHRAE Transactions*, Vol. 112, Part 2.

Xaman, J., Alvarez, G., Lira, L. and Estrada, C., 2005, Numerical Study of Heat Transfer by Laminar and Turbulent Natural Convection in Tall Cavities of Façade Elements, *Energy and Buildings*, Vol. 37, July, pp. 787-794.

Yang, H.X., Marshall, R.H. and Brinkworth, B.J., 1996, Validated Simulation for Thermal Regulation of Photovoltaic Wall Structures, *Proc. 25th IEEE Photovoltaic Specialists Conference*, May 13-17, Washington, DC.

Ye, P., Harrison, S.J. and Oosthuizen, P.H., 1999, Convective Heat Transfer from a Window with a Venetian Blind: Detailed Modelling, *ASHRAE Trans.*, Vol. 105, SE-99-15-03, pp. 1031-1037.

Appendix A

Overview of Numerical Modelling

A.1 Discretization Schemes

Within FLUENT, a control-volume analysis is employed to transform the governing equations (Eq. 3.1 - 3.4) into algebraic equations. As an example of the discretization process, consider the integral form of the steady-state transportation of a scalar variable ϕ within an arbitrary control volume V:

$$\oint \rho\phi\vec{\upsilon} \cdot d\vec{A} = \oint \Gamma_\phi \nabla\phi \cdot d\vec{A} + \int_V S_\phi dV \qquad \textbf{(A.1)}$$

where

ρ = density,
$\vec{\upsilon}$ = velocity vector,
$\vec{A}$ = surface area vector,
Γ_ϕ = diffusion coefficient for ϕ,
$\nabla\phi$ = gradient of ϕ,
S_ϕ = source of ϕ per unit volume.

The discretization of Eq. A.1 for a given CV can be represented as:

$$\sum_f^{N_{faces}} \rho_f \overrightarrow{v_f} \phi_f \cdot \overrightarrow{A_f} = \sum_f^{N_{faces}} \Gamma_\phi (\nabla\phi)_n \cdot \overrightarrow{A_f} + S_\phi V \qquad \textbf{(A.2)}$$

where the unknowns are:

N_{faces} number of faces enclosing the given CV,

ϕ_f value of ϕ convected through face ***f,***

$\rho_f \overrightarrow{v_f} \cdot \overrightarrow{A_f}$ mass flux through face,

$\overrightarrow{A_f}$ area of face ***f,***

$(\nabla\phi)_n$ magnitude of $\nabla\phi$ normal to face ***f.***

Note that all of the calculated ϕ values are stored at the center of the CV. All of the diffusion terms in Eq. A.2 are calculated using a central differencing scheme having second order accuracy. The convected portion of ϕ, namely ϕ_f, was calculated using an upwind scheme, which can be either first or second order. Throughout this thesis, second order upwind schemes were employed for calculating the momentum, turbulence and energy terms. The second order upwind scheme, which provides second order accuracy, calculates ϕ_f using the following equation:

$$\phi_f = \phi + \nabla\phi \cdot \Delta\vec{s} \qquad \textbf{(A.3)}$$

where ϕ_f, ϕ, $\nabla\phi$ and $\Delta\vec{s}$ are the face value, cell-centered value, gradient from the upstream cell and displacement vector from the centroid of the upstream cell to the face centroid, respectively. The Taylor series expansion about the cell centroid requires the application of the divergence theorem to solve the $\nabla\phi$ terms for each cell as follows:

$$\nabla\phi = \frac{1}{V}\sum_{f}^{N_{faces}} \tilde{\phi}_f \vec{A} \qquad \textbf{(A.4)}$$

where $\tilde{\phi}_f$ is the average value of ϕ_f for the two adjacent cells.

A.2 Linearization

In order to calculate the unknown quantities (such as ϕ in Eq. A.2), a set of coupled non-linear equations must be solved. In order to solve the coupled equations, they must first be linearized. The linearization of Eq. A.2 would be as follows:

$$a_P \phi = \sum_{nb} a_{nb} \phi_{nb} + b \tag{A.5}$$

where a_P and a_{nb} are the linearized coefficients for ϕ and ϕ_{nb}, respectively where the subscript "nb" refers to the neighboring cells and b is a constant which includes any source term. This set of linearized algebraic equations makes up a sparse coefficient matrix which is then solved using a Gauss-Seidel solver combined with an algebraic multigrid method (FLUENT, 2005) for all scalar equations.

A.3 Under-Relaxation Factors

The discretization schemes rely on under-relaxation factors to ensure smooth convergence of all non-linear equations. Smooth convergence is achieved by controlling the total change of variable ϕ from one iteration to the next using the following equation:

$$\phi = \phi_{old} + \alpha \Delta \phi \tag{A.6}$$

The new value ϕ is therefore obtained from the previous value of ϕ, namely ϕ_{old}, plus a percentage (α) of the calculated change ($\Delta\phi$) between the old and new value. The multiplying factor α is the under-relaxation factor and can be controlled in FLUENT. For the majority of the validation, the default values were used for all under-relaxation factors (Table A.1).

Table A.1: Summary of under-relaxation factors.

Under-Relaxation Factors	
Pressure	0.3
Density	1
Body Forces	1
Momentum	0.7
Turbulent Kinetic Energy	0.8
Specific Dissipation Rate	0.8
Turbulent Viscosity	1
Energy	1
Discrete Ordinates	1

A.4 Numerical Method

In FLUENT, two methods are available for solving the discretized equations: segregated and coupled solver. The methods differ in the way that the unknown quantities are solved. A segregated implicit solver scheme was employed throughout the modelling; variables are solved sequentially (Figure A.1) for each control volume using existing values as well as the unknown neighboring values. As the equations are non-linear, several iterations are required in order to achieve convergence.

The discretization equations for the segregated solver are as follows:

$$\text{Continuity: } \sum_{f}^{N_{faces}} J_f A_f = 0 \qquad \textbf{(A.7)}$$

where J_f is the mass flux through any face f.

$$\text{x-Momentum: } a_P u = \sum_{nb} a_{nb} u_{nb} + \sum p_f A \cdot \hat{i} + S \qquad \textbf{(A.8)}$$

Due to the pressure-velocity coupling in Eq. A.8, Eq. A.7 is used to calculate a pressure value from the velocity terms. The pressure-velocity relationship is:

$$J_f = \hat{J}_f + d_f \left(p_{c0} - p_{c1} \right) \qquad \textbf{(A.9)}$$

where p_{c0} and p_{c1} are the pressures of the cells adjacent the face *f* and *df* is determined as a function of a_P (FLUENT, 2005). Within FLUENT, various schemes are available to the user for solving Eq. A.9. The default scheme, called the SIMPLE pressure-velocity coupling scheme, relates the pressure at a CV face to the velocity at the same face by ensuring mass flux is conserved across a cell. The SIMPLE scheme was employed throughout this thesis.

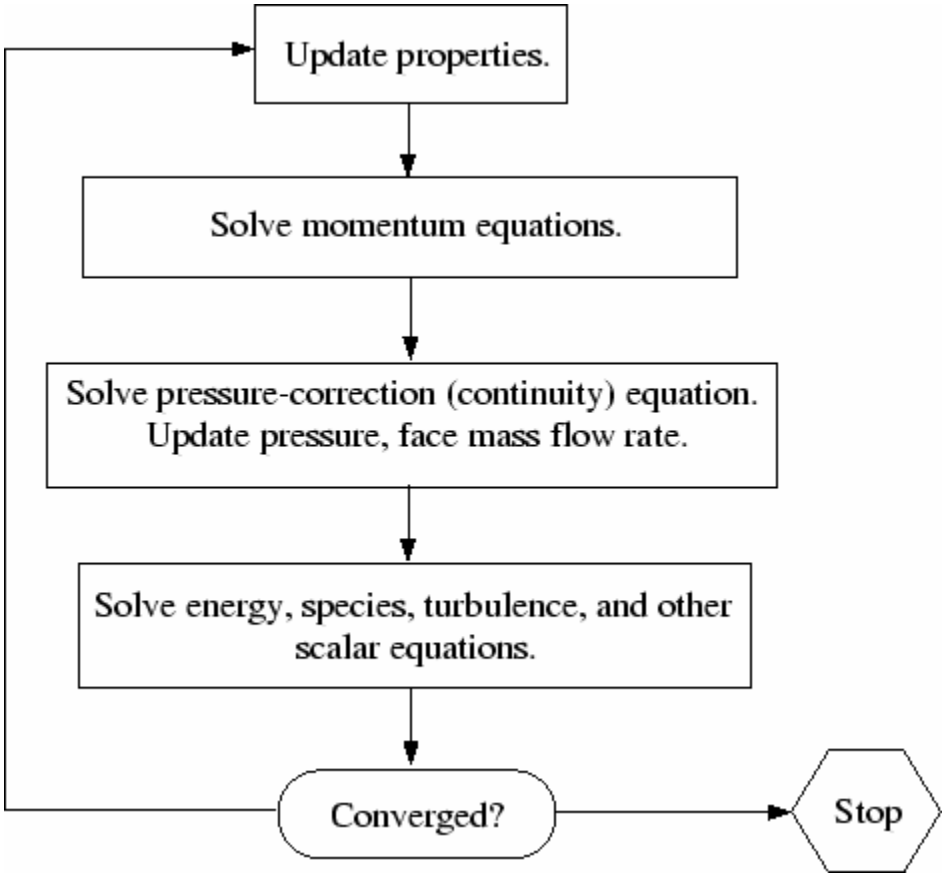

Figure A.1: Solution method for segregated solver method.

A.5 Residuals

Ideally, numerical convergence is attained when conservation is obtained for all of the unknown values within each CV of the entire flow domain. However, due to time and processing constraints, basic assumptions and approximations are inherent to the

software, absolute convergence impossible. For this reason, residuals are employed to provide the user with a quantifiable measure of the convergence levels for each run.

After each iteration, the values of the conserved quantities are calculated according to Figure A.1. From these values, FLUENT computes a residual as follows:

$$R^{\phi} = \sum_{cellsP} \left| \sum_{nb} a_{nb}\phi_{nb} + b - a_P\phi_P \right| \quad \textbf{(A.10)}$$

As it is difficult to judge convergence based on absolute residual values, FLUENT employs a scaling factor to calculate a *scaled* residual:

$$R^{\phi} = \frac{\sum_{cellsP} \left| \sum_{nb} a_{nb}\phi_{nb} + b - a_P\phi_P \right|}{\sum_{cellsP} \left| a_P\phi_P \right|} \quad \textbf{(A.11)}$$

With an appropriate solver and model, residuals will approach zero without ever attaining it. As such, the ability to determine whether or not a solution has converged is difficult and the convergence results are often times misleading.

A.6 Convergence Criteria

Although the FLUENT help files acknowledge that there are no universal metrics for judging convergence (FLUENT, 2005), certain guidelines are put forth that can, in some circumstances, be used for measuring the success level of a given numerical convergence. It should be noted that all quoted residual values refer to the *scaled* values. The default convergence values in FLUENT are 10^{-3} for all equations with the exception of the energy equation, which is set at 10^{-6}. Although this criteria is appropriate for most problems, it can be misleading in some cases. FLUENT cautions that the success of the

convergence is based upon the initial guess, which is required to start the iteration process, as well as the nature of the flow. A poor initial value may result in over-inflated scaling, leading to a low-scaled residual. As such, a small residual may not always guarantee that a successful convergence has been obtained. Conversely, an accurate initial guess may lead to a large scaled-residual due to the small overall change of the value in question. For instance, in flows where given variables are nearly zero everywhere, like the cross-stream velocity in pipe flow, an initial guess of zero for the velocity will result in a small drop in the residual, which is again misleading. The best verification of a successful convergence is to measure the results against known values after the scaled residuals have stabilized. For the numerical modelling performed during this thesis project, residual targets were set to 10^{-8}. Although not all residuals dropped below 10^{-8}, a run was terminated once the scaled residuals steadied at or below 10^{-4}. In the rare case where a scaled residual did not surpass 10^{-4}, the behavior could be linked to one of the explanations mentioned above. As an additional convergence check, conservation of all relevant values was measured as the total difference between the influx and outflux. Typically, the conservation discrepancies were less than 0.5% of the known influx.

Appendix B

Sample Data for Data Set A

x-pos [mm]	y-pos [mm]	U pix [pix]	V pix [pix]	U [m/s]	V [m/s]	Std dev (U) [m/s]	Std dev (V) [m/s]
Time stamp:	5/3/2005	10:49:19:200AM					
3.61452	2.40968	0	0	0	0	0	0
4.81935	2.40968	0	0	0	0	0	0
6.02419	2.40968	0	0	0	0	0	0
7.22903	2.40968	0	0	0	0	0	0
8.43387	2.40968	0	0	0	0	0	0
9.63871	2.40968	0	0	0	0	0	0
10.8435	2.40968	0	0	0	0	0	0
12.0484	2.40968	0	0	0	0	0	0
13.2532	2.40968	0	0	0	0	0	0
14.4581	2.40968	0	0	0	0	0	0
15.6629	2.40968	0.052625	0.014254	0.007926	0.002147	0.00463982	0.00193446
16.8677	2.40968	0.10525	0.028509	0.015851	0.004294	0.00927964	0.00386892
18.0726	2.40968	0.157876	0.042763	0.023777	0.00644	0.0139195	0.00580338
19.2774	2.40968	0.210501	0.057017	0.031702	0.008587	0.0185593	0.00773785
20.4823	2.40968	0.126288	4.72381	0.01902	0.711428	0.0334439	0.266615
21.6871	2.40968	0.035388	7.63164	-0.00533	1.14936	0.0600917	0.217224
22.8919	2.40968	-0.0013	7.95587	-0.0002	1.19819	0.062118	0.18684
24.0968	2.40968	0.002014	8.32166	-0.0003	1.25328	0.0639384	0.385352
25.3016	2.40968	0.072397	8.42659	0.010903	1.26909	0.0641329	0.383329
26.5064	2.40968	0.089796	8.53644	0.013524	1.28563	0.0691654	0.381572
27.7113	2.40968	0.087337	8.61857	0.013153	1.298	0.0723326	0.371323
28.9161	2.40968	0.07699	8.66497	0.011595	1.30499	0.0740289	0.363269
30.121	2.40968	0.062354	8.71877	0.009391	1.31309	0.0726054	0.365238
31.3258	2.40968	0.035632	8.7343	0.005366	1.31543	0.0733441	0.367497
32.5306	2.40968	0.000269	8.7793	4.05E-05	1.3222	0.0730173	0.372308
33.7355	2.40968	0.032186	8.82923	-0.00485	1.32972	0.0736211	0.375755
34.9403	2.40968	-0.07112	8.87932	-0.01071	1.33727	0.0758876	0.376026
36.1452	2.40968	0.116717	8.92004	-0.01758	1.3434	0.0786399	0.37751
37.35	2.40968	-0.15975	8.93199	-0.02406	1.3452	0.0774531	0.374784

38.5548	2.40968	-0.16856	8.93003	-0.02539	1.3449	0.0760888	0.373001
39.7597	2.40968	0.155819	8.92372	-0.02347	1.34396	0.0732561	0.36241
40.9645	2.40968	0.128187	8.90837	-0.01931	1.34164	0.0661183	0.352403
42.1693	2.40968	0.081373	8.65754	-0.01226	1.30387	0.0492233	0.163941
43.3742	2.40968	0.066658	8.7986	-0.01004	1.32511	0.0480222	0.344488
44.579	2.40968	0.018359	8.21716	-0.00276	1.23754	0.0376744	0.226832
45.7839	2.40968	0.028495	4.31708	-0.00429	0.650173	0.0141134	0.0986429
46.9887	2.40968	0.014248	2.15854	-0.00215	0.325086	0.00705668	0.0493214
48.1935	2.40968	0	0	0	0	0	0
49.3984	2.40968	0	0	0	0	0	0
50.6032	2.40968	0	0	0	0	0	0
51.8081	2.40968	0	0	0	0	0	0
53.0129	2.40968	0	0	0	0	0	0
54.2177	2.40968	0	0	0	0	0	0
55.4226	2.40968	0	0	0	0	0	0
56.6274	2.40968	0.061731	3.457	-0.0093	0.52064	0.254005	0.49174
57.8322	2.40968	0.224462	4.01262	-0.03381	0.60432	0.493648	0.707617

Appendix C

Chapter 3 Calculations

Data collected on March 13th 2006 was used to compare the numerical results to experimental data. In Chapter 3, it was mentioned that the measured solar irradiance was primarily diffuse in nature, with only 0.5% of the radiation acting as beam. A general overview of the relevant theory on radiation is provided in this appendix. The presented theory will be used to explain the statement that only 0.5% of the radiation was beam.

Effect of Atmosphere

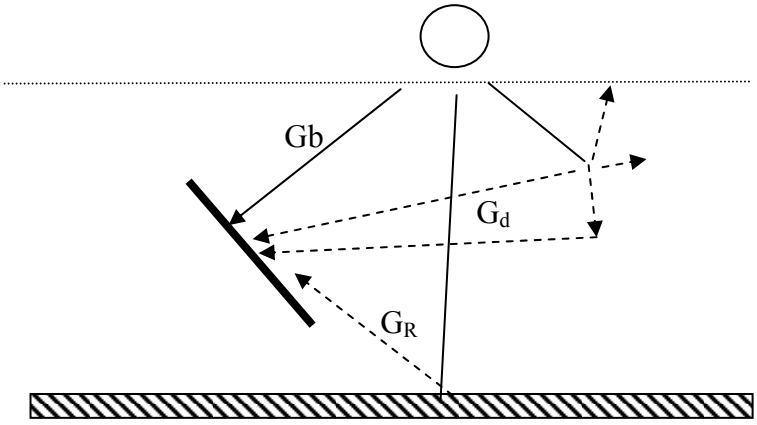

- When solar rays enter the atmosphere, some photons are scattered and/or absorbed.
- Unscattered photons constitute beam irradiance, G_b, and have the same directional characteristics of G_o.
- Some scattered photons arrive at a surface and constitute diffuse irradiance, G_d.
- Some photons are reflected by the ground, G_g.

- The total irradiance is $G_t = G_b + G_d + G_g$.

$$H_i, I_i = \int_{t1}^{t2} G_i dt \qquad \text{where i = b, d, g, t}$$

Solar Measurement

Pyranometer (Total and Diffuse): A black disc attached to a metal heat sink. The temperature between the centre and the edge indicate the strength of solar radiation. A glass dome prevents convection from influencing the readings.
- Some use a black and white disc.
- Some use shades and fans to keep the heat sink at a constant temperature.
- A shade band or disc is often used to remove direct irradiation (diffuse measure only)

The pyranometer used at Concordia University was a LI-200SA model. A full description of the sensor can be found in Appendix D.

The Clearness Index
- This measure of atmospheric clarity "KAYTEE" is defined for different time periods.

$$k_t' = \frac{G_{t,H}}{G_{o,H}} \qquad \text{instantaneous}$$

$$k_t = \frac{I_{t,H}}{I_{o,H}} \qquad \text{hourly}$$

$$K_T = \frac{H_{t,H}}{H_{o,H}} \qquad \text{daily}$$

$$\overline{K}_T = \frac{\overline{H}_{t,H}}{\overline{H}_{o,H}} \qquad \text{monthly-averaged daily}$$

- The diffuse Fraction "KAY" also indicates clarity

$$k' = \frac{G_{d,H}}{G_{t,H}} \qquad \text{instantaneous}$$

$$k = \frac{I_{d,H}}{I_{t,H}} \qquad \text{hourly}$$

$$K = \frac{H_{d,H}}{H_{t,H}} \qquad \text{daily}$$

$$\overline{K} = \frac{\overline{H}_{d,H}}{\overline{H}_{t,H}} \qquad \text{monthly-averaged daily}$$

The data that was collected at Concordia University and used to validate the numerical work was instantaneous data but was used to represent an average over the hour (between 1 and 2 pm). Only the hourly, daily or monthly-averaged daily clearness indexes were not required.

Relationship Between KAY and KAYTEE (Beam / Diffuse Relations)

- There are more correlations than are presented here.

(1) $\overline{K}$ verses $\overline{K}_T$ (monthly-averaged daily) (Erbs et al.)

$$\overline{K} = 1.391 - 3.560\overline{K}_T + 4.189\overline{K}_T^2 - 2.137\overline{K}_T^3 \qquad \text{for } \omega_s \le 81.4^o \text{ and } 0.3 \le \overline{K}_T \le 0.8$$

$$\overline{K} = 1.311 - 3.022\overline{K}_T + 3.427\overline{K}_T^2 - 1.821\overline{K}_T^3 \qquad \text{for } \omega_s > 81.4^o \text{ and } 0.3 \le \overline{K}_T \le 0.8$$

(2) K verses K_T (daily) (Erbs et al.)

For $\omega_s \le 81.4^o$

$$K = \begin{cases} 1.0 - 0.27279K_T + 2.4495K_T^2 - 11.9514K_T^3 + 9.3879K_T^4 & \text{for } K_T < 0.715 \\ 0.143 & \text{for } K_T \ge 0.715 \end{cases}$$

For $\omega_s > 81.4^o$

$$K = \begin{cases} 1.0 + 0.2832K_T - 2.5557K_T^2 + 0.8448K_T^3 & \text{for } K_T < 0.722 \\ 0.175 & \text{for } K_T \ge 0.722 \end{cases}$$

(3) k verses k_t (hourly) (Erbs et al.)

- Important to hourly monitoring, and analysis of concentrating collectors.

$$k = \begin{cases} 1.0 - 0.249\,k_t & \text{for } k_t \le 0.35 \\ 1.557 - 1.84k_t & \text{for } 0.35 < k_t \le 0.75 \\ 0.177 & \text{for } k_t > 0.75 \end{cases}$$

The third (3) correlation was used for the analysis in Chapter 3 for the case where $k_t \le 0.35$.

<u>Directional Distribution of Diffuse Radiation</u>

- It is possible to estimate G_{dT} from G_{dH}.

- On an overcast day, the scattered radiation appears to come uniformly from all directions. (Isotropic Model)

- On a clear day, the intensity is highest near the sun, and also high near the horizon.

- The isotropic model for clear and overcast skies was used throughout the analysis. The error associated with the isotropic model is not excessive, provided that the surface is oriented skywards (10 to 20% error in diffuse component).

$$G_{dT} = G_{dH}\left(\frac{1+\cos\beta}{2}\right)$$

Instantaneous (G_T) and Hourly Radiation (I_T) On Tilted Surfaces

- Often, solar radiation on a horizontal surface is known, but we require radiation on a tilted surface.

Beam Radiation

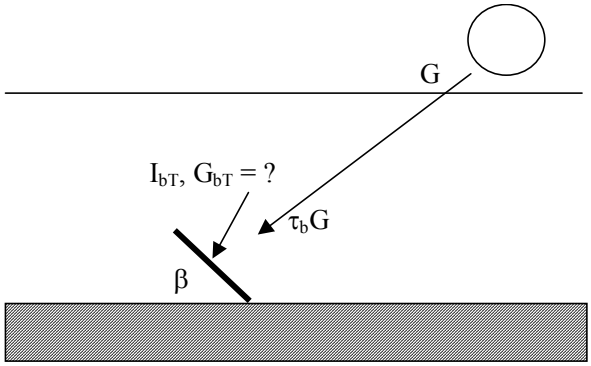

- It is useful to define the beam transmittance of the atmosphere as

$$\tau_b = \frac{G_{bH}}{G_{oH}} = \frac{G_{tH} - G_{dH}}{G_{tH}} \cdot \frac{G_{tH}}{G_{oH}} = \left(1 - \frac{G_{dH}}{G_{tH}}\right) \cdot \frac{G_{tH}}{G_{oH}} = (1-k')k_t'$$

$$\therefore G_{bT} = \tau_b G_{oT} = (1-k')k_t' G_{oT}$$

- Integrating over one hour gives

$$I_{bT} = (1-k)k_t I_{oT}$$

- Remember, $k = k(k_t)$, so this gives I_{bT} from knowledge of k_t.

Diffuse Radiation (Isotropic Model)
- Diffuse radiation is easy to describe due to its uniformity

$$G_{dT} = G_{dH}\left(\frac{1+\cos\beta}{2}\right) = \frac{G_{dH}}{G_{tH}} \cdot \frac{G_{tH}}{G_{oH}}\left(\frac{1+\cos\beta}{2}\right)G_{oH} = k'k_t'\left(\frac{1+\cos\beta}{2}\right)G_{oH}$$

$$\therefore G_{dT} = k'k_t'\left(\frac{1+\cos\beta}{2}\right)G_{oH}$$

- Integrating over one hour gives

$$I_{dT} = kk_t\left(\frac{1+\cos\beta}{2}\right)I_{oH}$$

Ground Reflected Radiation

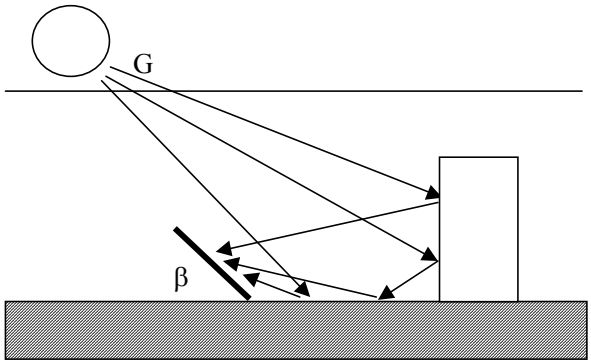

- Solar radiation reflects from objects and the ground and then may reach a surface. Only radiation from the ground was considered and it was treated as a diffuse reflector. The ground was assigned a solar reflectance, ρ_g, extending to the horizon, of 0.2.

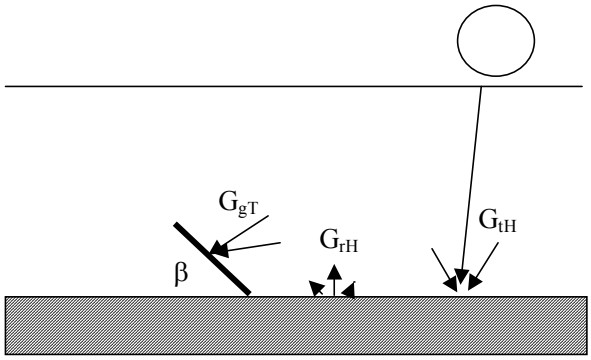

G_{rH} = ground reflected flux

$$G_{rH} = \rho_g G_{tH} = \rho_g k_t' G_{oH}$$

G_{gT} = ground reflected flux at surface

$$G_{gT} = G_{rH}\frac{A_g F_{g\_s}}{A_s} = G_{rH}F_{s\_g} = G_{rH}\left(\frac{1-\cos\beta}{2}\right)$$

$$G_{gT} = \rho_g G_{tH}\left(\frac{1-\cos\beta}{2}\right) = \rho_g k_t' G_{oH}\left(\frac{1-\cos\beta}{2}\right)$$

- Integrating over one hour

$$I_{gT} = \rho_g k_t I_{oH}\left(\frac{1-\cos\beta}{2}\right)$$

Total Radiation

- The total instantaneous irradiation is given by

$$G_{tT} = G_{bT} + G_{dT} + G_{gT}$$

$$G_{tT} = (1-k')k_t' G_{oT} + k'k_t'\left(\frac{1+\cos\beta}{2}\right)G_{oH} + \rho_g k_t' G_{oH}\left(\frac{1-\cos\beta}{2}\right)$$

The measured value on March 13th was G_{tT} = 40 W/m2. Since the AFW is perpendicular to the ground, $\beta = \pi/2$. Using the above equations, the beam radiation incident upon the surface was calculated to be G_{bT} = 0.2 W/m2 or only 0.5% of the total radiation.

- The total hourly irradiation is given by

$$I_{tT} = I_{bT} + I_{dT} + I_{gT}$$

$$I_{tT} = (1-k)k_t I_{oT} + kk_t\left(\frac{1+\cos\beta}{2}\right)I_{oH} + \rho_g k_t I_{oH}\left(\frac{1-\cos\beta}{2}\right) \text{ and } k = k(k_t)$$

- Once we can estimate k_t, we can get I_{tT}. I_{oH} and I_{oT} can be estimated using

$$I_{oT} = \int_{t-\Delta t/2}^{t+\Delta t/2} G(t)dt \cong G(t)\Delta t$$

the error in this is about 0.3% unless sunrise or sunset falls within the hour.

- To use this equation, weather files usually supply I_{tH} and I_{dH}. Then
  1) obtain $k_t = I_{tH}/I_{oH}$
  2) obtain $k = I_{dH}/I_{tH}$, or use diffuse correlation
  3) use above equation

Use of R-Ratios to Get Hourly Radiation on Tilted Surfaces

- R-ratios are defined to convert radiation on the horizontal to radiation on the tilted surface.

- For beam radiation

$$I_{bT} = (1-k)k_t I_{oT} = (1-k)k_t e_n G_{SC}(\cos\theta)^+ \Delta t$$

$$I_{bH} = (1-k)k_t e_n G_{SC} (\cos\theta_z)^+ \Delta t$$

- So

$$R_b = \frac{I_{bT}}{I_{bH}} = \frac{[\cos\theta]^+}{[\cos\theta_z]^+} \qquad \text{where} \qquad [x]^+ = \frac{|x| + x}{2}$$

- Assuming $\omega_r' < \omega < \omega_s'$

$$R_b = \frac{I_{bT}}{I_{bH}} = \frac{\cos\theta}{\cos\theta_z}$$ (R_b is also given in the text as Eqns 1.8.2 and 1.8.3)

- Similarly, we get

$$R_d = \frac{I_{dT}}{I_{dH}} = \frac{1+\cos\beta}{2}$$

$$R_g = \frac{I_{gT}}{I_{gH}} = \left(\frac{1-\cos\beta}{2}\right)\rho_g$$

- The total hourly irradiation is given by

$$I_{tT} = R_b I_{bH} + R_d I_{dH} + R_g I_{gH} = R_b\left(\frac{I_{tH} - I_{dH}}{I_{tH}}\right) I_{tH} + R_d \frac{I_{dH}}{I_{tH}} I_{tH} + R_g I_{gH}$$

$$\boxed{I_{tT} = I_{tH}\left(R_b(1-k) + R_d k + R_g\right)}$$

- As before, get $k_t = I_{tH}/I_{oH}$ from data, and $k = k(k_t)$ or $k = I_{dH}/I_{tH}$

Appendix D

Pyranometer Sensor Information

LI-200SA Pyranometer Sensor

LI-COR, Inc. Toll Free: 1-800-447-3576 (U.S. & Canada) • Phone: 402-467-3576 • FAX: 402-467-2819 • E-mail: envsales@env.licor.com • Internet: http://www.licor.com

Total Solar Radiation

The LI-200SA Pyranometer is designed for field measurement of global solar radiation in agricultural, meteorological, and solar energy studies. In clear unobstructed daylight conditions, the LI-COR pyranometer compares favorably with first class thermopile type pyranometers (1, 2), but is priced at a fraction of the cost.

Patterned after the work of Kerr, Thurtell and Tanner (3), the LI-200SA features a silicon photovoltaic detector mounted in a fully cosine-corrected miniature head. Current output, which is directly proportional to solar radiation, is calibrated against an Eppley Precision Spectral Pyranometer (PSP) under natural daylight conditions in units of watts per square meter (w m^{-2}). Under most conditions of natural daylight, the error is <5%.

The spectral response of the LI-200SA does not include the entire solar spectrum (Figure 1), so it must be used in the same lighting conditions as those under which it was calibrated. Therefore, the LI-200SA should only be used to measure unobstructed daylight. It should NOT be used under vegetation, artificial lights, in a greenhouse, or for reflected solar radiation.

LI-200SA Specifications

Calibration: Calibrated against an Eppley Precision Spectral Pyranometer (PSP) under natural daylight conditions. Typical error under these conditions is ± 5%.

Sensitivity: Typically 90 µA per 1000 W m^{-2}.

Linearity: Maximum deviation of 1% up to 3000 W m^{-2}.

Stability: < ± 2% change over a 1 year period.

Response Time: 10 µs.

Temperature Dependence: 0.15% per °C maximum.

Cosine Correction: Cosine corrected up to 80° angle of incidence.

Azimuth: < ± 1% error over 360° at 45° elevation.

Tilt: No error induced from orientation.

Operating Temperature: -40 to 65°C.

Relative Humidity: 0 to 100%.

Detector: High stability silicon photovoltaic detector (blue enhanced).

Sensor Housing: Weatherproof anodized aluminum case with acrylic diffuser and stainless steel hardware.

Size: 2.38 Dia. × 2.54 cm H (0.94" × 1.0").

Weight: 28 g (1 oz).

Cable Length: 3.0 m (10 ft).

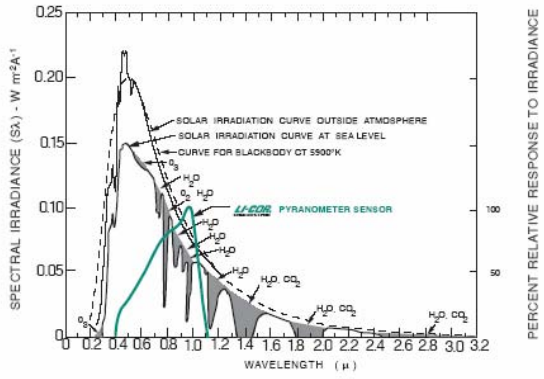

Figure 1. The LI-200SA Pyranometer spectral response is illustrated along with the energy distribution in the solar spectrum (3).

Ordering Information

The LI-200SA Pyranometer Sensor cable terminates with a BNC connector that connects directly to the LI-250 Light Meter or LI-1400 DataLogger. The 2220 Millivolt Adapter should be ordered if the LI-200SA will be used with a strip chart recorder or datalogger that measures millivolts. The 2220 uses a 147 ohm precision resistor to convert the LI-200SA output from microamps to millivolts. The sensor can also be ordered with bare leads (without the connector) designated LI-200SZ. Both are available with 50 foot cables, LI-200SA-50 or LI-200SZ-50. The 2003S Mounting and Leveling Fixture is recommended for each sensor unless other provisions for mounting are made. Other accessories are described on the Accessory Sheet.

LI-200SA Pyranometer
LI-200SZ Pyranometer
LI-200SA-50 Pyranometer
LI-200SZ-50 Pyranometer
2220 Millivolt Adapter
2003S Mounting and Leveling Fixture
2222SB-50 Extension Cable
2222SB-100 Extension Cable

REFERENCES

1. Flowers, E.C. 1978. Comparison of solar radiation sensors from various manufacturers. In: 1978 annual report from NOAA to the DOE.

2. Palmiter, L.S., L.B. Hamilton, M.J. Holtz. 1979. Low cost performance evaluation of passive solar buildings. SERI/RR-63-223. UC-59B.

3. Kerr, J.P., G.W. Thurtell and C.B. Tanner. 1967. An integrating pyranometer for climatological observer stations and mesoscale networks. J. Appl. Meterol. 6:688-694.